Research on the Basic Understanding of High Efficiency in Silicon Solar Cells

Annual Report
1 December 1982 – 30 November 1983

A Subcontract Report

A. Rohatgi
P. Rai-Choudhury
Westinghouse R&D Center
Pittsburgh, Pennsylvania

September 1984

Solar Energy Research Institute
A Division of Midwest Research Institute

1617 Cole Boulevard
Golden, Colorado 80401

NOTICE

CONTENTS

LIST OF FIGURES

LIST OF TABLES

1. SUMMARY

The overall objective of this program is to develop a basic understanding of high efficiency silicon solar cells and achieve cell efficiencies greater than 17% by employing innovative concepts of material preparation, cell design, and fabrication technology. The program consists of a theoretical effort to develop models for very high-efficiency cell designs, experimental verification of the designs, and an improved understanding of efficiency-limiting mechanisms such as heavy doping effects and bulk and surface recombination.

In this program we have used 4 ohm-cm, high lifetime, (111) float-zone silicon obtained from Monsanto as our baseline material, in addition to low-resistivity gallium-doped Czochralski silicon and some boron-doped float-zone silicon in the resistivity range of 0.1-0.8 Ω-cm.

DLTS and generation lifetime measurements were performed on the 4 Ω-cm baseline float-zone material to confirm its high quality, and no deep levels were detected in this material. The minority-carrier generation lifetime, determined by pulse MOS technique, was about 350 μsecs.

Baseline n^+-p-p^+ solar cells were fabricated by 850°C/50 min $POCl_3$ diffusion and 950°C/20 min BBr_3 diffusion to form the emitter and the back-surface field, respectively. Cells were tested under 100 mW AM1 illumination, and an average efficiency of ~ 14.5% was obtained for 4 Ω-cm base cells with the maximum exceeding 15%. Short-circuit current density and open-circuit voltage were 33 mA/cm^2 and 580 mV, respectively.

We have used a theoretical model which involves an internal recombination velocity to assess the minority-carrier loss mechanisms in various regions of the solar cell. Using the guidelines of our model, we passivated the cell surfaces by thermal oxidation of silicon at

1

$800^{\circ}C$. We have successfully fabricated the oxide-passivated cells on 4 Ω-cm base material with efficiencies in the range of 17 to 17.5%, open-circuit voltage $\geqslant$ 600 mV, and short circuit current $\sim$ 36 mA/cm^2. As predicted by our model, oxide passivation provided an increase of about 20 mV in open-circuit voltage, $\sim$ 3 mA/cm^2 increase in J_{sc}, and about 2% improvement in absolute cell efficiency compared to the counterpart 15% efficient unpassivated cells. These cells have been tested and verified at SERI.

Detailed dark I-V and spectral response measurements were performed on the cells, with and without passivation, to understand the oxide-passivation-induced improvement. Transformed dark I-V data, in which bulk and junction recombination components were properly separated, showed a decrease in reverse saturation current (J_o) from 3.7 x 10^{-12} A/cm^2 to 2.0 x 10^{-12} A/cm^2 as a result of surface passivation. This decrease in J_o, coupled with an increase of 2-3 mA/cm^2 in J_{sc}, accounts for the observed 20 mV increase in V_{oc}. Spectral response and reflectivity measurements showed that a 17.2% efficient cell on 4 Ω-cm material has significantly higher quantum efficiencies in the wavelength range of 0.4-0.7 μm and somewhat higher quantum efficiency in the range of 0.9-1.1 μm, compared to the counterpart unpassivated cell. This indicates that oxide passivation is quite effective on both surfaces and reduces the loss of carriers via surface recombination.

We found that removal of back oxide from the passivated cells reduces J_{sc} by $\sim$ 0.5 mA/cm^2 and V_{oc} by $\sim$ 5 mV. The majority of increase in V_{oc} comes from the front-surface passivation, while both front and back-surface passivation contribute to the increase in J_{sc}. Thus, both front- and back-surface passivation are important and effective in our devices. It appears that without any passivation, emitter surface recombination velocity controls the reverse saturation current ($J_o \sim J_{oe}$); therefore, front passivation alone increases V_{oc} and J_{sc}. After the front-surface passivation, J_{oe} is reduced and the J_o or V_{oc} tends to become base dependent, and therefore an additional $\sim$ 5 mV increase in V_{oc} is observed when the back surface is passivated.

2

We have fabricated both baseline n^+-p-p$^+$ and the oxide-passivated O-n^+-p-p$^+$-O cells on a gallium-doped 0.3 to 0.7 Ω-cm Czochralski crystal which was pulled from a synthetic quartz crucible to minimize residual impurity concentration. Efficiencies of the n^+-p-p$^+$ solar cell were ~ 14.75% and the oxide-passivated cell efficiencies were ~ 16% with the maximum exceeding 16.3%. V_{oc} was ~ 615 mV and J_{sc} was ~ 33 mA/cm^2 in the passivated cells.

High-efficiency solar cells on boron-doped, lower-resistivity, float-zone silicon have also been fabricated. Without the oxide passivation, solar cell efficiencies on 0.1-0.2 Ω-cm material were ~15.5%, and after passivation the efficiency went up to 16.7% with V_{oc} of ~620 mV and J_{sc} of ~33 mA/cm^2. On 0.75 Ω-cm float-zone silicon, the cell efficiency was also ~15.5% without the oxide passivation, and went up to 16.9% as a result of oxide passivation. The open-circuit voltage was ~624 mV and the short-circuit current density was 34 mA/cm^2. In both cases we saw ~1-2 mA/cm^2 improvement in J_{sc} and about 10-15 mV improvement in V_{oc} as a result of oxide passivation, which is somewhat less than what we found for 4 Ω-cm material. This particular run had a patchy antireflective coating due to a slight problem in the photoresist step. We therefore anticipate better results on these crystals.

In the case of 0.1-0.2 Ω-cm material, quantum efficiency improvement was observed only in the shorter wavelength range probably because these wafers were ~ 350 μm thick and cell width to diffusion length ratio was somewhat larger. This is consistent with the relatively smaller improvement observed in these cells due to the oxide passivation, compared to 4 Ω-cm cells.

Consistent with the model design, we fabricated a gallium back-surface field with a surface concentration of ~ 5 x 10^{18} cm^{-3}, a depth of ~ 2 μm by open-tube gallium (OTG) diffusion at 1230°C. In this first attempt, despite the desired surface concentration, we observed a degradation in the n^+-p-p$^+$ solar cell efficiencies from 15% to 13%. This loss in cell performance is attributed to a decrease in carrier

lifetime, suggesting that the gallium diffusion conditions need to be optimized.

Few attempts have been made to deposit silicon nitride coating by a plasma-enhanced technique using silane and ammonia gases. Initial results on baseline n^+-p-p^+ cells look quite promising, indicating ~45% enhancement in the short-circuit current and >50% improvement in cell efficiency. Open-circuit voltage is higher than for the cells with spin-on coating, suggesting that these films can also passivate the silicon surface. Multilayer AR coating with varying refractive index is being investigated.

Attempts were made to apply reflective back contacts by replacing Ti-Pd-Ag with Al, Ag, and Au. Ag and Au back contacts peeled off because of poor adhesion with the back oxide but the results with Al back contact were encouraging. More work needs to be done in this area.

One attempt was made to make a high-low emitter using epitaxial growth. Poor lifetime in the epi-layer resulted in low cell efficiency. Further attempts are being made to improve this lifetime.

2. INTRODUCTION

This report is a summary of activities conducted under Phase I of a SERI-sponsored program to develop high-efficiency solar cells.

2.1 Objective

The objective of this program is to develop a basic understanding of high-efficiency silicon solar cells and to achieve cell efficiencies greater than 17%. Important considerations for improving silicon solar cell efficiency include high-purity silicon, proper cell design, and careful cell processing. Specifically, the current phase of the program is concerned with: 1) theoretical study or models leading to high-efficiency cell designs, 2) material selection and experimental verification of the designs and analysis, and 3) identification and improved understanding of mechanisms which degrade or limit cell performance.

2.2 Technical Approach

2.2.1 Theory and Design

Recent efforts to increase the efficiency of silicon solar cells have been correctly focussed on the problem of raising the open-circuit voltage. Current collection efficiency has reached near the theoretical limits.[1-3] This emphasis has led directly to the problem of maximizing the effective diffusion length in all parts of the device while using substrate material with the highest possible donor or acceptor concentrations. These provisions act in opposition and are modified by the specific details of the device structure. It is thus evident that an optimization is possible. The problem is greatly complicated by imperfectly understood mechanisms or imprecise knowledge of the controlling parameters, and by experimental difficulties in separating the effects of these mechanisms.

The major problems of efficiency improvement fall in the above categories; however, there are additional design requirements for efficient contacts and antireflective coatings. Although these areas are better understood, they are not trivial and must be satisfied in a manner compatible with the requirements of the rest of the device.

The mechanisms to be dealt with can be more or less separated into heavy-doping effects and recombination processes, resistive losses, and optical losses. These three mechanisms are discussed in the following subsections.

2.2.2 Heavy Doping and Recombination

Basic diode theory provides a simple relationship to examine the doping requirements for a high-efficiency cell. We assume an idealized device consisting solely of a high lifetime base region with acceptor concentration, N_a, and width, W, bounded on the top side by a collecting junction and on the bottom side by a zero recombination back contact. In the steady state, under low-injection and open-circuit conditions, the electron concentration will be nearly constant throughout the base; the value of the electron concentration is governed by the generation (G) and recombination (R) rates, which must be equal:

$$G = R$$

The generation rate is given by:

$$G = N_{ph}/W$$

$$R = n_p/\tau_n$$

where N_{ph} is the photon flux, n_p is the electron concentration, and τ_n the lifetime. If this device is to produce an open-circuit voltage of V_{oc}, then the electron concentration at the edge of the space-charge region, n_p, is given by:

$$n_p = n_{po} \exp(V_{oc}/V_T) = (n_i^2/N_a) \exp(V_{oc}/V_T)$$

$V_T = kT/q$ and the other symbols have their usual meaning. Combining these gives the desired relationship:

$$N_a = \frac{W n_i^2}{\tau_n N_{ph}} \exp(V_{oc}/V_T)$$

We see that for a given open-circuit voltage, the base doping level must increase as the base lifetime becomes smaller or the base width is increased. If we assume a photon flux, $N_{ph} = 2.5 \times 10^{17}/cm^2$-sec, a flux equivalent to a maximum short-circuit current of 40 mA, then for a V_{oc} of 0.7 volts, width of 150 μm, and a base lifetime of 200 μs, the minimum base doping is ~ $7 \times 10^{16}/cm^3$. We cannot expect to do better than this idealized analysis implies. Our proposed approach attempts to follow its guidelines; that is, minimize the basewidth consistent with absorption, maximize lifetimes, and use the highest doping levels which do not lead to the heavy doping penalties of band-narrowing and Auger recombination.

To contend with these design questions we have developed several simple models which, although neither complete nor fully verified, provide good agreement with experiment in most cases. For the present problem, the "effective recombination velocity model" or Se model is particularly useful.[4] This model includes the effect of band narrowing, Fermi statistics, trap and Auger recombination, and the effects of recombination at the device surfaces. While there are uncertainties as to the proper constants for Auger recombination and band narrowing, model results are in good general agreement with experimental data. This model is described in more detail in Section 3.1. Figure 1 shows results of voltage calculations for a back-surface-field (BSF) device using three different BSF structures with two different base diffusion lengths (see Table 1). The significance of the velocity is that the saturation current can be expressed in terms of the value of Se at the space-charge region boundary:
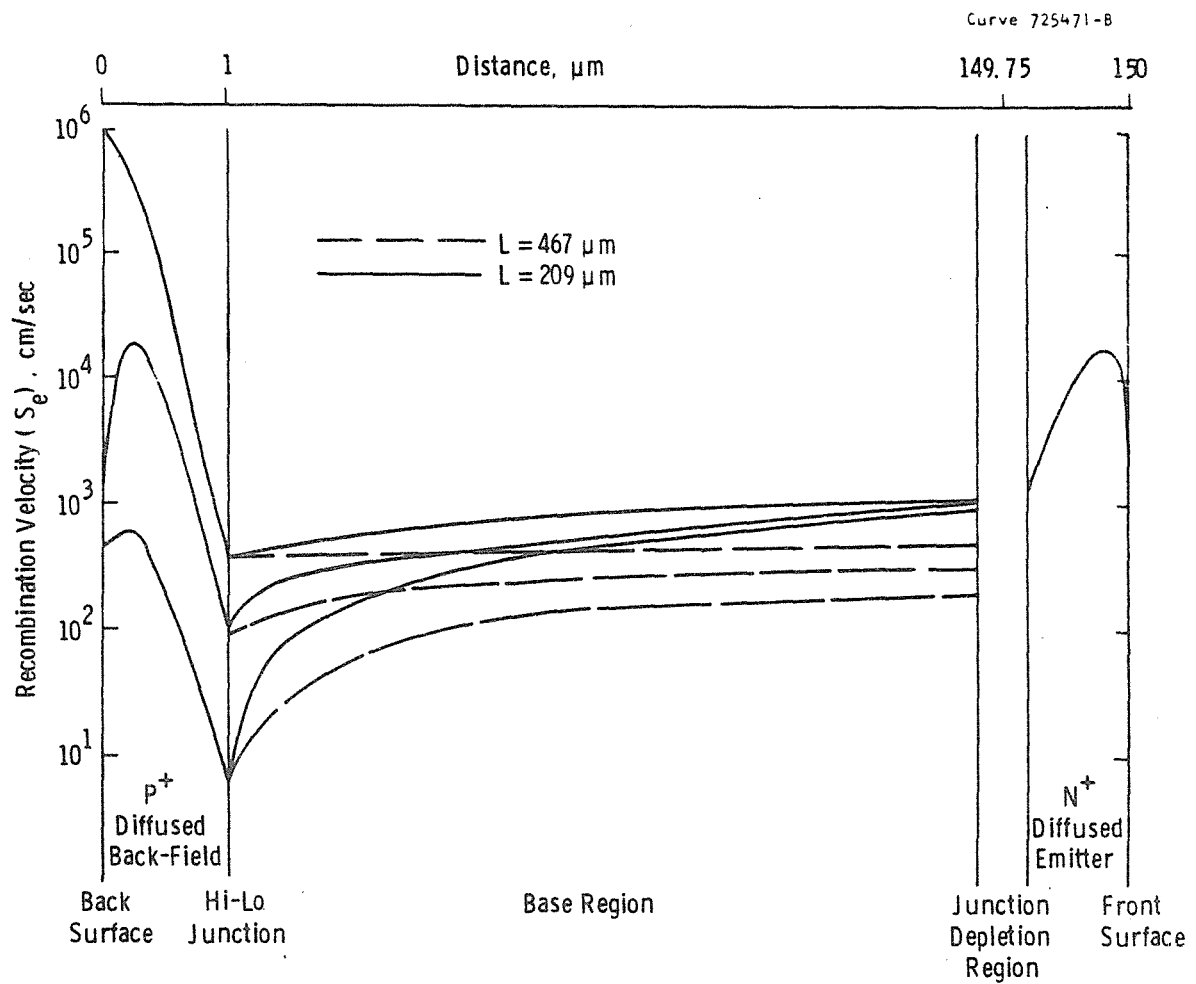
Figure 1.   Internal recombination velocity plots for
back-surface field solar cells.

Table 1. Calculated Performance for Narrow-Base Back-Field Solar Cells (4 ohm-cm, p-base, width 150 μm)

Intrinsic Base Diffusion Length, μm	Effective Base Diffusion Length, μm	V_{oc}, mV	J_{sc}, mA	n, %	Remarks
209	324	567	34	15.4	Ohmic back surface
209	330	571	34	15.5	Passive back surface
209	336	573	35	15.6	Passive back surface; reduced BSF doping
467	630	587	37	16.9	Ohmic back surface
467	1090	599	37	17.4	Passive back surface
467	1470	605	37	17.8	Passive back surface; reduced BSF doping

$$J_{on} = (qn_i^2/N_A)(Se_{sc})$$

and the open-circuit voltage is:

$$V_{oc} = V_T \ln[J_{sc}/(J_{on}+J_{op})]$$

The highest voltage results with the lowest values of Se at the space-charge edge. Our model calculations show that a narrow back-field (~1 μm) is superior to the more typical wide BSF, provided that the back surface has a low recombination velocity, where "low" means smaller than the diffusion velocity, D_n/L_n, in the p^+ region.

Figure 1 illustrates the rationale behind our proposed approach. Referring to the BSF region in the figure, the upper curve is for a high surface recombination ohmic back while the lower two curves are for oxide-passivated backs. The lowest curve was obtained by lowering the BSF doping to $10^{19}/cm^3$, thus reducing the heavy doping effects. In the

base region the solid curves are for the lower lifetimes. It is clear that better performance would be obtained if the basewidth were reduced. The emitter in this example is a conventional high-surface-concentration phosphorus diffusion emitter, but the emitter surface is oxide-passivated.

Calculations indicate that high efficiency should be obtained with deep high-low emitter structures, provided the impurity profile at the n-p junction is very abrupt and the donor concentration is low enough to minimize heavy doping effects (i.e., $\sim 5 \times 10^{18}/cm^3$). While currently available experimental data do not agree well with the prediction, this is believed to be a result of excessively graded junction profiles. Although reduced emitter concentration is indicated, low emitter doping results in high sheet resistance and a deep emitter structure would provide substantial assistance in the design of an efficient contact grid and should be further investigated.

The contradictory requirements for passivating the surfaces while providing them with electrical contacts is approached in two ways. The first is to use a very small total area of actual ohmic contact, made by grid delineation through the passivating back oxide. This is less than ideal because of the difference between surface recombination velocity at the metal and that under the oxide (Figure 1). This translates into a difference of two orders of magnitude in the value of Se at the base boundary of the BSF region. Although the contact area is small, its effect is coupled to a very large volume of the base because of the large diffusion length. This situation can be substantially improved by employing tunneling MIS contacts.[5] While we do not at present have an effective explanation of the properties of such an interface, the passivation benefit seems real. MOS theory indicates that the contact properties depend on the metal-silicon barrier heights and require that the metal work functions be such as to result in a surface accumulation layer. This implies that the metal work function should be less than that of silicon for contact to an n-type layer (e.g., Al or Mg) and the converse for a p-type contact (e.g., Au, Pd, or Pt).

A final consideration involves the question of impurities. In the course of an intensive investigation of the effects of impurities on silicon and silicon solar cells conducted for JPL,[6,7] it was found that many impurities result in considerable lifetime degradation at concentrations in the parts per trillion range, well below the detection limits of practically every analytical method. An example of this behavior is shown in Figure 2 where, for molybdenum at a concentration of $10^{10}/cm^3$, cell efficiency is reduced from 15.35% to 14.9%. The effect is more pronounced for higher efficiency cells. This observation indicates that extreme care must be exercised to prevent contamination of the silicon both in processing and during purification and growth.

A benefit in impurity control may be obtained by using gallium as a primary p-type dopant. Gallium has a small effective segregation coefficient and will therefore remain in the melt at high concentrations during crystal growth. This may provide a degree of gettering for trap impurities. However, a more important reason for using gallium is the experimental fact that higher lifetimes are observed than in the case of comparable boron-doped material. It may also be conjectured that gallium acceptors will have a slightly higher threshold for bandgap narrowing because of their higher activation energies and a better fit in the silicon lattice.

2.2.3 Resistive Losses and Grid Design

We have developed a design model which minimizes the total energy losses of the contact system. The model has been verified experimentally for numerous designs. Included in the analysis are the losses due to metal coverage, ohmic losses in the emitter and the BSF layer, ohmic losses in the metal grid and back contact, ohmic losses in the metal-silicon interface (both front and back), and ohmic losses due to bulk base resistance. An example of grid design data is illustrated in Table 2.
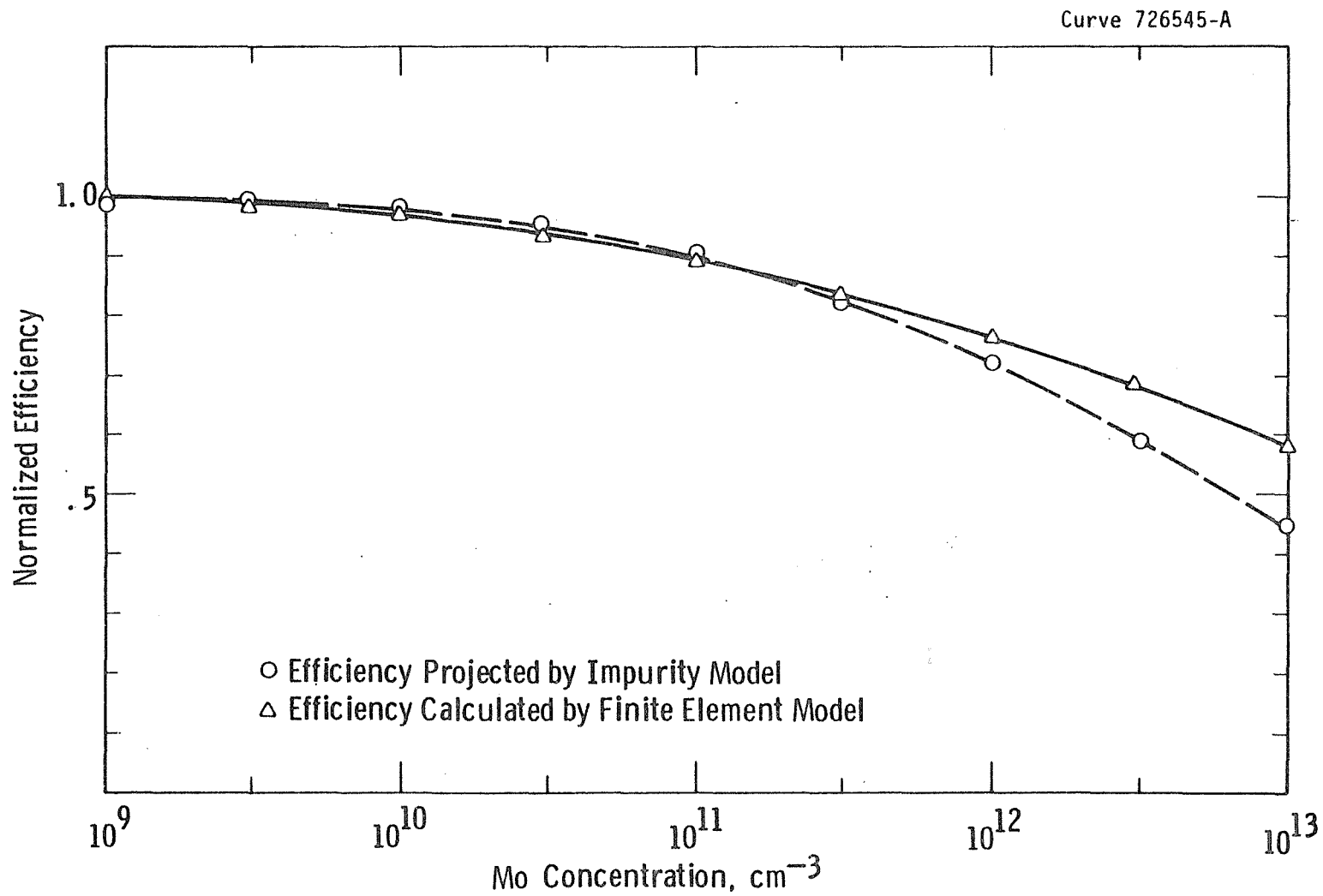
Figure 2. Calculated efficiency as a function of molybdenum
concentration for a narrow-base, back-surface field,
high-efficiency cell.

Table 2. Example Output of Contact Design Program

Cell Module: 1.0000 x 1.0000 cm Grid Module: 0.9000 x 0.9000 cm

Pad: 0.060 x 0.060 cm Number of Fingers: 11 Width: 5 µm

Thickness: 6 µm Diffused Sheet Resistance: 40 ohms/square

Metal Resistivity: 1.68 x 10^{-6} ohm-cm Base Resistivity: 4.00 ohm-cm

Base Width: 175 µm BSF Sheet Resistance: 60 ohms/square

Back Contact Area Coverage Factor: 0.0020 Contact Dot Radius: 10 µm

Number: 637 Specific Interface Resistance: 2.0 x 10^{-5} ohm-cm^2

Intrinsic Efficiency: 17.50% Light Current Density: 27.00 mA/cm^2

Corner Angle, θ_2 = 26.57

Energy Losses (LaPlace Solution)

Sheet: 0.029 mW Finger: 0.110 mW Shadow: 0.207 mW

Front Interface: 0.002 mW Base Loss: 0.096 mW

Back Contact Interface Loss: 0.000 mW Back Sheet Loss: 0.0484 mW

Total Joule Losses: 0.285 mW   Total Losses: 0.493 mW

Contact Coverage Area: 0.012 cm^2 (1.18%)

R_s = 0.213 ohms R_{sp} = 0.213 ohm-cm^2

Efficiency = 17.01%

2.2.4 Optical Losses

Use of a multilayer antireflective coating is capable of
increasing cell efficiency by about 5%. In addition, incorporation of
an optically reflecting back can minimize absorption losses resulting
from the narrow base. The reflector -- for example, a gold film deposit
on an oxide -- will be a highly efficient mirror for unabsorbed low-
energy photons. The design of an AR coating is complicated by the
presence of the passivating oxide. An example of the reflectance
calculations for this case is shown in Figure 3.
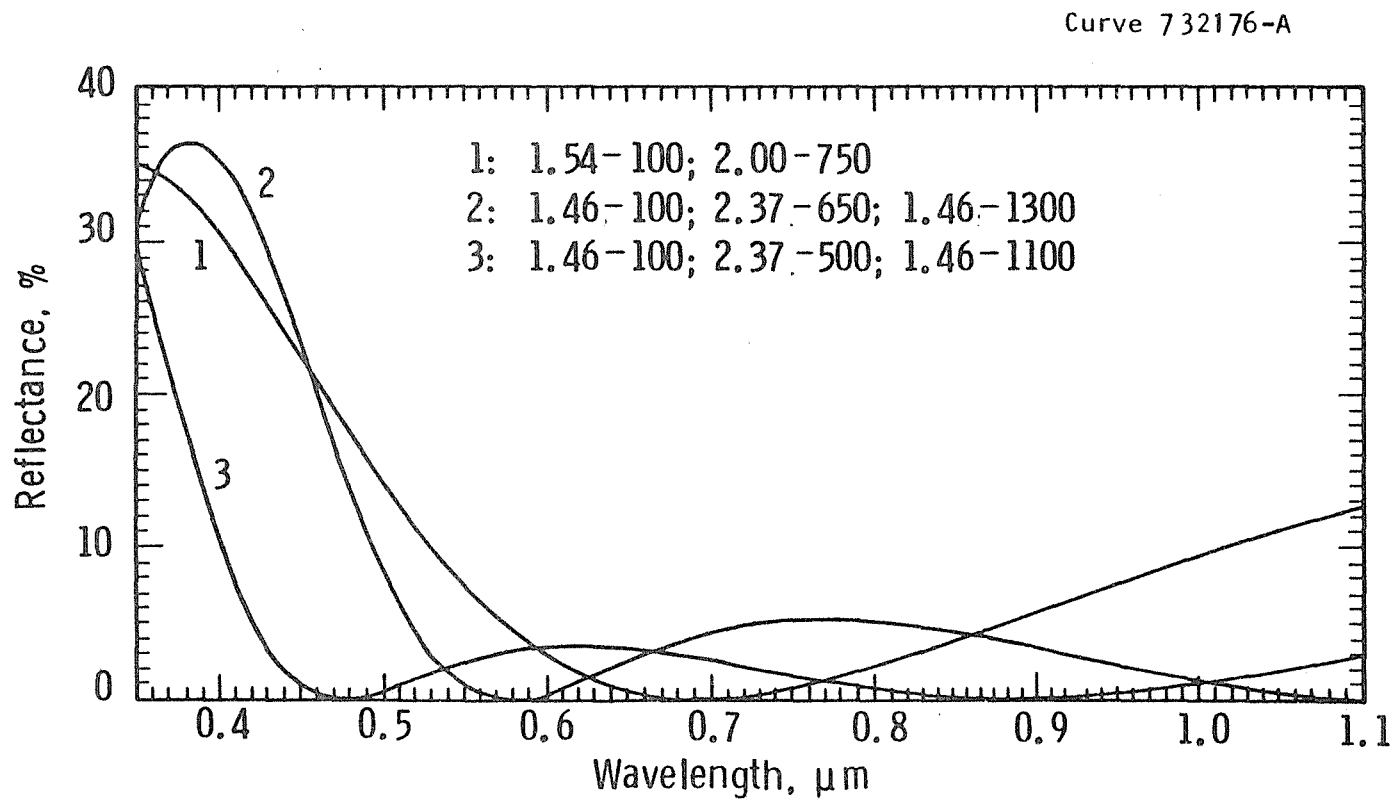
Figure 3. Reflectance data for two- and three-layer antireflective
coating designs for oxide-passivated surface. (The data
following the curve number in the legend represent the
refractive indices and thicknesses of the antireflective
coatings.)

2.3 Experimental Approach

The following subsections describe systematically our experimental approach for making high-efficiency solar cells. After selecting the right material, we have added features in our baseline cell design process to achieve AM1 cell efficiencies in excess of 17%.

2.3.1 Material and Dopant Selection

In addition to clever cell design, it is extremely important to select the proper starting material, dopants, and doping concentrations in all regions of the solar cell. The most important criterion for the starting material is high carrier lifetime (> 500 μs). For the highest efficiencies, such lifetimes must be obtained in low-resistivity material ($\sim$ 0.1 ohm-cm). We have used a high-quality float-zone silicon as our starting substrate. We have also made a few cells on 0.1 Ω-cm and 0.75 Ω-cm boron-doped float-zone silicon. Prior to advanced cell design or processing, we fabricated baseline n^+-p-p^+ type solar cells followed by carrier lifetime and DLTS measurements.

We have investigated the use of Ga as a dopant (in addition to the conventionally used boron) in the substrate material as well as in the p^+ region. Ga fits the silicon lattice better than boron and has an activation energy greater than that of boron; therefore, it may have less severe heavy doping effects. We used the Westinghouse open-tube gallium diffusion technique to form the p^+ region.[8] It is possible that Ga-doped crystals may even have higher carrier lifetimes because of the gallium-rich melt-assisted gettering (the segregation coefficient of Ga is several orders of magnitude smaller than that of boron).

With regard to the doping concentrations in the n^+ and p^+ regions, surface concentrations should be limited below 5 x 10^{19} cm^{-3}, and then a compatible contact grid should be designed to minimize the sheet resistance losses. Some attempts have been made to do this, although the majority of runs in this phase were done by straight $POCl_3$ and BBr_3 diffusions with high surface concentration.

15

2.3.2 Oxide Passivation

Our model dictates that it is necessary to passivate cell surfaces for higher open-circuit voltages; therefore, we have passivated the cell surfaces by growing a very thin layer of thermal oxide on top of n^+ and p^+ regions. We have opened an aperture pattern through the back oxide layer to establish communication between the back metal and the p^+ region and we have made some attempt to optimize the oxidation conditions and oxide thickness for the best results.

2.3.3 Oxide-Passivated Solar Cells with High-Low Emitter

Fabrication of a six-layer cell structure consisting of oxide-n^+-n-p-p^+-oxide could result in a further improvement over the oxide-passivated cell design. Our preliminary model calculations indicate that to gain the maximum benefit from this high-low emitter design, the n^+ region should be very shallow (< 0.1 μm) and the n region should be about 1 μm wide, with a doping density of less than 10^{18} cm^{-3} and diffusion length of several microns. The transition from n to p should be highly abrupt. It is possible to produce such a region by either atmospheric-pressure silane epitaxy or a reduced-pressure CVD technique. An attempt was made by epitaxial-growth to form an n-region and further work is in progress.

2.3.4 Oxide-Passivated Cells with High-Low Emitter and MIS-Type Contacts

In this cell design use of all the above-mentioned features along with a very thin layer of oxide (< 30 Å) underneath the front and back contact metals is proposed. Thus, the contact regions have an MIS structure with very thin oxide. This avoids direct metal-to-silicon contact to keep the surface recombination velocity of silicon low. The important requirements are that the oxide layer should be thin enough to keep the tunneling impedance low and that its oxide quality should be good enough to offer surface passivation. Green[5] has shown that it is possible to grow such an oxide layer, although it requires clever

contact grid design to minimize losses.   Attempts are in progress to make such a structure.

2.3.5   Oxide-Passivated Cells with Multilayer AR Coating and Reflective Back Metal

Use of multilayer antireflective coatings and reflective back metal contact can enhance the oxide-passivated cell performance. Initial model calculations (described in Section 2.2.1) indicate that the reflective losses can be minimized by using a multilayer AR coating in place of the conventionally used single-layer coating with a refractive index of ~ 2.   Similarly, if we make very thin-base solar cells, we can gain from a reflective back mirror to contain the light. Plasma-deposited Si_xN_y coatings have been formed with varying refractive index in the range of 1.5-3.8.   Solar cells with single layer coatings has been fabricated, and multilayer coatings are being investigated.

3. TECHNICAL PROGRESS

3.1 Model Calculations and Discussion

We have developed a simplified analytical model which provides useful insight and guidelines for fabricating high-efficiency solar cells. The model includes the effect of bandgap narrowing, Auger recombination, and recombination at the device surfaces, but it neglects the electric field effects resulting from the gradient of doping concentrations.[9,10]

The model is based on the use of an internal recombination velocity as a measure of the minority-carrier losses in the various regions of the device. This directly provides the junction saturation current and thus the dark voltage-current characteristic which exerts primary control over cell performance. It is apparent that the major benefit of reducing recombination is the increase in open-circuit voltage, V_{oc}, which follows from reductions of the saturation current, J_o.

Solar cell efficiency is directly proportional to the open-circuit voltage and the short-circuit current. Both, of course, are subject to recombination losses, but here we will only concentrate on the variation of V_{oc}. Open-circuit voltage is inversely related to the saturation current (J_o).

$$V_{oc} = V_T \ln \left[1 + \frac{J_{sc}}{J_o} \right] \tag{1}$$

$$J_o = J_{ob} + J_{oe} = \frac{qn_i^2}{N_A} \cdot \frac{D_n}{L_n} \left[\frac{S_n \cosh \left(\frac{W_b}{L_n}\right) + \frac{D_n}{L_n} \sinh \left(\frac{W_b}{L_n}\right)}{\frac{D_n}{L_n} \cosh \left(\frac{W_b}{L_n}\right) + S_n \sinh \left(\frac{W_b}{L_n}\right)} \right]$$

$$+ \frac{qn_i^2}{N_D} \cdot \frac{D_p}{L_p} \left[\frac{S_p \cosh \left(\frac{W_e}{L_p}\right) + \frac{D_p}{L_p} \sinh \left(\frac{W_e}{L_p}\right)}{\frac{D_p}{L_p} \cosh \left(\frac{W_e}{L_p}\right) + S_p \sinh \left(\frac{W_e}{L_p}\right)} \right] \tag{2}$$

(D_n, L_n) and (D_p, L_p) are the diffusivity and diffusion length of the minority carriers in the p-base and n^+ emitter region, W_b and W_e are the base and emitter widths beyond the junction edges, S_n and S_p are the surface recombination velocities at the front of the n^+ emitter region and back of the p-base region, respectively, and J_{ob} and J_{oe} are the base and emitter contribution to the reverse saturation current.[10]

The recombination at the silicon surface can be reduced by introducing a low-high junction[11-14] or by growing an oxide layer. A detailed analysis of low-high structures by Gunn[15] provides a beginning place for our model. The starting expression for the present discussion is an equation, derived from the carrier transport equations which transform the surface recombination velocity of the device (S_o) to an effective recombination velocity seen by minority carriers at the low side of the low-high interface as a function of the properties of the low and high regions. This equation for a p-p^+ structure is:

$$ S_e = \frac{n_p^+}{n_p} \frac{D_n^+}{L_n^+} \cdot \frac{\dfrac{S_o L_n^+}{D_n^+} + \tanh\left(\dfrac{W_p^+}{L_n^+}\right)}{1 + \dfrac{S_o L_n^+}{D_n^+} \tanh\left(\dfrac{W_p^+}{L_n^+}\right)} \tag{3} $$

where n_p^+, L_n^+, D_n^+ = concentration, diffusion length, and diffusivity of the minority carrier in the heavily doped p^+ region.

W_p^+ = width of the heavily doped region.

S_o = surface recombination velocity at the back of the high region.

S_e = effective recombination velocity at the low side of the low-high junction.

n_p = minority-carrier concentration in the low region.

We introduce the necessary modifications in the above expression to include the effects of degeneracy and bandgap narrowing. We have devised an empirical expression for the effective bandgap narrowing, (ΔV_G) based on the data of Lanyon[16] and Lindholm[17] corrected for degeneracy effects. The values thus adjusted for Fermi statistics can be used in the usual Boltzman expression for the np product, i.e.,

$$np = n_{ie}^2 = \exp \frac{(\Delta V_G^+ - \Delta V_G^-)}{V_T} n_i^2$$

where ΔV_G^+ and ΔV_G^- are the effective bandgap narrowing in the high and low regions, respectively.

$$\Delta V_G = 0.231 \left[\left(\frac{10^{20}}{N} \right)^{3/4} + 1 \right]^{-2/3} \tag{4}$$

and

$$n_i^2 = N_c N_v \exp \left(-\frac{E_G}{V_T} \right)$$

Equation 3 can now be written as:

$$S_e = \frac{N_A}{N_A^+} \frac{D_n^+}{L_n^+} \exp \left(\frac{\Delta V_G^+ - \Delta V_G^-}{V_T} \right) \frac{\frac{S_o L_n^+}{D_n^+} + \tanh \left(\frac{W_p^+}{L_n^+} \right)}{1 + \frac{S_o L_n^+}{D_n^+} \tanh \left(\frac{W_p^+}{L_n^+} \right)} \tag{5}$$

Empirical expressions were derived to relate the diffusion length and diffusivity to the impurity concentrations (N).

The expression for D was obtained from the data of Conwell as given in Grove.[18]

$$D = \frac{D_o}{1 + \left(\frac{N}{10^{17}} \right)^{0.6}} + A_o \tag{6}$$

where for p-type

$$D_o = D_{no} = 35$$

$$A_o = 1.8$$

and for n-type

$$D_o = D_{po} = 12.5$$

$$A_o = 1$$

The diffusion length is obtained using a Kendall's lifetime function[19] for bulk silicon (τ_K) combined with Beck and Conradt's[20] data for Auger recombination τ_A.

$$\tau_n = \left(\frac{1}{\tau_A} + \frac{1}{\tau_K}\right)^{-1} \tag{7}$$

where

$$\tau_K = \frac{\tau_o}{1 + \frac{N}{7 \times 10^{15}}} \tag{8}$$

Note the value chosen for τ_o is related to the quality of silicon. We have found that a value of 200 to 400 µs for τ_o is more appropriate for modeling high-performance devices.

The Auger lifetime is given by:

$$\tau_A = \frac{1}{(K_A \cdot 10^{-31})N^2} \tag{9}$$

where K_A = 1.2 for p-type
K_A = 2.8 for n-type

Then the diffusion length is obtained from:

$$L = \sqrt{D\tau} \tag{10}$$

21

It should be noted that the derivation of Equation 5 is completely general in that it may be applied to the calculation of an effective recombination velocity across an arbitrarily chosen region anywhere in the device as, for example, within the base region where the doping is constant. In this case we set $N_A = N_A^+ = N_A(base)$. This velocity then characterizes the total recombination beyond this plane.

Assuming appropriate recombination velocity on the cell surface as the boundary conditions and from known doping profiles, we can now iteratively apply this calculation using Equation 5 from the back surface, across the base to the edge of the depletion region, and thus account for all the recombination processes in the base and back by calculating S_{ejb}. A similar calculation for the n region above the junction can give S_{ejb}. Relating Equation 2 in terms of S_e as given in Equation 5 permits expressing the base and emitter component of the saturation current density as:

$$J_o = J_{ob} + J_{oe} = (qn_i^2/N_A)S_{ejb} + (qn_i^2/N_D)S_{eje} \qquad (11)$$

where (S_{ejb},N_A) and (S_{eje},N_D) are the recombination velocities and doping densities at the edges of the depletion region. Then, neglecting current contributions from the depletion region,

$$V_{oc} = V_T \ln \left(\frac{J_{sc}}{J_{on} + J_{on}}\right) \qquad (12)$$

Figure 1 shows the results of model calculations for a back-surface field solar cell using three different back-surface field (BSF) structures with two different base diffusion lengths. In Figure 1 recombination velocity is plotted as a function of distance into the n^+-p-p^+ solar cell. Referring to the BSF region in the figure, the upper curve is for a high recombination ohmic back ($S_o = 10^6$ cm/sec), while the lower two curves are for the oxide-passivated backs with reduced S_o. The lowest curve was obtained by lowering the BSF surface-

doping concentration to 10^{19} cm^{-3}, thus reducing the heavy doping effects. In the 4 Ω-cm base region, the solid curves are for a lower base diffusion length of 209 μm while the dotted curves are for longer base diffusion length of 467 μm. In this example we have assumed a diffused emitter with high-surface concentration with the emitter surface passivated (S$_o$ ~ 500 cm/sec).

If the emitter surface is not passivated in this 4 Ω-cm cell, the $S_{eje} \gg S_{ejb}$, $J_{oe} \gg J_{ob}$, and V_{oc} is limited by J_{oe}. Model calculations in Figure 1 show that with the emitter surface passivated, $S_{eje} \gtrsim S_{ejb}$, but due to much higher doping density in the emitter (~ 10^{17} cm^{-3}) at the edge of the depletion region[4] compared to the base doping (3.5 $\times$ 10^{15} cm^{-3}), $J_{ob} \gg J_{oe}$. Therefore, with emitter surface passivation, J_{ob} limits J_o. Now both S_{ejb} and the reverse saturation current can be reduced further by back-surface passivation or lower BSF doping (Figure 1) to gain additional increase in V_{oc}. Figure 1 shows that a long diffusion length (L > 3W) in the finished device is necessary to realize this benefit of back-surface passivation and lower BSF doping, otherwise S_{ejb} is limited by the diffusion velocity (D/L) of the carriers in the base. Calculations also indicate that for a diffusion length of 467 μm, with both surfaces passivated, a V_{oc} of 599 mV, J_{sc}[21] of 37 mA/cm^2, and a cell efficiency of 17.4% can be obtained. If the surface concentration of the BSF region is reduced to 10^{19} cm^{-3}, then a V_{oc} of 605 mV and a cell efficiency of 17.8% can be achieved on this 4 Ω-cm substrate.

Use of a lower resistivity substrate[22] with similar diffusion length can further reduce the base component of the reverse saturation current and thus give greater improvements in V_{oc}. The design of the emitter could be more important for the low-resistivity substrate because J_{oe} may dominate J_o, even after front-surface passivation. Reduced doping in the emitter can lower J_{oe} further and provide additional gain in V_{oc}. A similar effect of doping concentration is shown in Figure 1 for the heavily doped p$^+$ region when J_{ob} dominates J_o.

3.2 Baseline Material Selection and Qualification

In this program we selected a 4 ohm-cm, p-type, boron-doped, (111) float-zone silicon grown with zero dislocation density as a baseline material. These wafers are 2 inches in diameter and ~10 mils thick. The front side is chem-mechanically polished and the back side is chemically etched. This crystal was grown at Monsanto and is supposed to have high minority-carrier lifetime.

In order to evaluate the material quality ourselves we fabricated 30 mil diameter Schottky barrier diodes on the wafers by evaporating Ti-Au contacts to perform DLTS measurements. Deep-level transient spectroscopy (DLTS) is a capacitance transient technique which is used to detect the deep levels that may degrade carrier lifetime in semiconductors. The capacitance transients are generated from the deep levels by applying voltage pulses repetitively to a reverse-biased depletion region of the device. This technique is well-documented in the literature.[23-24] Figure 4 shows a schematic diagram of our DLTS set-up which uses a lock-in amplifier and Boonton capacitance meter.

Figure 5 shows DLTS spectra for the baseline float-zone silicon. There are no detectable deep levels in this material because no peaks were observed in the spectra. It is important to recognize that the DLTS detection limit for 4 ohm-cm material is 3.5×10^{11} cm^{-3}; therefore, lifetime-killing centers with lower than 3.5×10^{11} cm^{-3} concentration will not show up in this spectra. Since $\tau_r \approx \frac{1}{\sigma N_t V_{th}}$ (where τ_r is the recombination lifetime, σ is the capture cross section of the deep level, N_t is deep-level concentration, and V_{th} is the thermal velocity of carriers ($\sim 10^7$ cm/sec), the DLTS data suggest that if there are deep levels with $N_t \leqslant 3.5 \times 10^{11}$ cm^{-3}, then the lifetime of this material would be greater than 300 µsecs provided the minority-carrier capture cross section of those deep levels is smaller than 10^{-15} cm^2.

In another experiment we determined the minority-carrier generation lifetime in this float-zone silicon by fabricating MOS
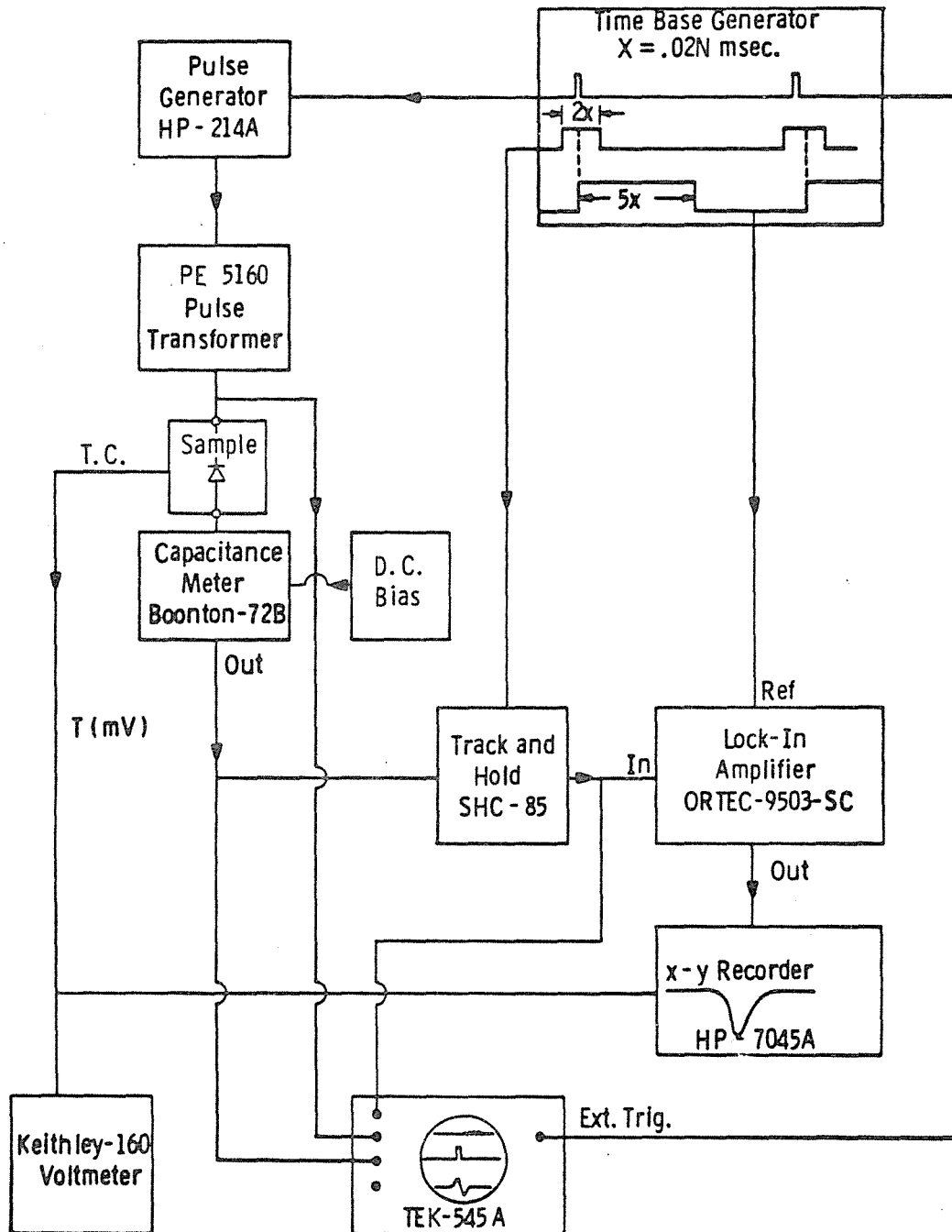
Figure 4. Schematic diagram of the DLTS set-up.
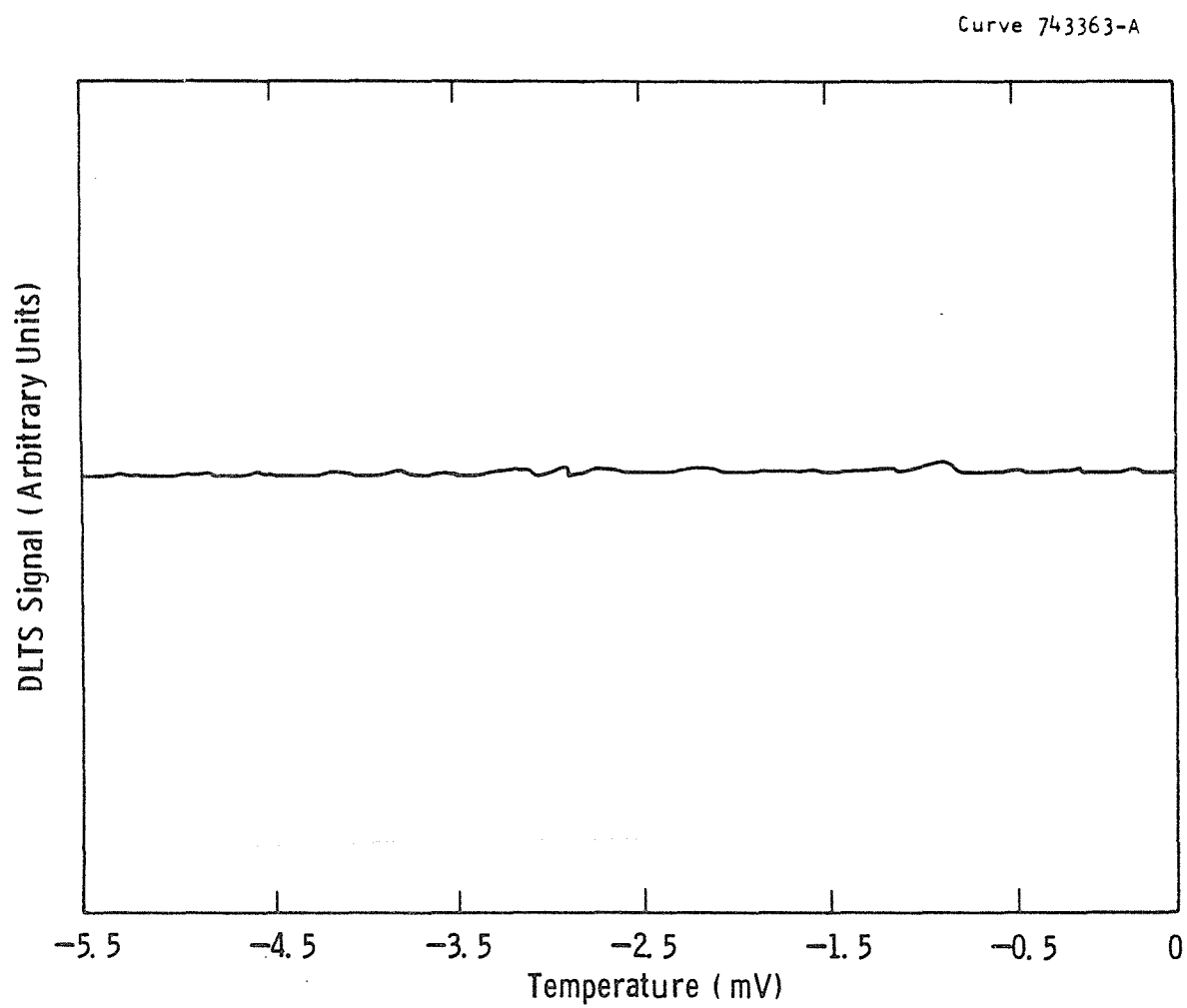
Figure 5. DLTS spectra for the baseline 4 ohm-cm float-zone silicon.

capacitors. The wafers were first oxidized at $1100^{\circ}C$ for 1 hour in pure O_2, then in-situ annealed for 20 min in N_2 at $1100^{\circ}C$, and finally slow-cooled at a rate of $1^{\circ}C/min$. Aluminum metal dots were evaporated followed by a $450^{\circ}C/30$ min sintering in H_2. The generation lifetime (τ_g) was determined by the pulse MOS technique in which MOS capacitors are pulsed from inversion into deep depletion and the recovery to inversion is recorded as a function of time (Figure 6). This technique is well-documented in the literature.[25] Figure 5 shows the typical c-t curve for these samples which gave us a generation lifetime of 350 µsecs. It should be pointed out that the generation lifetime (τ_g) and the recombination lifetime (τ_r) are equal only when the lifetime-controlling deep center lies in the middle of the bandgap:

$$\tau_g = \tau_r \exp\left(|\Delta E|/KT\right)$$

where ΔE is the energy difference between the deep level and the mid-gap.

3.3 Baseline n^+-p-p^+ Solar Cells on 4 ohm-cm Float-zone Silicon

To verify the material quality, a large number of 1 cm x 1 cm n^+-p-p^+ solar cells were fabricated on 4 ohm-cm float-zone silicon by $850^{\circ}C$ $POCl_3$ diffusion for a n^+ emitter and $950^{\circ}C$ BBr_3 diffusion for a p^+ back-surface field. The process sequence for fabricating n^+-p-p^+ solar cells is shown in Table 3. Solar cell data consisting of short-circuit current density, open-circuit voltage, fill factor, and cell efficiency are shown in Table 4. All cells were tested under 100 mW/cm^2 AM1 illumination using a quartz-iodine lamp.

The data in Table 4 show that the short-circuit current density (I_{sc}) is about 33 mA/cm^2 and the open-circuit voltage is in the range of 575-585 mV. Average solar cell efficiency is ~ 14.75% with the maximum exceeding 15%.
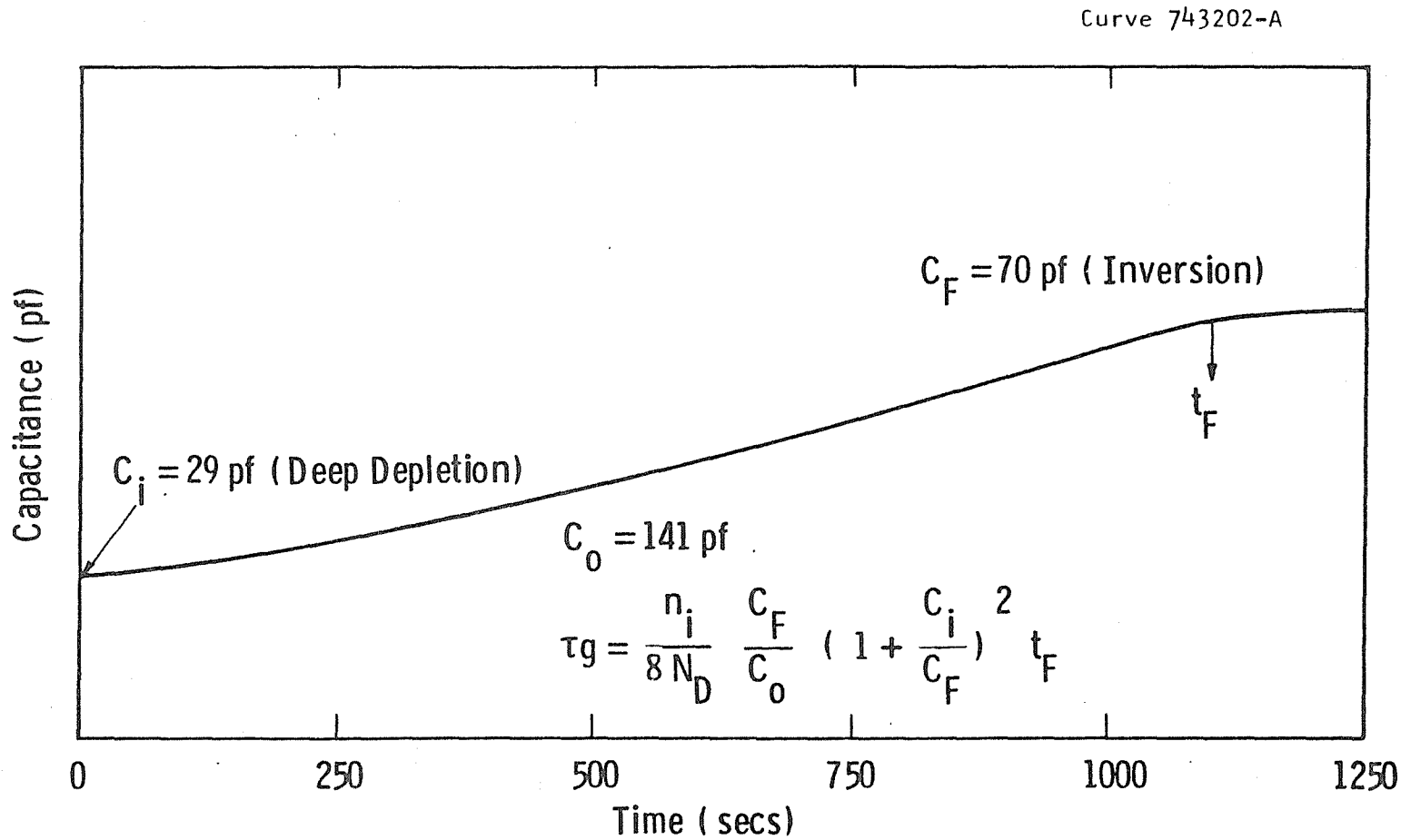
Figure 6. Capacitance versus time curve for determining the minority-carrier generation lifetime in baseline float-zone silicon.

Table 3. Sequence for Fabricating n^+-p-p^+ Solar Cells

Wafer clean

Silox deposition to cap emitter side

Clean

BBr_3 diffusion to form p^+ back surface field

Oxide removal

Silox deposition on p^+ region

Clean

$POCl_3$ diffusion to form n^+ emitter

Oxide removal

Pre-metal deposition clean

Front and back metal evaporation

Apiezon wax to protect back metal

Photoresist front side and expose grid patterns

Metal etch

Photoresist front and expose mesa around
   grid patterns

Silicon etch

Contact sintering

Test

Anti-reflective coating on front

Test

3.4 Cell Testing With and Without a Metal Mask

Figure 7 shows that our cell configuration consists of twelve
1 cm x 1 cm solar cells on two-inch diameter wafers. An 8 to 10 μm deep
mesa is etched around each cell to isolate it. In order to verify that
we are not collecting any appreciable current from the etched bare-
silicon region between the cells, we tested a few cells by placing a
metal mask on top of the wafer. The mask was painted black and had a
precise 1 cm x 1 cm window so that by proper placement or alignment, only

Table 4. Solar Cells (n^+-p-p^+) Fabricated on Baseline
4 ohm-cm Float-Zone Silicon

Cell ID	Short-Circuit Current J_{sc} mA/cm^2	Open-Circuit Voltage V_{oc} Volts	Fill Factor	Cell Efficiency %
1	33.5	0.582	0.767	14.9
2	33.3	0.582	0.767	14.8
3	33.1	0.584	0.756	14.6
4	33.2	0.582	0.781	15.1
5	33.4	0.582	0.777	15.1
6	33.0	0.579	0.780	14.9
7	32.9	0.582	0.786	15.0
8	33.2	0.579	0.776	15.0
9	33.6	0.577	0.763	15.0
10	33.0	0.579	0.777	14.9
11	32.9	0.581	0.772	14.7
12	32.9	0.581	0.752	14.4

Run: M-7, Wafer B-1

100 mW/cm^2 AM1 illumination

one cell is exposed to the light during testing. Table 5 shows that with and without the metal mask, the difference in J_{sc} and cell efficiency is less than 2%; this is within the experimental error of measurement and the manual alignment of the metal mask, although without the metal mask absolute cell efficiencies appear to be 0.2 to 0.3% higher.

3.5 Oxide-Passivated 17.2% Efficient Solar Cells on 4 Ω-cm Float-Zone Silicon

Following the guidelines of our model, the solar cell surfaces were passivated by growing a thermal oxide at 800°C. The oxide thickness on top of the n^+ region was about 110 Å and on top of the p^+ region

30
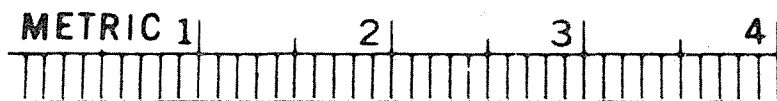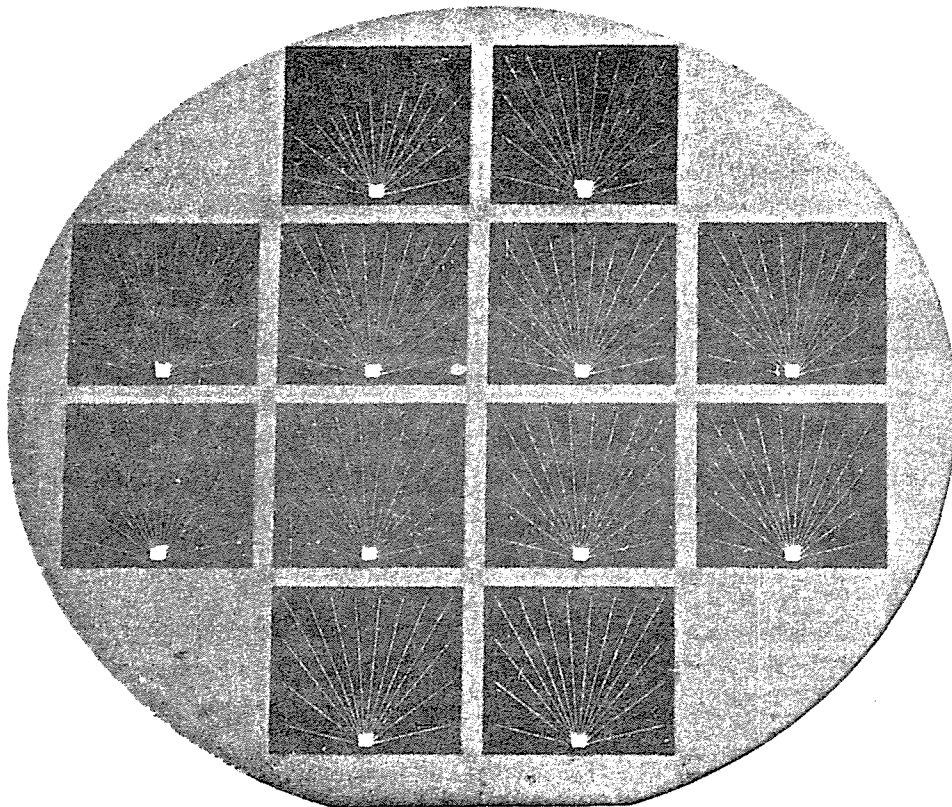
Figure 7. Cell configuration.

31

Table 5. Cell Testing With and Without the Metal
Mask with 1 cm x 1 cm Window

Cell No.	Without Metal Mask			With Metal Mask		
	J_{sc} (mA/cm^2)	V_{oc} (volts)	η %	J_{sc} (mA/cm^2)	V_{oc} (volts)	η %
1	34.9	.588	16.0	33.7	.590	15.7
2	34.9	.589	16.0	34.4	.591	15.9
3	35.4	.596	16.5	34.9	.596	16.2
4	35.0	.594	16.4	34.0	.596	16.1
5	35.1	.594	16.3	34.5	.596	16.1

it was ~ 45 Å. A grid pattern was opened through the back oxide.
Figure 8 shows a schematic diagram of the oxide-passivated cell, while
the process sequence for the oxide-passivated cells is shown in
Table 6. In this sequence we slow-cooled all the high-temperature steps
at a rate of 1°C/min to preserve the bulk lifetime. In addition,
phosphorus was diffused through a very thin oxide to preserve the
surface quality. Front and back contacts were Ti-Pd-Ag and the
TiO_2/SiO_2 antireflective coating was spun on these cells prior to
photolithography and metallization. Our cell design ($O-n^{+}-p-p^{+}-O$),
coupled with careful cell processing and controlled AR coating
deposition, has resulted in cell efficiencies in excess of 17% with a
maximum of 17.2%. These cells were tested and verified at SERI. As
shown in Table 7, our measurements gave V_{oc} of 600 mV, J_{sc} of
36.2 mA/cm^2, fill factor of 0.793, and cell efficiency of 17.2%. SERI
measurements on the same cell gave V_{oc} of 604 mV, J_{sc} of 35.6 mA/cm^2,
fill factor of 0.795, and cell efficiency of 17.11%.

3.5.1 Ellipsometric Measurements on 17.2% Efficient Cells

A Rudolph Auto-EL ellipsometer was used to determine the initial
oxide thickness and the thickness of spin-on AR coating on the 17% .
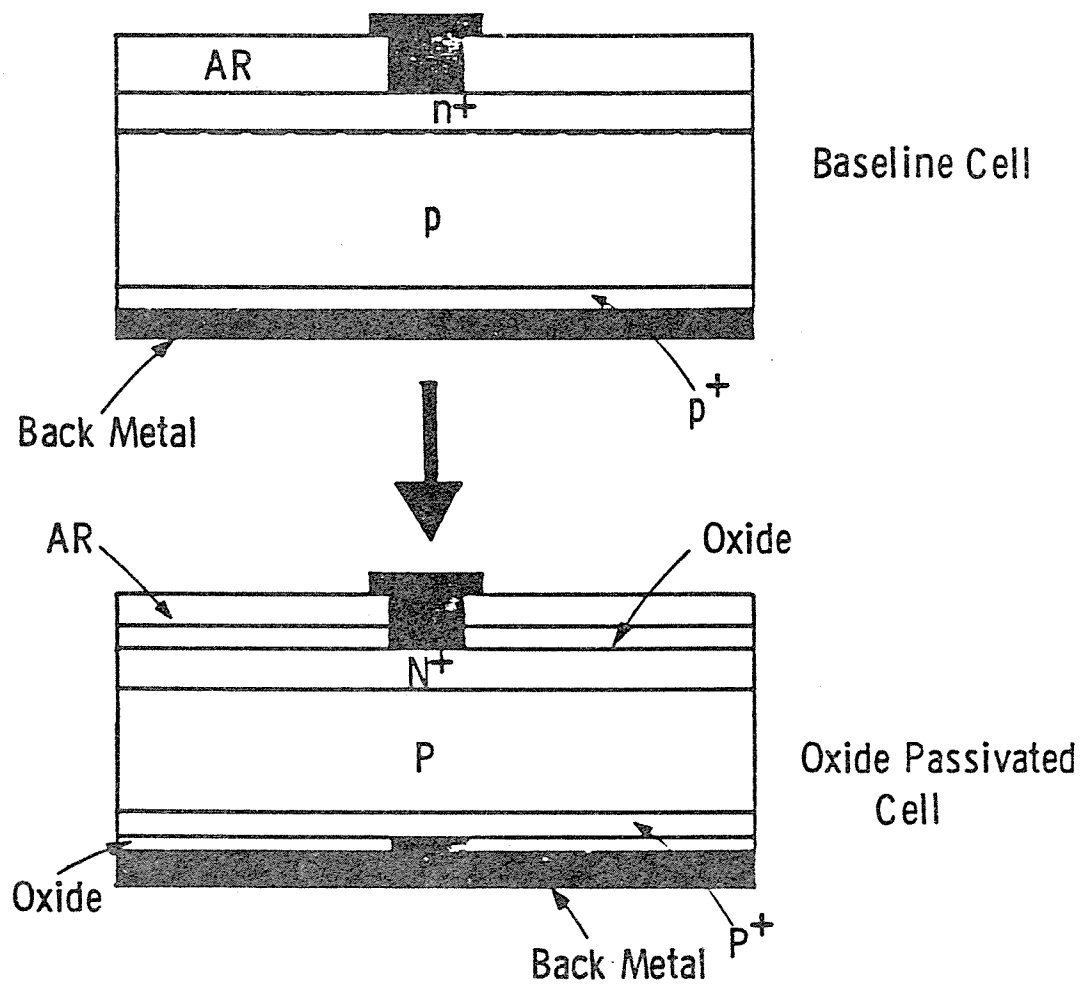
Figure 8. Schematic diagram of oxide-passivated cells.

33

Table 6. Process Sequence for Fabricating
         Oxide-Passivated Solar Cells

Clean

Silox deposition to cap emitter side

Clean

BBr_3 diffusion to form p^+ back-surface field

Oxide etch

Silox deposition p^+ region

$POCl_3$ diffusion to form n^+ emitter

Oxide etch

Clean

Oxidation – passivation

Anti-reflective coating on n^+ side

Photoresist both sides

Expose grid pattern on both sides

Antireflective coating etch

Oxide etch

Evaporate metal on front side

Reject metal/remove PR from the back

Evaporate back metal

Build front metal thickness by electroplating Ag

Photoresist front side and expose mesa mask around
    grid patterns

Protect back by apiezon wax

Etch AR coating

Etch silicon for mesa

Remove wax from back

Remove photoresist from front

Test

Sinter contact

Test

Table 7. Oxide-Passivated Solar Cells on
Boron-Doped 4 Ω-cm Float-Zone Silicon

Cells Tested at Westinghouse

Cell ID	Area (cm^2)	J_{sc} (mA/cm^2)	V_{oc} (mV)	FF (%)	η (%)
HIEFY 4-4	1.0	36.1	599	79.4	17.1
-5	1.0	36.2	600	79.3	17.2
-6	1.0	36.4	598	78.5	17.1
-7	1.0	36.2	599	79.1	17.2
-8	1.0	36.3	597	79.5	17.2

Above Cells Tested at SERI

HIEFY 4-4	1.01	35.5	604	79.6	17.1
-5	1.01	35.6	604	79.5	17.1
-6	1.01	35.9	605	78.6	17.1
-7	1.01	35.4	604	79.7	17.0
-8	1.01	35.3	603	79.8	17.0

*AM1, 100 mW/cm^2 Illumination

*Run #HIEFY 4, Base 2

efficient cells. Just after the oxidation step the measured front oxide thickness was 110 Å and the back oxide was ~ 50 Å thick. After complete cell fabrication, ellipsometric measurements were made with the help of a computer program for two-layer coatings since the AR coating consists of a thin SiO_2 layer underneath the spin-on coating. The measurements show that the AR coating of a 17.2% efficient cell consists of an oxide thickness of 112 Å with a refractive index of 1.458, and a spin-on anti-reflective coating on top of this oxide with a thickness of 555 Å and a refractive index of 2.03.

3.5.2 I-V Analysis of the 17.2% Efficient Cells

Dark I-V measurements[26] were performed in conjunction with the lighted I-V data to obtain resistances, bulk recombination, and junction recombination components. An effective base lifetime is calculated from J_o using an approximation $J_o = \frac{qn_i^2}{N_A} \sqrt{\frac{D}{\tau_{eff}}}$. Notice that in this calculation, surface effects are neglected; also, it is assumed that J_o is dominated by the base, which may not necessarily be the case. As discussed in Section 3.3.6, for these 4 Ω-cm material cells, $J_o \sim J_{oe}$ without any passivation; however, after front-surface passivation, J_o becomes dependent upon J_{ob} ($J_{ol} = J_{oe} + J_{ob}$). The I-V analysis and its approximations are described in detail in the second quarterly report.[27]

Table 8 shows the comparison of cell parameters of a 15.2% baseline n^+-p-p^+ cell and the counterpart oxide-passivated 17.2% cell. We observe a 2.8 mA increase in J_{sc}, 17 mV increase in V_{oc}, and about a factor of 1.85 decrease in J_{ol}. Dark and lighted I-V curves taken at SERI on a 17.2% cell are shown in Figures 9 and 10, respectively. There is reasonable agreement between the lighted and dark I-V data taken at Westinghouse and SERI. We generally measure slightly lower open-circuit voltage because of the lack of temperature control during cell testing.

3.5.3 Reflectivity and Spectral Response Measurements on 17.2% Efficient Cells

Our equipment for reflectivity and spectral response measurements includes a tungsten halogen light source, a manochrometer, and a silicon photodetector.[27] Photocurrent from the cell is compared automatically to that from a standard silicon detector of calibrated spectral response. Reflectivity and relative spectral response of the 17.2% cell is shown in Figure 11. Absolute spectral response (amps/watt) is obtained by:

$$\frac{\text{Relative Spectral Response x Standard (A/W)}}{1-R(\lambda)} \qquad (13)$$

Table 8. A Comparison of the Cell Parameters of a Baseline
n^+-p-p^+ Cell and 17.2% Oxide-Passivated Cell
Fabricated on 4 Ω-cm Float-Zone Silicon

Parameter	Baseline n^+-p-p^+ Cell	17.2% Oxide-Passivated Cell
J_{sc}	33.4 mA/cm^2	36.1 mA/cm^2
V_{oc}	583	600
FF	.78	.794
η	15.2%	17.2%
R_s	0.5 Ω-cm^2	0.21 Ω-cm^2
R_{sh}	104 kΩ-cm^2	190 kΩ-cm^2
J_{o1}	3.7 x 10^{-12} A/cm^2	2 x 10^{-12} A/cm^2
τ_{eff}	213 μsecs	709 μsecs
J_{o2}	1.7 x 10^{-7} A/cm^2	7.7 X 10^{-7}

From these data, internal quantum efficiency, $Q_{E(\lambda)}$, as a function of
wavelength is determined according to:

$$Q_{E(\lambda)} = \frac{hC}{q\lambda} \cdot \text{Absolute Spectral Response} \qquad (14)$$

Internal quantum efficiency is defined as the ratio of the number of
collected electrons to the number of photons entering the material at a
given wavelength per unit time.[10]
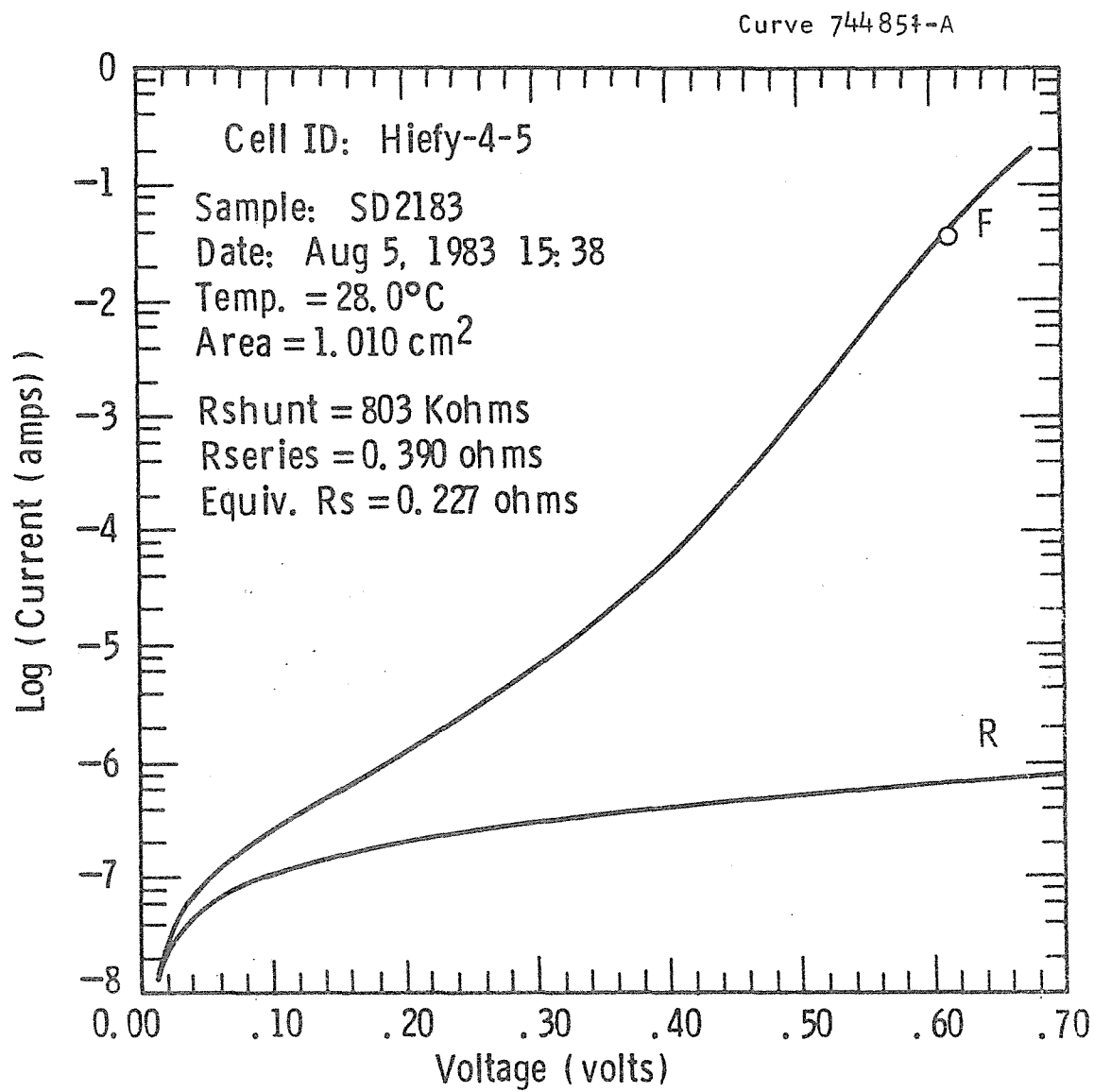
Figure 9. Dark I-V data taken at SERI on a 17.2% oxide-passivated cell on 4 Ω-cm float-zone silicon.

38
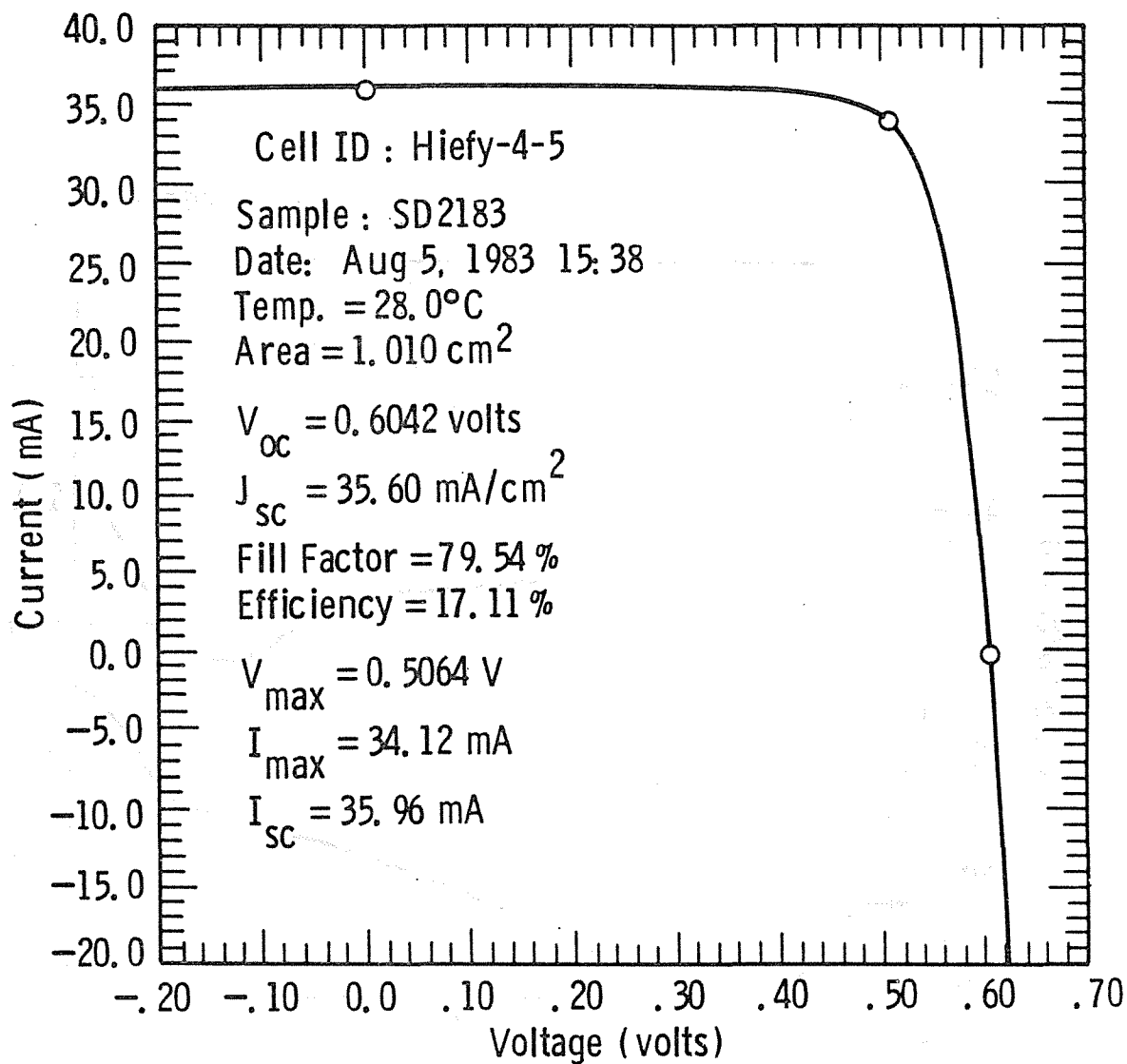
Figure 10.   Lighted I-V data taken at SERI on a 17.1% oxide-passivated cell fabricated on 4 Ω-cm float-zone silicon.
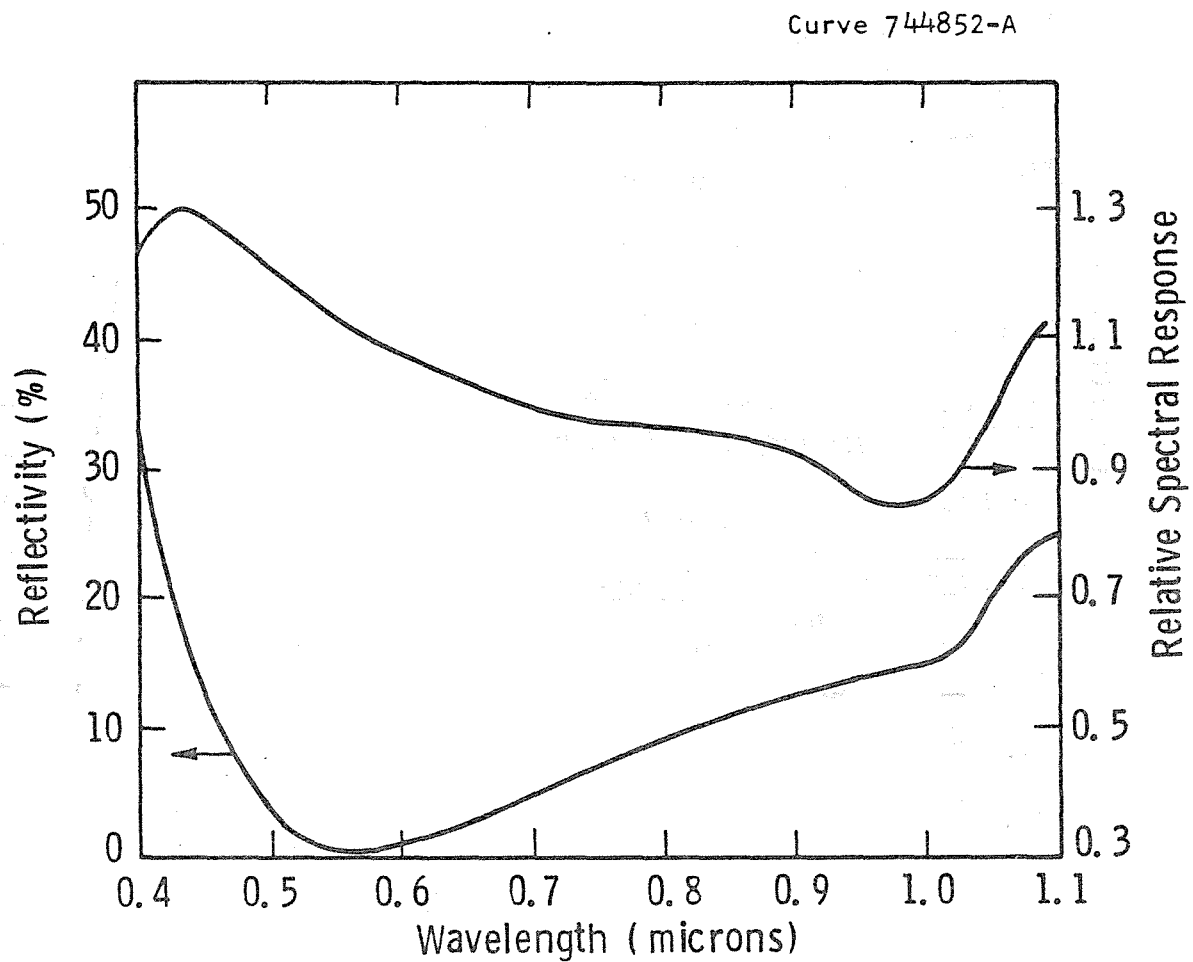
Figure 11. Reflectivity and relative spectral response of a 17.2% efficient oxide-passivated cell on 4 Ω-cm silicon.
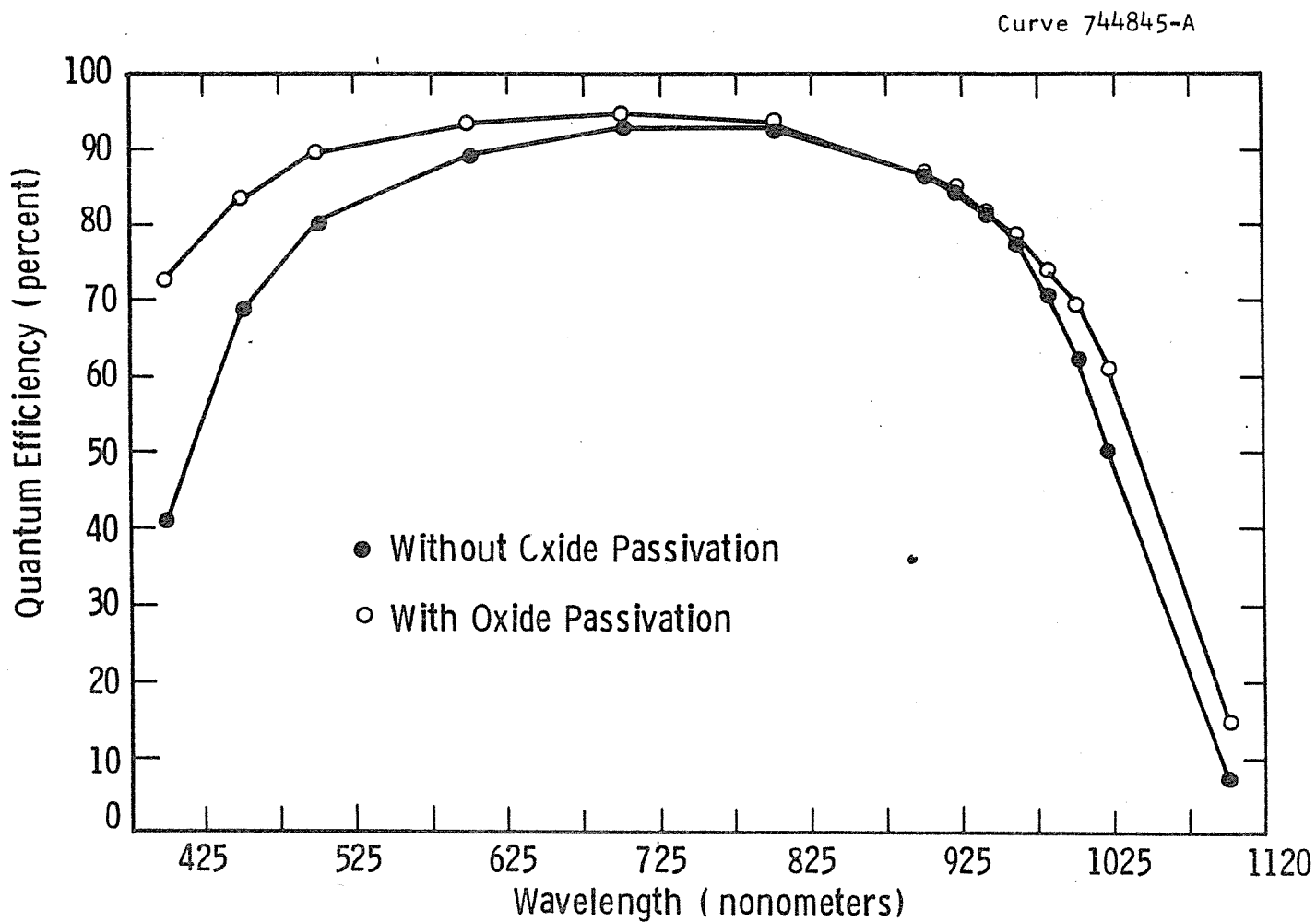
Figure 12. Quantum efficiency versus wavelength plot for an
unpassivated cell and 17.2% efficient oxide-passivated cell
on 4 Ω-cm float-zone silicon.

41

Figure 12 compares the quantum efficiency of the oxide-passivated 17.2% efficient cell and the counterpart 15.2% efficient n^+-p-p^+ cell without any oxide passivation. The data clearly verify the benefits of oxide passivation. We observe a very significant increase in the quantum efficiency at the shorter wavelengths (0.4 - 0.55 μm) which are primarily absorbed in the emitter. (At a wavelength of 0.4 μm, the absorption length is ~0.1 μm.) This supports the fact that the front oxide reduces the loss of carriers to the front surface. The data show that even at 0.4 μm the quantum efficiency can be raised from 0.4 to 0.72 by proper surface passivation, which means that a majority of photogenerated carriers near the emitter surface are not lost due to its bulk recombination properties (Auger recombination and bandgap narrowing), but a very significant number are lost into the front surface. Thus, the emitter region should not be regarded as a dead layer because even for 0.3 μm deep junctions, the quantum efficiency of the light absorbed in the emitter can be made greater than 75% by proper oxide passivation.

Figure 12 indicates that the quantum efficiency in the wavelength range of 0.75 to 0.95 μm is nearly the same. In this range, most light is absorbed within the bulk of silicon, away from surfaces, because absorption length is in the range of 15 to 60 μm. This suggests that oxide passivation has apparently not changed the true diffusion length in the base material.

At higher wavelengths, > 0.95 μm, we again see a small enhancement in the quantum efficiency of the passivated cells. This indicates that back-surface passivation is also helping to raise cell performance. These data are consistent with our expectation that both front- and back-oxide passivation contributes to the increase in J_{sc}, while the majority of increase in V_{oc} comes from front-surface passivation.

3.5.4 Diffusion Length Determination from Spectral Response Data

Figure 13 shows a plot of photon attenuation length ($1/\alpha$, where α is the photon absorption coefficient) and a variable X-1, where X is
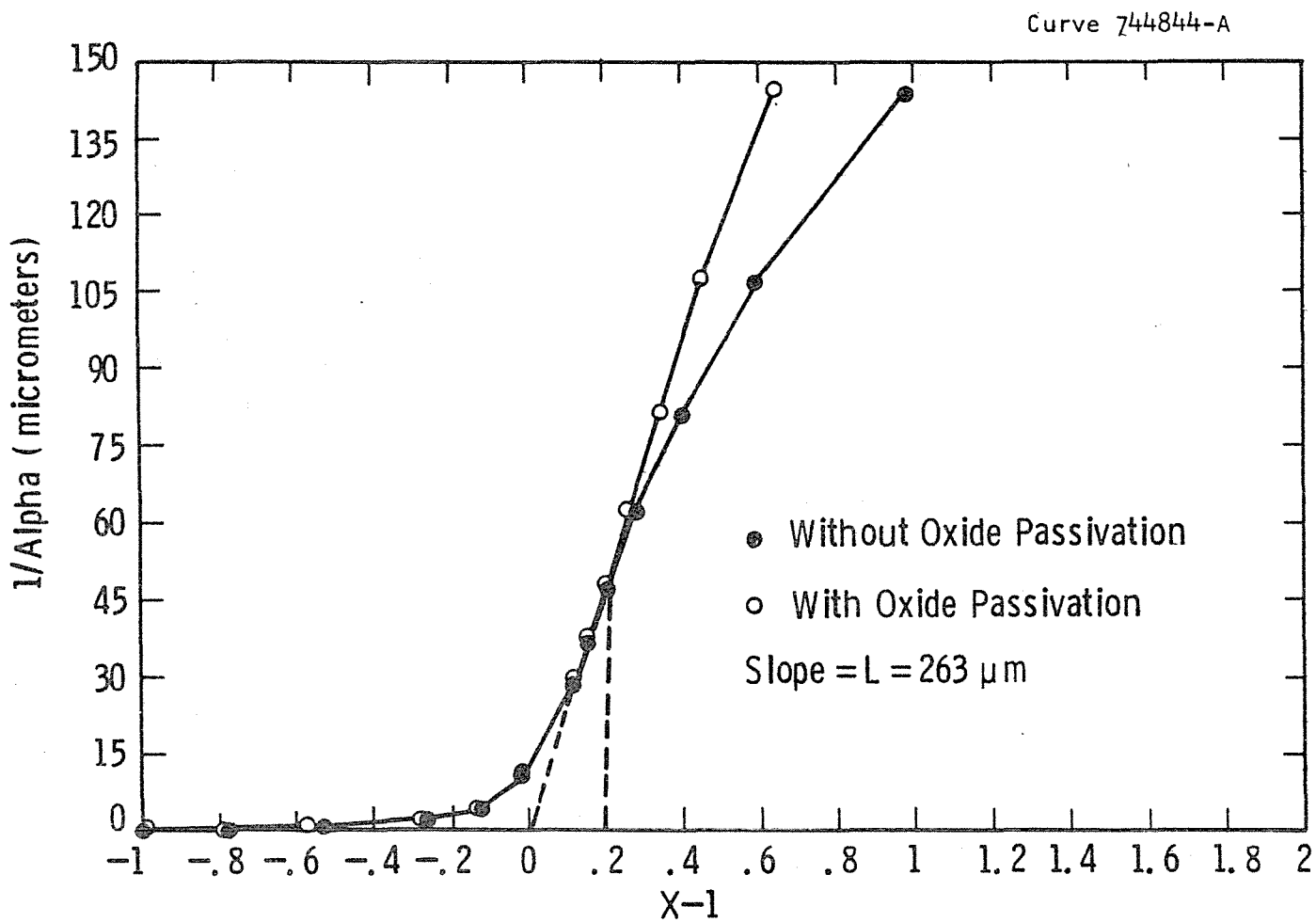
Figure 13. Diffusion length plot for an unpassivated cell and 17.2% efficient cell on 4 Ω-cm float-zone silicon.

the ratio of the number of photons absorbed per unit of time in the base to the number of electrons per unit of time in the external circuit. $X = e^{-\alpha(d + w)}/Q_E$, where d is the junction depth, w is the width of the depletion region at zero bias, and Q_E is the quantum efficiency. The slope of $1/\alpha$ versus $X-1$ gives an effective diffusion length[28] which would be equal to the base diffusion length if the base width is much greater than the diffusion length; otherwise the effective diffusion length is a combination of bulk diffusion length and surface recombination velocity.

Figure 13 shows such plots for an oxide-passivated 17.2% efficient cell and a 15.2% efficient unpassivated cell. It is interesting to note that the two curves overlap in the $1/\alpha$ range of 4.4–6.0 μm (wavelength range 0.7–0.94 μm). The slope of the two curves in this range gives a bulk diffusion length of 263 μm, but as we go to longer wavelengths the slope of the unpassivated cell becomes less steep, indicating that the effective bulk diffusion length becomes smaller due to back-surface recombination. Relative to the unpassivated cell, the slope of the oxide-passivated cell is only very slightly affected at the larger wavelengths, supporting the reduction in the back-surface recombination velocity.

Assuming 263 μm to be the true bulk diffusion length in the finished cell, we obtain a minority-carrier diffusion velocity (D/L) of 1254 cm/sec for the bulk. Only a very slight drop in the effective diffusion length at longer wavelengths (Figure 13) in the oxide-passivated cell confirms that back-surface recombination velocity has been reduced considerably. However, a downward bending suggests that S at the p-p$^+$ interface is still greater than 1254 cm/sec (D/L). If the back surface has no influence at all (infinite bulk), then there will be no curvature in Figure 13 at longer wavelengths (higher values of $1/\alpha$).

3.5.5 Spreading Resistance Measurements on 17.2% Efficient Cells

Figure 14 shows the carrier concentration profile obtained by the spreading resistance measurements. The data indicate a surface
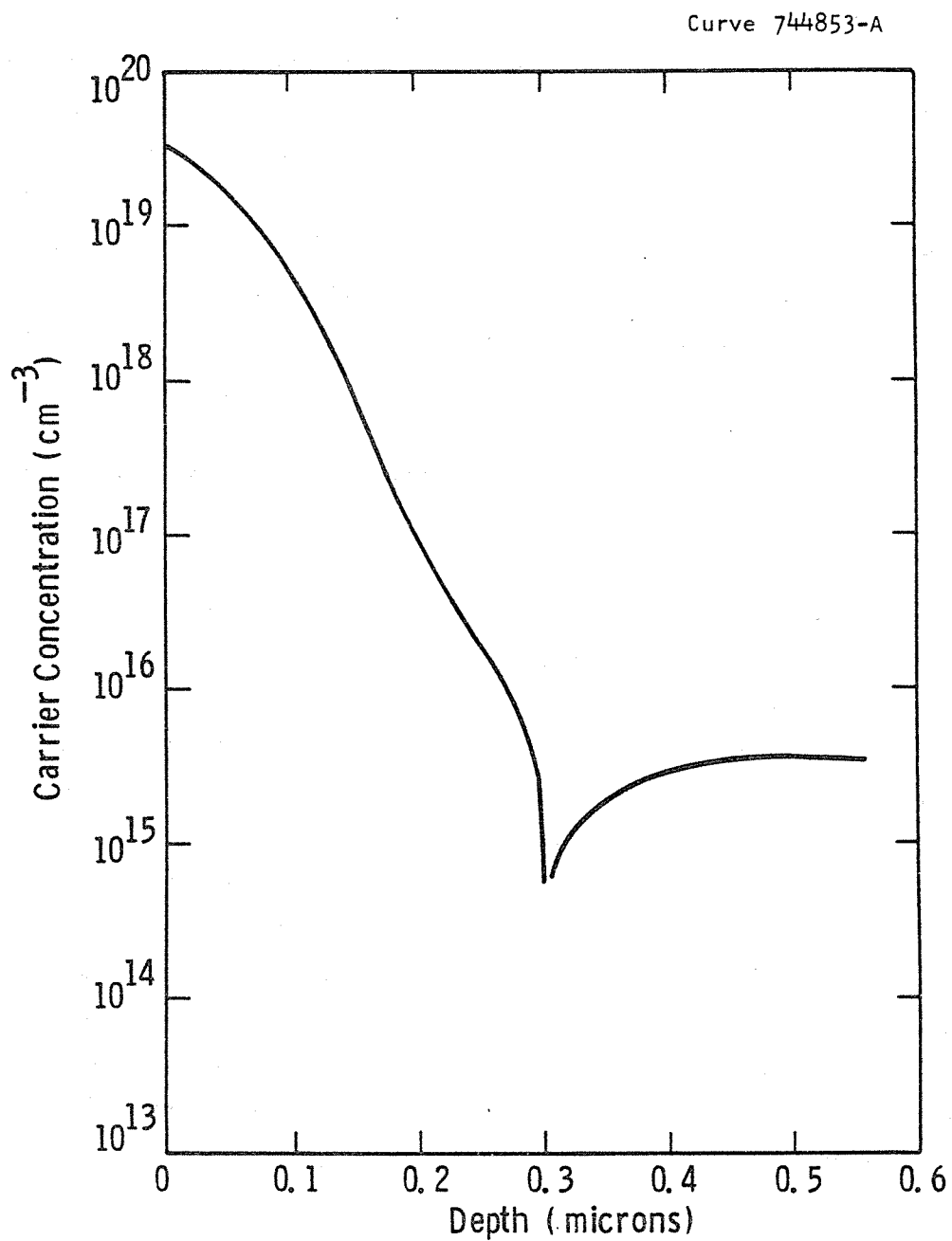
Figure 14. Dopant profile in the emitter of a 17.2% efficient oxide-passivated cell on 4 Ω-cm float-zone silicon.

concentration of 4×10^{19} cm^{-3} and a junction depth of ~ 0.3 μm. The sheet resistance measured by four-point probe after diffusion was ~ 80 Ω/square, but the sheet resistance calculated from the spreading resistance data was ~ 240 Ω/square. More measurements are required to resolve this discrepancy. The surface concentration in Figure 14 indeed appears lower than expected despite the fact that oxidation consumes 50 Å of the silicon surface. On the other hand, n-type dopants tend to segregate in the silicon at the Si/SiO$_2$ interface. A lower doping concentration does reduce heavy doping effects; however, the sheet resistance of the cell cannot be very high because the measured series resistance is only ~ 0.25 ohms.

3.5.6 Effectiveness of Front- and Back-Surface Passivation in the Oxide-Passivated Cells

In Section 3.5.2 we showed that oxide passivation reduces the reverse saturation current J_o, where $J_o = J_{oe}$ (emitter) + J_{ob} (base). In order to find out which component of J_o has been reduced most or which surface passivation is more effective in improving V_{oc}, we removed the back metal and the back oxide, protecting the front-surface, and then remetallized the back. These cells now have only front oxide passivation. Table 9 shows the cell data with a) both surfaces passivated, b) the same cells with only front oxide passivation, and c) baseline n$^+$-p-p$^+$ cells with no surface passivation.

The data in Table 9 indicate that the back oxide removal results in about 0.5 mA/cm^2 loss in J_{sc}, ~ 5 mV loss in V_{oc}, and about 0.5 to 0.75% decrease in absolute cell efficiency. Compared to the unpassivated n$^+$-p-p$^+$ cells, V_{oc} of the front-surface-passivated cell is 10 to 15 mV higher and J_{sc} is also somewhat higher, resulting in about 1% higher absolute cell efficiency. This implies that emitter surface recombination velocity controls the reverse saturation current or V_{oc} ($J_o \sim J_{oe}$) in the cells without any surface passivation and the front-surface passivation lowers J_{oe} and improves V_{oc}. It appears that with the front-surface passivation, J_o tends to become base controlled and

Table 9. Solar Cell Data With a) Both Surfaces Passivated,
b) Only Front-Surface Passivation, and c) with No
Surface Passivation

Cell ID	V_{oc} volts	J_{sc} mA/cm^2	FF	η %
(a) Both Surfaces Passivated				
1	.599	34.6	.792	16.5
2	.598	34.6	.789	16.4
3	.595	34.6	.793	16.3
4	.593	34.8	.795	16.4
5	.592	34.5	.792	16.2
6	.594	34.8	.793	16.4
7	.593	34.3	.792	16.1
8	.589	34.6	.796	16.2
(b) Above Cells with Only Front-Surface Passivation				
1	.595	33.9	.795	16.0
2	.594	34.0	.793	16.0
3	.592	33.8	.795	15.9
4	.584	34.0	.788	15.7
5	.583	33.8	.787	15.5
6	.590	34.2	.793	15.9
7	.589	33.7	.793	15.7
8	.571	33.9	.779	15.1
(c) n^+-p-p$^+$ Cells Without Surface Passivation				
1	.582	33.5	.767	14.9
2	.582	33.3	.767	14.8
3	.582	33.2	.781	15.1
4	.579	33.0	.780	14.9
5	.577	33.6	.763	15.0

therefore back-surface passivation gives an additional 5 mV improvement in V_{oc} (back oxide removal showed a 0.5 mV drop in V_{oc}). Passivating both surfaces reduces the loss of minority carriers to surfaces; therefore, we observe some increase in J_{sc} just by front-surface passivation and a further increase when both surfaces are passivated.

3.5.7 Analytical Summary of 17.2% Efficient Cells

Table 7 shows that oxide passivation coupled with careful cell processing can give solar cell efficiencies greater than 17% (AM1) on good quality 4 Ω-cm float-zone silicon, with $V_{oc} \geqslant 600$ mV, $J_{sc} \sim 36$ mA/cm^2, and fill factor ~ 0.795. These parameters are in good agreement with the model calculations in Section 3.1. These cells are among the best cells reported to date, especially on 4 Ω-cm material. The data in Table 8 show ~ 20 mV improvement in V_{oc}, ~ 3 mA/cm^2 increase in J_{sc}, and about 2% (absolute) increase in cell efficiency in the oxide-passivated cell compared to the counterpart unpassivated cell.

Dark I-V measurements (Table 8) indicate a decrease in reverse saturation current, J_o, from 3.7×10^{-12} cm^{-2} to 2.0×10^{-12} cm^{-2}. Using the expression $V_{oc} \simeq KT/q \, \ln(J_{sc}/J_o)$, this decrease in J_o coupled with the measured increase in J_{sc} essentially accounts for the observed 18 mV increase in V_{oc} due to passivation in this pair of cells. Since $J_o = J_{oe}$ (emitter) $+ J_{ob}$ (base), to find out which component of J_o has been reduced, back-oxide passivation from some lower efficiency cells (16.5%) was removed and then they were retested (Table 9b) after remetallizing the p$^+$ back surface. The data in Table 9 indicate that, out of the ~18 mV increase in V_{oc} due to oxide passivation, a 13 mV improvement comes from the front-surface passivation and the remaining comes from the back-surface passivation. This also implies that without any surface passivation in these cells, $J_o \sim J_{oe}$ and, therefore, front-surface passivation alone is able to increase V_{oc}. If J_{ob} was limiting J_o, then the front-surface passivation would not have much influence on J_o or V_{oc}. It appears that after front-surface passivation in these 4 Ω-cm cells, J_o becomes base limited ($J_o \sim J_{ob}$) and, therefore, back-

surface passivation gives an additional 5 mV improvement in V_{oc} (Tables 9a-9b). These observations are entirely consistent with our model predictions in Section 3.1, Figure 1.

Greater improvements in V_{oc} can be achieved from front-surface passivation in lower resistivity base material[22,29] with similar diffusion velocity (D/L). In these cells J_{ob} will no longer limit J_o; instead, the value of S achievable from front-surface passivation will define the lower limit of J_{oe} or J_o. However, if J_{oe} remains much greater than J_{ob}, even after front-surface passivation, then the back-surface passivation will not increase V_{oc} much further. Some attempts are being made to verify this by fabricating cells on 0.2-0.3 Ω-cm material specially grown for high lifetime.

Figure 12 explains the reason for the observed increase in J_{sc} due to oxide passivation. Shorter wavelengths (< 0.55 µm) are primarily absorbed in the emitter, while longer wavelengths (> 0.95 µm) are mostly absorbed near the back surface. The figure shows that front-surface passivation results in a significant improvement in the quantum efficiency at shorter wavelengths, while the back-surface passivation increases the quantum efficiency at longer wavelengths. This is consistent with the data in Table 9, which show that both front- and back-surface passivation contribute to the observed increase in J_{sc}, since passivation reduces the number of photogenerated carriers that are lost to the surfaces. The quantum efficiency at ~ 0.4 µm wavelength could be raised from 40 to 75% by emitter surface passivation, which implies that in the unpassivated cell, a majority of the photogenerated carriers near the emitter surface are not collected because of high surface recombination, and not because of high bulk recombination in the emitter as a result of Auger and bandgap narrowing effects. Thus, the emitter region should not be regarded as a "dead layer" because simply by proper oxide passivation, emitter quantum efficiency can be made greater than 75%, and further improvements may be possible by reducing Auger recombination and bandgap narrowing effects in the emitter. Surface recombination can be minimized further by growing a thin tunnel

oxide underneath the front and back metal to completely avoid direct metal/silicon contact.

Figure 12 indicates that quantum efficiency in the wavelength range of 0.85–0.95 μm is nearly the same for both unpassivated and passivated cells. Most of the light in this wavelength range is absorbed within the bulk silicon, away from the surfaces, since the absorption length is in the range of 20–60 μm. This suggests that oxide passivation has apparently not changed the actual diffusion length of the base material, which is calculated to be 263 μm in this wavelength range (Figure 13). At longer wavelengths (higher values of $1/\alpha$), the slope of the unpassivated cell becomes less steep relative to a passivated cell, indicating that its effective diffusion length decreases near the back surface due to high surface recombination velocity. The slope of the curve for the oxide-passivated cell in Figure 13 is only slightly affected at longer wavelengths, supporting the notion that a good back-surface passivation has been achieved.

3.6 Oxide Passivated Solar Cells Fabricated on 0.1–0.2 Ω-cm Boron-Doped Float-Zone Silicon

A few solar cells have been fabricated on 0.1–0.2 Ω-cm Wacker Waso-S (100), boron-doped float-zone silicon. The thickness of these wafers was ~ 350 μm. In this particular run the antireflective coating ended up a little thin and patchy on the oxide-passivated cells because of some problem in the photoresist step; however, solar cell efficiencies still look quite promising. Table 10 shows the solar cell data on 0.1–0.2 Ω-cm material, with and without passivation. Without passivation, 0.1–0.2 Ω-cm material gave $J_{sc} \simeq 31.8$, $V_{oc} \simeq 0.613$, fill factor $\simeq .802$, and cell efficiency = 15.6%. After oxide passivation, the best cell in this run had $J_{sc} \sim 33.0$, $V_{oc} \sim 0.627$, fill factor $\sim .815$, and cell efficiency ~ 16.9%. Partly because of poor AR coating, we only saw about 1.5 mA/cm^2 improvement in the J_{sc} and about 14 mV improvement in V_{oc} due to oxide passivation.

50

Table 10. Solar Cell Data on 0.1–0.2 Ω-cm Float-Zone Silicon, With and Without Oxide Passivation

Cell ID	J_{sc} mA/cm^2	V_{oc} volts	FF %	η %
(a) Without Oxide Passivation				
C-1	31.2	.612	.785	15.0
-2	31.8	.613	.802	15.6
-4	31.3	.612	.798	15.3
-5	31.7	.612	.797	15.5
-9	30.9	.607	.799	15.0
(b) With Oxide Passivation				
C-4	33.0	.627	.815	16.9
-8	33.2	.624	.793	16.4
C3-4	32.3	.620	.809	16.3
-9	32.4	.617	.811	16.2
C4-8	32.6	.617	.800	16.1

*Cell Area 1 cm^2, AM1, 100 mW/cm^2 Illumination

Quantum efficiency data in Figure 15 show that somewhat smaller enhancement in J_{sc} is also because the back-surface passivation is not effective in increasing the long wavelength response in these cells. In Section 3.5.6 we showed that the back-surface passivation on 4 Ω-cm material gave ~ 0.5 mA/cm^2 improvement in J_{sc} and about 5 mV increase in V_{oc}. One of the reasons why back-surface passivation is not as effective is because the cell thickness to diffusion length ratio, $\frac{W}{L}$ (= $\frac{375 \ \mu m}{300 \ \mu m}$), is more than unity in these cells as opposed to a $\frac{W}{L}$ (= $\frac{250 \ \mu m}{263 \ \mu m}$) of less than unity for 4 Ω-cm cells. In low-resistivity silicon with good lifetime,

Figure 15. Quantum efficiency versus wavelength plot for an
unpassivated cell and a 16.9% efficient oxide-passivated
cell on 0.1-0.2 Ω-cm float-zone silicon.

J_{ob} is quite small and, even after front-surface passivation, if J_{oe} dominates J_o, then back-surface passivation will not affect J_o or improve V_{oc}. A diffusion length of 300 μm in these cells was obtained from the slope of $1/\alpha$ versus X-1 in the wavelength range of 0.7-0.95 μm in Figure 16. Such a high diffusion length in the finished cells on 0.1-0.2 Ω-cm material is quite respectable, and we think we could have done better on this material if the AR coating was proper. The overlap of two curves in Figure 16, especially at longer wavelengths, again supports the premise that oxide passivation on the back of these cells is not helping the current response at all.

Dark I-V data in Table 11 show a decrease in J_{o1} by a factor of ~1.4 due to oxide passivation. This is consistent with the observed increase in V_{oc}.

3.7 Oxide-Passivated Solar Cells Fabricated on 0.75 Ω-cm Boron-Doped Float-Zone Silicon

Solar cells were also fabricated on 0.75 Ω-cm Wacker Waso-S boron-doped float-zone silicon using the oxide passivation technique. Solar cell data on this material, with and without passivation, are shown in Table 12. Without the oxide passivation, this material gives J_{sc} = 32.3 mA/cm^2, V_{oc} = .607 mV, fill factor = .802, and cell efficiency of 15.7%. After oxide passivation, the best cell gave J_{sc} = 33.7, V_{oc} = 0.624, fill factor = .792, and cell efficiency of 16.7%. The scatter in the cell data was due to the nonuniform and patchy AR coating since these cells were also processed with the 0.1-0.2 Ω-cm cells described in Section 3.6. Compared to 4 Ω-cm material, we see a smaller oxide passivation-induced improvement. J_{sc} went up by 1.5 mA/cm^2 and V_{oc} improved by 17 mV. Quantum efficiency data in Figure 17 show improvement in the entire spectrum range; however, quantum efficiency improvement in the short wavelengths is not as good as seen for 4 Ω-cm material. This may be another reason, in addition to a poor AR coating, why we did not see as much improvement in J_{sc}. Slopes of the $1/\alpha$ versus X-1 plot in Figure 18 give a bulk
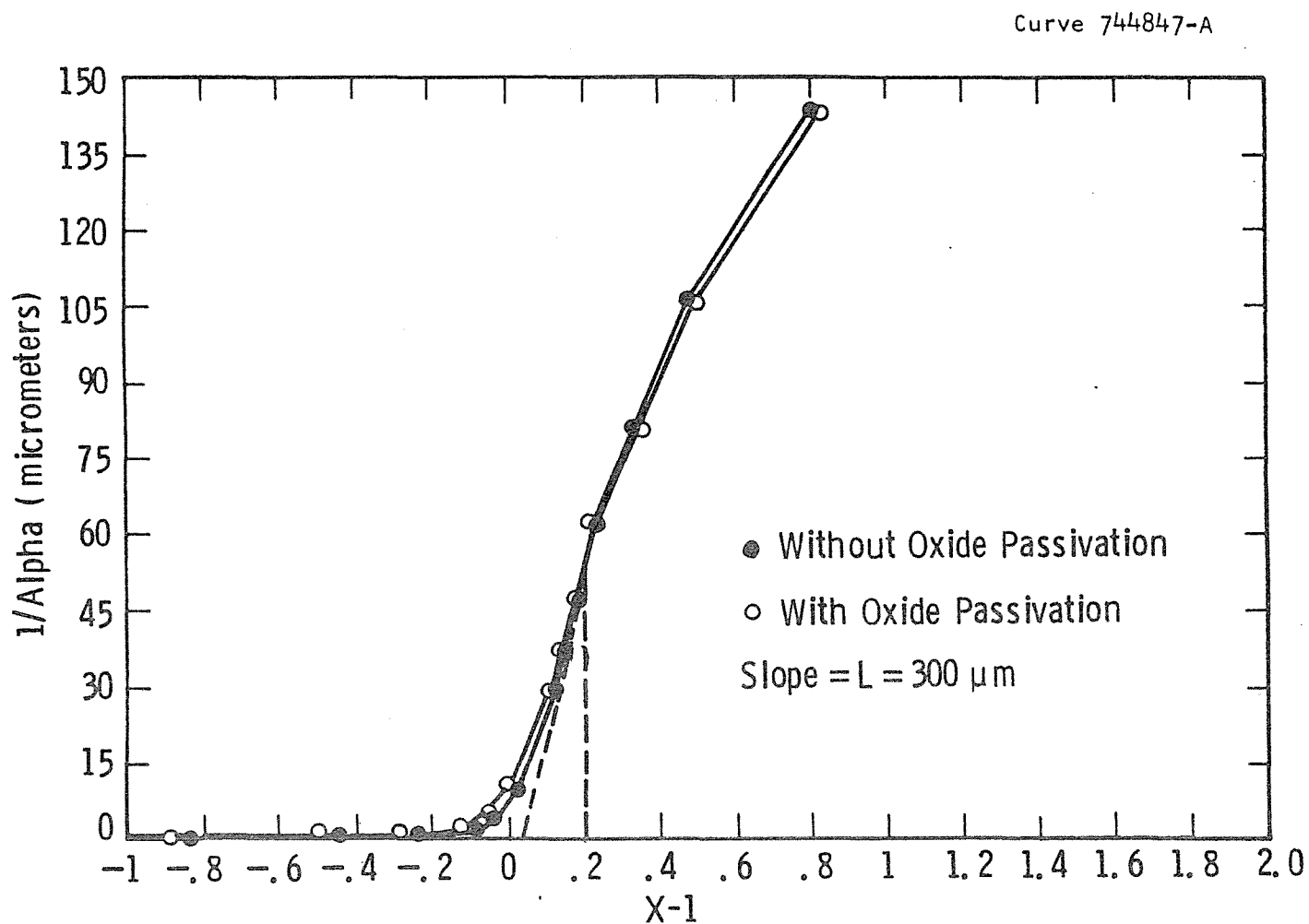
Figure 16. Diffusion length plot for an unpassivated cell and a 16.9% efficient oxide-passivated cell on 0.1-0.2 Ω-cm float-zone silicon.
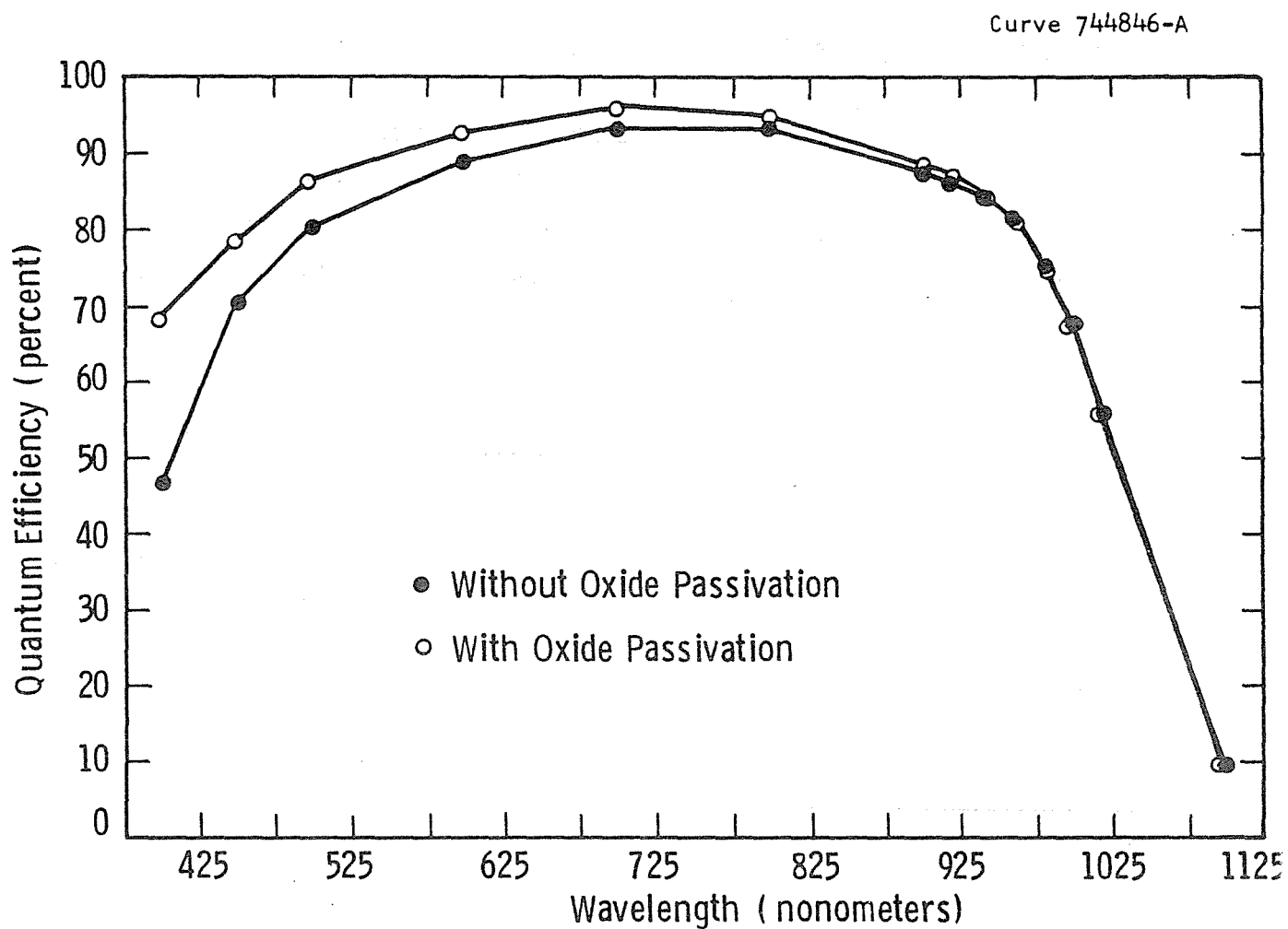
54
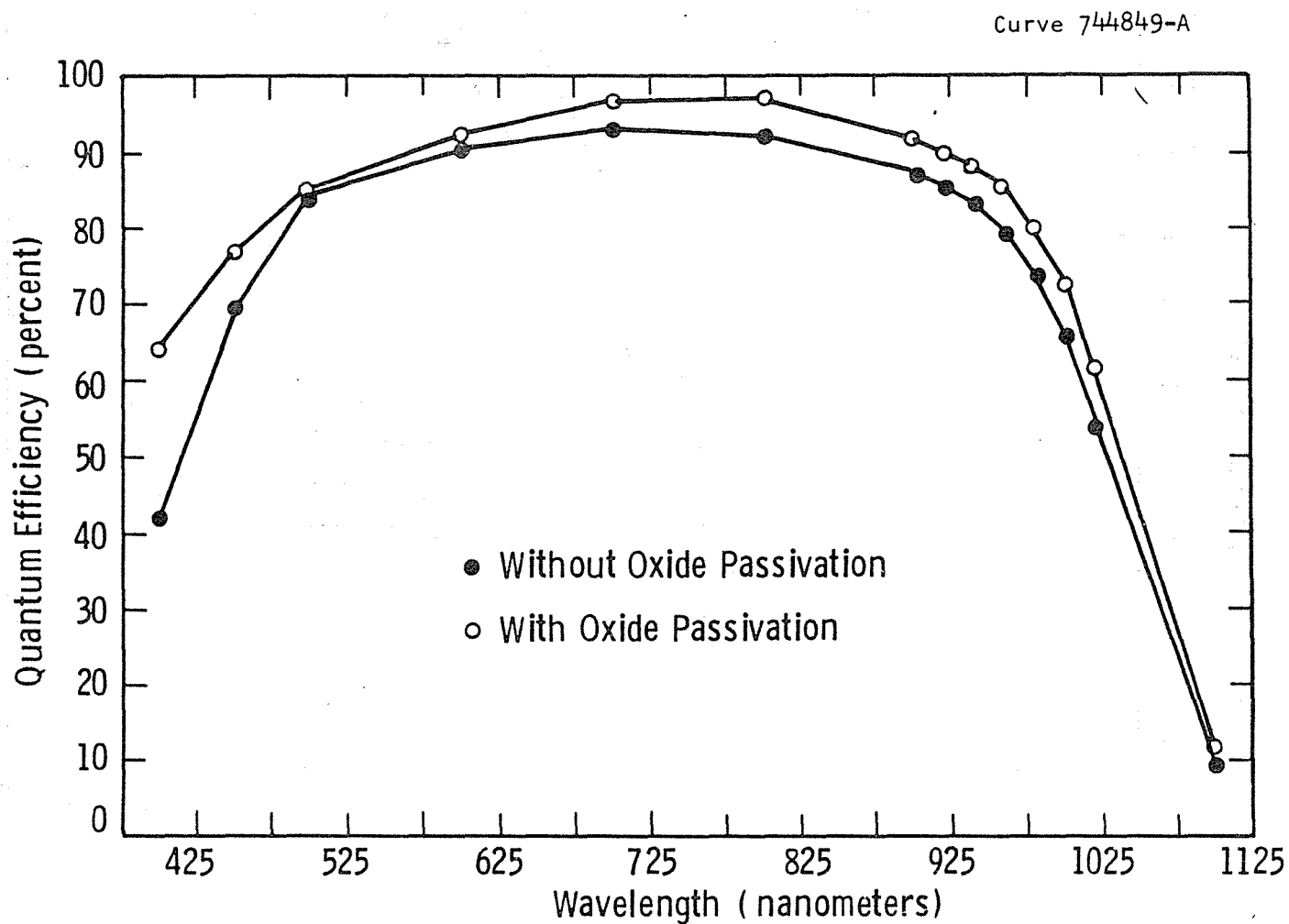
Figure 17. Quantum efficiency versus wavelength plot for an
unpassivated cell and a 16.7% efficient oxide-passivated
cell on 0.75 Ω-cm float-zone silicon.
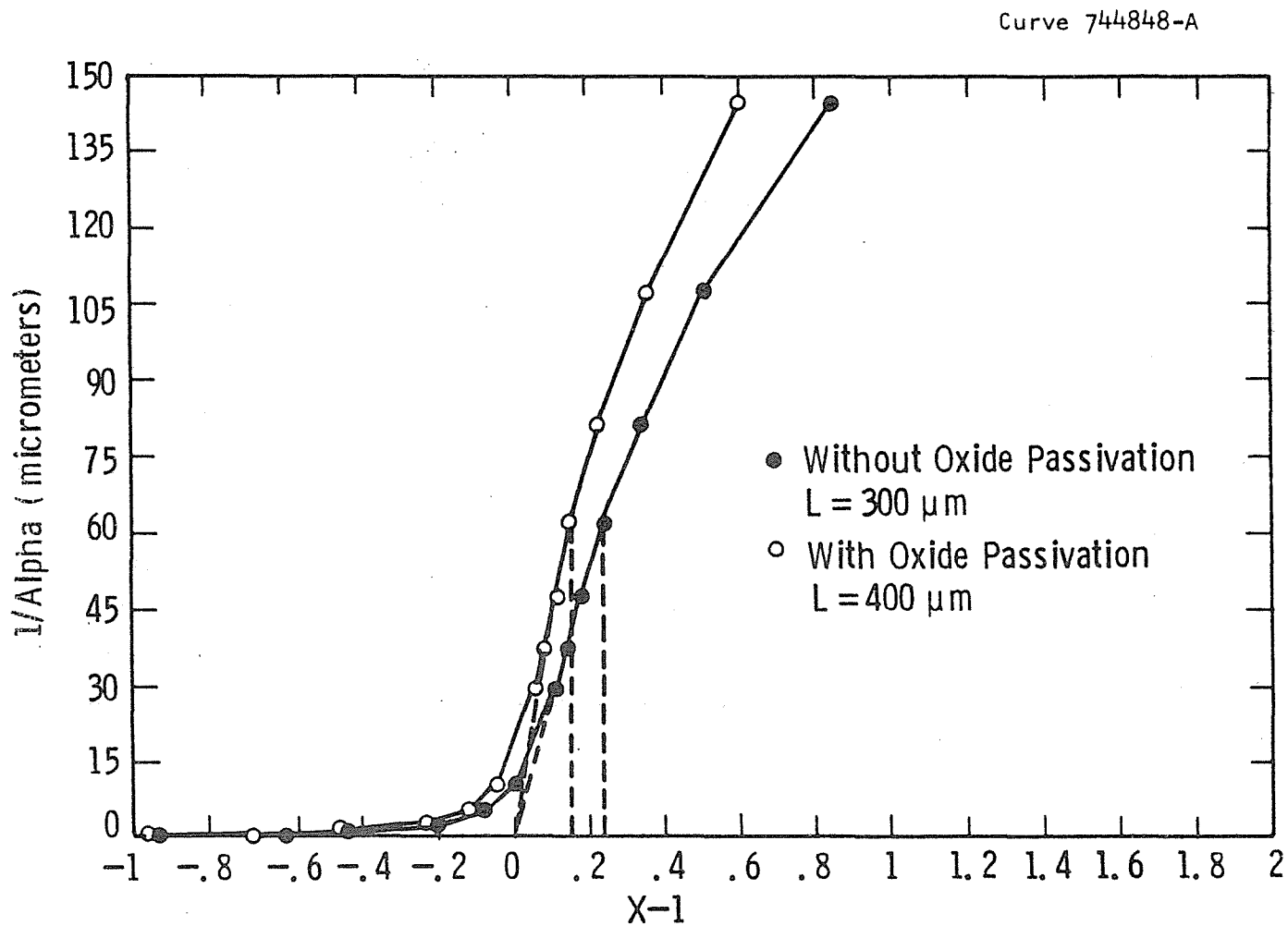
Figure 18. Diffusion length plot for an unpassivated cell and a 16.7% efficient oxide-passivated cell on 0.75 Ω-cm float zone silicon.

Table 11. A Comparison of the Cell Parameters of a Baseline
n^+-p-p^+ Cell and 16.9% Oxide-Passivated Cell
Fabricated on 0.1-0.2 Ω-cm Float-Zone Silicon

Parameter	Baseline n^+-p^+p^+ Cell	16.9% Oxide-Passivated Cell
J_{sc}	31.8 mA/cm^2	33.0 mA/cm^2
V_{oc}	.613 volts	.627 volts
FF	.802	.815
η	15.6%	16.9%
R_s	0.76 Ω-cm^2	0.26 Ω-cm^2
R_{sh}	8.3 kΩ-cm^2	35 kΩ-cm^2
J_{o1}	7.1 x 10^{-13} A/cm^2	5.0 x 10^{-13} A/cm^2
T_{eff}	0.5 μsecs	1.06 μsecs
J_{o2}	2 x 10^{-6} A/cm^2	5 x 10^{-6} A/cm^2

diffusion length of ~300 μm in the unpassivated cell and ~400 μm in the passivated cell. Curves in Figure 18 tend to diverge at longer wavelengths, indicating that the back-surface passivation is working. This is also consistent with the $\frac{W}{L} = \frac{350}{400} < 1$ for the passivated cell.

Dark and lighted I-V data in Table 13 show that J_o decreases by about a factor of 2 in the oxide-passivated cells. This decrease coupled with the observed 1.5 mA/cm^2 increase in J_{sc} accounts for the 17 mV increase in V_{oc} due to oxide passivation.

3.8 Oxide-Passivated Solar Cells on 0.3-0.7 Ω-cm Gallium-Doped Czochralski Silicon

In order to see the effect of dopant on the base material, we obtained 0.25 to 0.67 Ω-cm Ga-doped Czochralski crystal with (100) orientation. This crystal was pulled from a synthetic quartz crucible to minimize the residual impurity concentration. Table 14 shows that n^+-p-p^+ solar cells fabricated on this material gave cell efficiencies exceeding 15%. V_{oc} was greater than 600 mV and J_{sc} was ~ 31 mA/cm^2.

Table 12. Solar Cell Data on 0.75 Ω-cm Float-Zone Silicon, With and Without Oxide Passivation

Cell ID	J_{sc} mA/cm^2	V_{oc} Volts	FF %	η %
(a)	Without Oxide Passivation			
R-1	31.7	.605	.794	15.2
R-2	32.3	.607	.802	15.7
-3	32.0	.606	.800	15.5
-4	32.9	.606	.796	15.8
-5	31.9	.602	.801	15.4
-6	31.6	.605	.793	15.2
-8	31.5	.600	.801	15.1
-10	31.6	.606	.796	15.2
(b)	With Oxide Passivation			
R1-4	33.2	.612	.804	16.4
-5	33.7	.624	.792	16.7
-8	33.2	.613	.805	16.4
-9	33.4	.608	.801	16.3
R1-8	33.5	.608	.791	16.1
5	33.2	.609	.791	16.1

*Cell Area 1 cm^2, AM1, 100 mW/cm^2 Illumination

Table 14 also shows that the oxide-passivated cells on the Ga-doped wafers give efficiencies in excess of 16% with $J_{sc} \sim 33$ mA/cm^2 and V_{oc} as high as 613 mV. The oxide thickness on top of the n$^+$ region was ~ 100 Å and on top of the p$^+$ region it was ~ 40 Å. Consistent with our model calculations, 650 Å thick AR coating was spun to reduce reflection losses.

Table 13. A Comparison of the Cell Parameters of a Baseline n^+-p-p^+ Cell and 16.7% Oxide-Passivated Cell Fabricated on 0.75 Ω-cm Float-Zone Silicon

Parameter	Baseline n^+-p-p^+ Cell	16.7% Oxide-Passivated Cell
J_{sc}	32.3 mA/cm^2	33.7 mA/cm^2
V_{oc}	.607 volts	.624 volts
FF	.802	.792
η	15.7%	16.7%
R_s	0.9 Ω-cm^2	.46 Ω-cm^2
R_{sh}	1.6 MΩ-cm^2	53 kΩ-cm^2
J_{o1}	1.8×10^{-12}	9.4×10^{-13}
T_{eff}	19 μsecs	67 μsecs
J_{o2}	1.3×10^{-6}	1.1×10^{-6}

Table 14. Baseline n^+-p-p^+ Cells and Oxide-Passivated O-n^+-p-p^+-O Solar Cells on 0.3 to 0.7 Ω-cm Gallium-Doped Czochralski Crystal Grown From a Synthetic Quartz Crucible

Cell ID	J_{sc} (mA/cm^2)	V_{oc} (volts)	FF	η %
a) Baseline n^+-p-p^+ Cells (HIEFY-7)				
1	31.2	.603	.798	15.1
2	31.3	.603	.798	15.1
3	31.2	.602	.797	15.0
4	31.2	.603	.784	14.7
b) Oxide-Passivated O-n^+-p-p^+-O Cells (HIEFY-5)				
1	33.6	.608	.794	16.3
2	33.5	.608	.795	16.2
3	32.8	.613	.802	16.2
4	32.9	.612	.800	16.2

*Cell Area 1 cm^2, AM1 100 mW/cm^2 illumination

3.9 Gallium-Diffused Back-Surface Field

Our model calculations (Figure 19) show that surface recombination velocity (S_e) can be minimized at the $p-p^+$ interface by an abrupt back-surface field with a doping concentration of $\sim 5 \times 10^{18}$ cm^{-3}. Model calculations in Figure 20 indicate that the width of the back-surface field region should be greater than 10 µm for a cell design which consists of metal on top of the p^+ region ($S_o \sim 10^6$ cm/sec). However, if the p^+ surface is passivated ($S \sim 500$ cm/sec), then the width of the p^+ region should be reduced below 1 to 2 µm.

Gallium fits the silicon lattice better than boron and may therefore show lower bandgap-narrowing effects. Therefore, we decided to minimize heavy doping effects in the BSF region without losing its effectiveness by forming a Ga back-surface field with a surface concentration of $\sim 5 \times 10^{18}$ cm^{-3} and $W_p+ < 2$ µm. We used an open-tube gallium (OTG) diffusion process for this step.

The open-tube gallium (OTG) diffusion process uses carbon monoxide to reduce gallium oxide, Ga_2O_3, at controlled temperature to generate gaseous gallium, which diffuses into the silicon wafer. The process equipment consists of three main parts: the diffusion furnace, the source furnace, and the gas-control system. This process can achieve three functions: the predeposition oxidation, the gallium deposition, and the drive-in diffusion with oxidation.

3.9.1 Chemistry of the OTG Process

Chemical reactions involved in the OTG deposition process can be simplified as follows:

$$Ga_2O_3 \ (s) + 2 \ CO \ (g) \rightarrow Ga_2O \ (g) + 2 \ CO_2 \ (g) \tag{15}$$

$$Ga_2O \ (s) + \ CO \ (g) \rightarrow 2 \ Ga \ (g) + \ CO_2 \ (g) \tag{16}$$

$$Ga_2O_3 \ (s) + \ CO \ (g) \rightarrow 2 \ GaO \ (g) + \ CO_2 \ (g) \tag{17}$$

$$Ga_2O_3 \ (s) + 3 \ CO \ (g) \rightarrow 2 \ Ga \ (g) + 3 \ CO_2 \ (g) \tag{18}$$
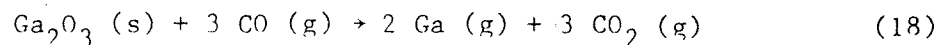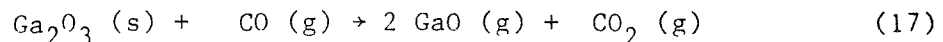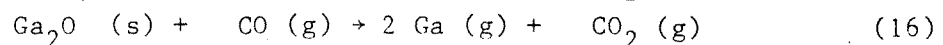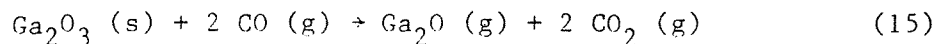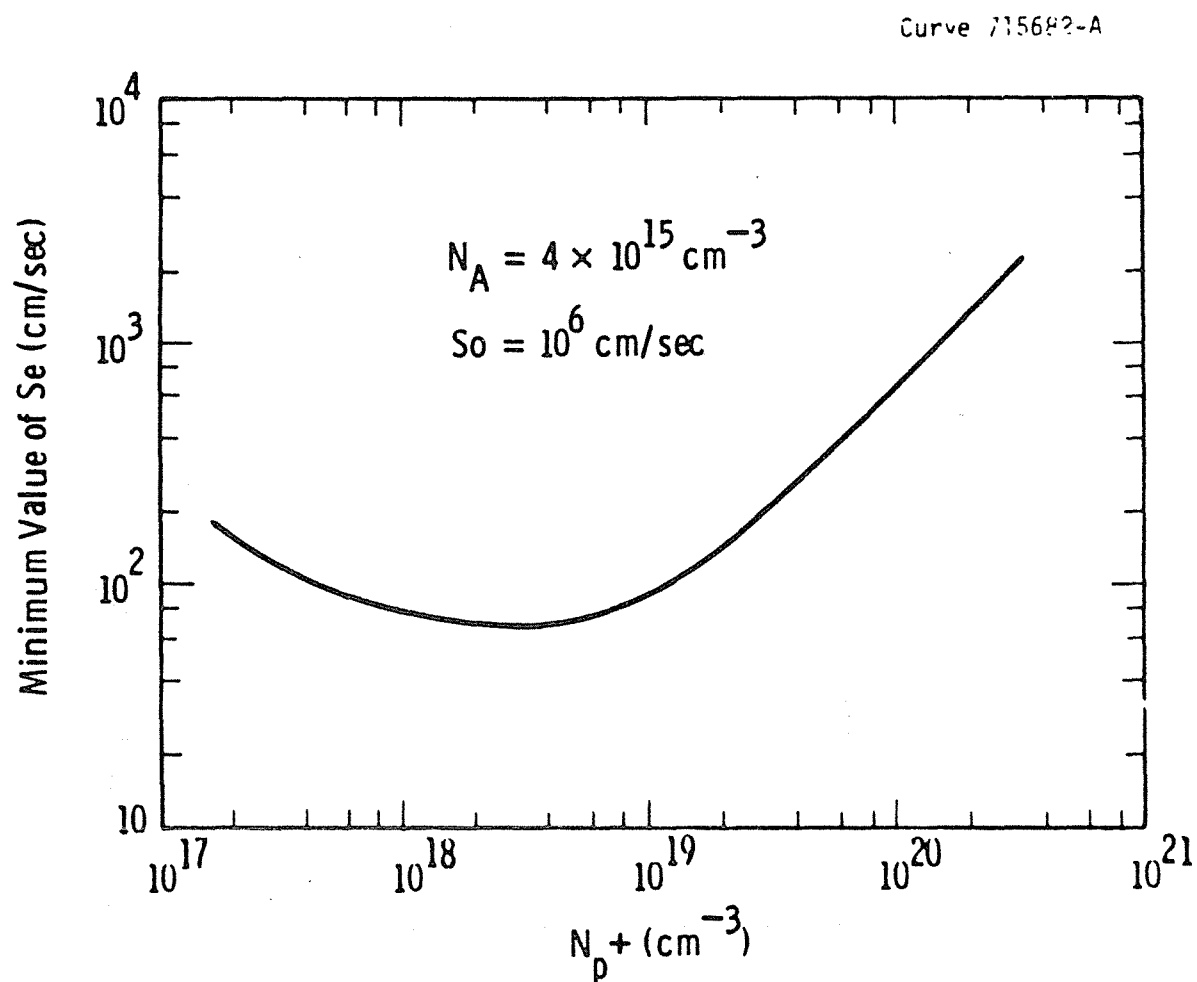
Figure 19. Effect of abrupt doping concentration in the p^+ region on the minimum effective recombination velocity at the p-p^+ interface. W_p^+ was optimized at each concentration.
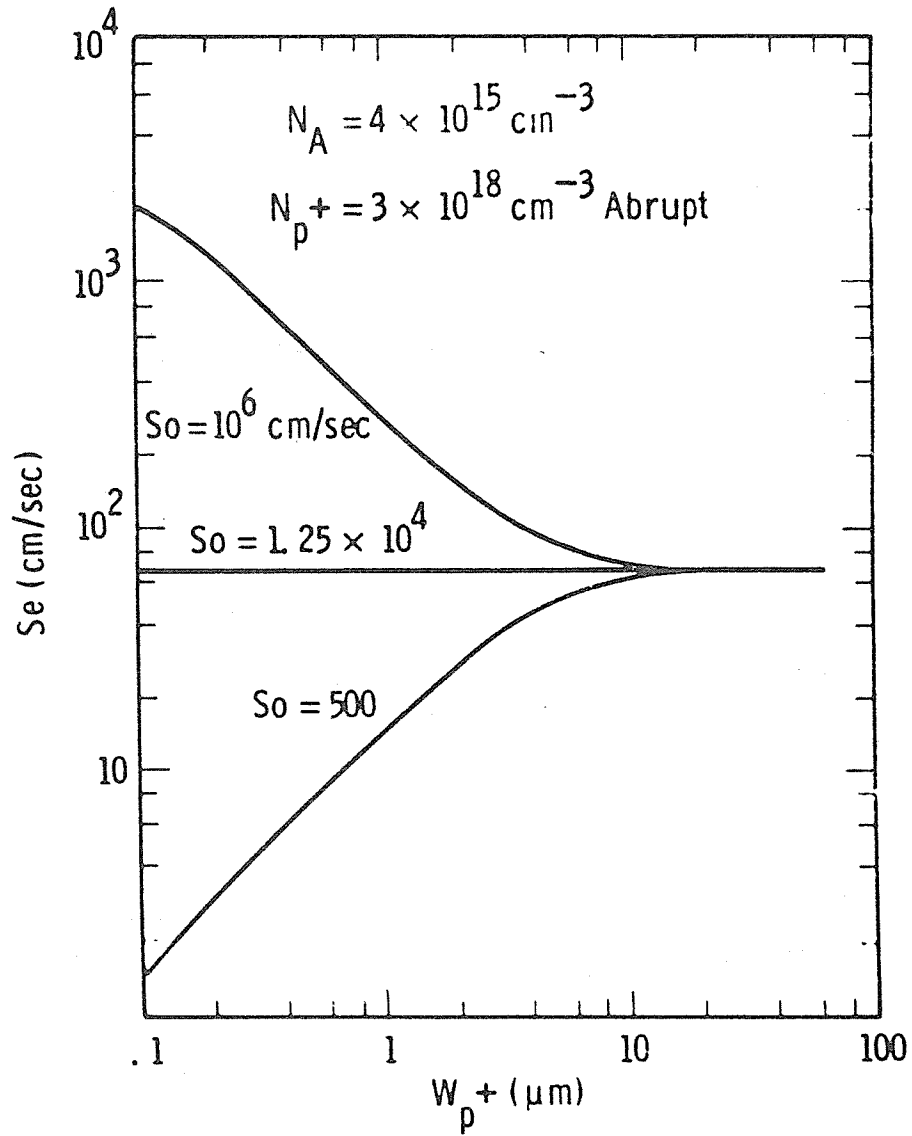
Figure 20. Effect of surface recombination velocity, S_o, and width of p^+ region (W_p+) on the effective recombination velocity at $p-p^+$ interface.

where (s) and (g) represent solid phase and gas phase, respectively. It is known that the concentration of GaO in Equation 17 is negligible. Hence, the chemical reactions in the system may be further simplifed as

$$Ga_2O_3 \text{ (s)} + 3 \text{ CO (g)} \rightarrow 2 \text{ Ga (g)} + 3 \text{ CO}_2 \text{ (g)} \qquad (19)$$
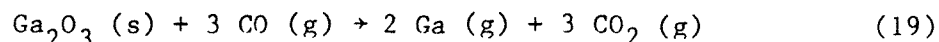
Therefore, at a controlled carbon monoxide gas flow rate and controlled gallium oxide source temperature, e.g., $875^{\circ}C \pm 2 \,^{\circ}C$, a finite amount of gaseous gallium can be generated. Using an inert gas such as argon can bring the gallium into the diffusion furnace and diffuse the gallium impurity uniformly into the silicon wafers.

The chemistry of pyrogenic oxidation is the same as conventional wet oxidation, the details of which are not included here.

3.9.2 The OTG Diffusion System

The following simplified diagram (Figure 21) shows the OTG diffusion system. Gallium trioxide, Ga_2O_3, as shown is the diffusion source reagent. The source furnace and diffusion furnace temperatures are set at $T_s = 875^{\circ}C \pm 2^{\circ}C$ and $T_D = 1230^{\circ}C + 1^{\circ}C$, respectively.
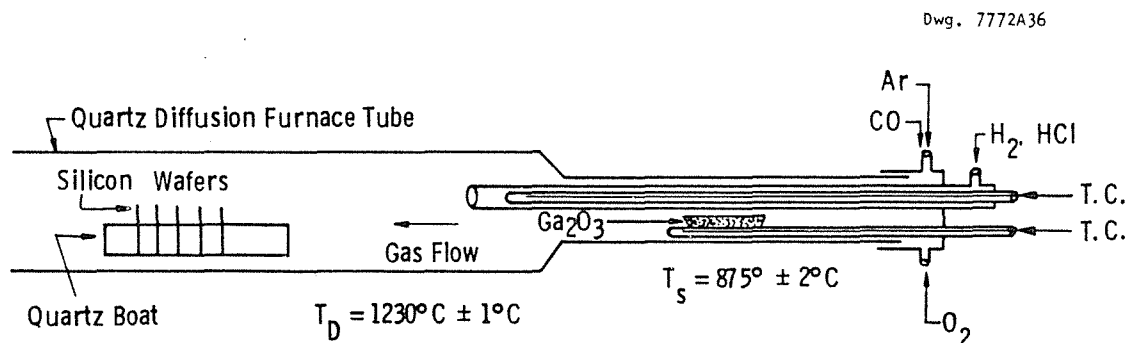
Figure 21. Arrangement for open-tube gallium diffusion.

Silicon wafers sit in the diffusion flat zone, which has a temperature controlled to within an accuracy of $\pm 1^{\circ}C$. The timer controls various gases and turn-on and turn-off at a pre-set time sequence.

3.9.3 Process Sequence Used for Open-Tube Gallium Diffusion for Back-Surface Field Formation

    a.   Mask front surface by 1200 Å Silox + 1200 Å silicon nitride deposited by CVD technique to prevent Ga diffusion into the front surface.

    b.   Load wafers at $600^{\circ}C$ with 2 liter/min Argon flow in the tube.

    c.   Heat wafers from $600^{\circ}C$ to $1230^{\circ}C$ in 45 minutes.

    d.   Turn on 900 cc/min CO for 3 minutes.

    e.   Slow cool wafers from $1230^{\circ}C$ to $900^{\circ}C$ at a rate of $1.5^{\circ}C$/min.

    f.   At $900^{\circ}C$ stop the flow of CO.

    g.   Slow pull the wafers from the furnace in 30 minutes.

Figure 22 shows that the above process sequence gave a back-surface concentration of $\sim 5 \times 10^{18}$ cm^{-3} and a p^+ depth of ~ 2 microns. However, on the front surface (Figure 8) we observed an out-diffusion of boron probably into the oxide because p-type dopants tend to segregate into the oxide. Since the boron concentration decreased substantially in the first 5 to 10 micron region, we chem-mechanically polished a ~ 25 µm thick region from the top surface prior to $POCl_3$ emitter diffusion.

3.9.4 n^+-p-p^+ Solar Cells with Ga Back-Surface Field

We have fabricated baseline n^+-p-p^+ cells with a Ga back-surface field, and the oxide-passivated cells with Ga BSF are in process. Cell data in Table 15 indicate that, despite the desired surface concentration, we observed 2 to 3 mA/cm^2 reduction in J_{sc}, a decrease of
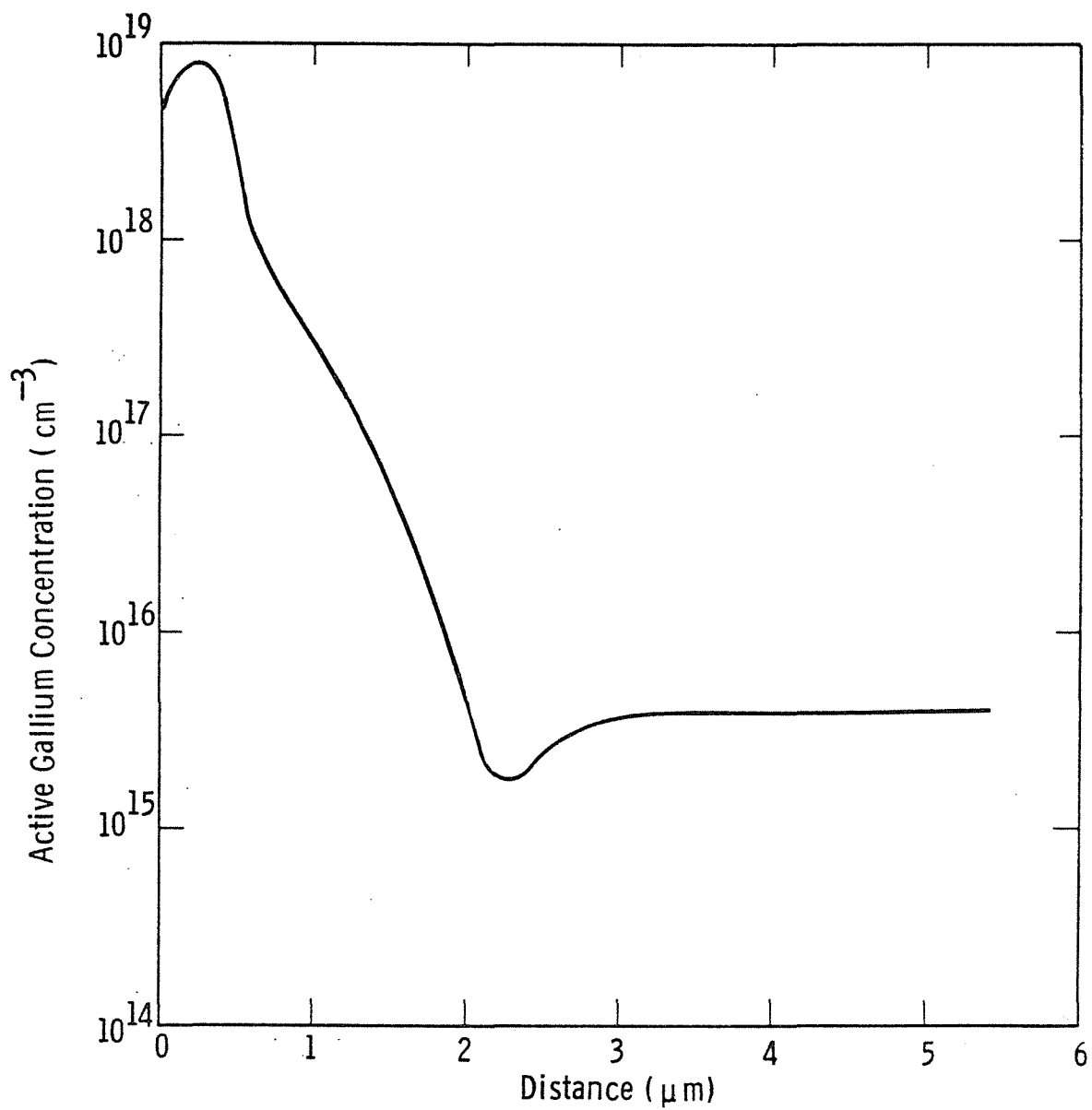
Figure 22.   Gallium back-surface field profile after 1230°C open-tube gallium diffusion.

Table 15. A Comparison of n^+-p-p^+ Solar Cells with Diffused Boron Back-Surface Field at $950^\circ C$ ($N_{surface} \sim 10^{20}$ cm^{-3}, $W_{p^+} \sim 0.5$ μm) and Gallium Back-Surface Field Formed by Open-Tube Ga Diffusion at $1230^\circ C$ ($N_{surface} \sim 5 \times 10^{18}$ cm^{-3}, $W_{p^+} \sim 2$ μm)

Cell ID	J_{sc} (mA/cm^{-2})	V_{oc} (volts)	FF	η %
a) Boron Back-Surface Field (M-7)				
1	33.5	.582	.767	14.9
2	33.3	.582	.767	14.8
3	33.1	.584	.756	14.6
4	33.2	.582	.781	15.1
b) Gallium Back-Surface Field (HIEFY)				
1	29.5	.552	.773	12.6
2	30.0	.555	.777	12.9
3	30.5	.557	.783	13.3
4	30.4	.556	.778	13.2

*Cell area 1 cm^2, AM1 100 mW/cm^2 Illumination

~ 0.25 mV in V_{oc}, and about 2% loss in cell efficiency compared to the boron-diffused back-surface field which has a surface concentration of ~ 10^{20} cm^{-3}. Dark I-V analysis showed a decrease in the effective bulk lifetime from 276 μsecs ($J_{ol} \sim 3.3 \times 10^{-12}$ A/cm^2) to 38 μsecs ($J_{ol} \sim 8.9 \times 10^{-12}$ A/cm^2) by switching from boron BSF to gallium BSF. The high-temperature ($1230^\circ C$) diffusion during this OTG process appears to degrade the bulk lifetime. It is possible that a slower cooling rate may be required since the cleanliness of the OTG process is sacrificed at such high temperatures. Possibly, this disadvantage can be overcome by incorporating HCl gettering and very slow cooling (Figure 21).
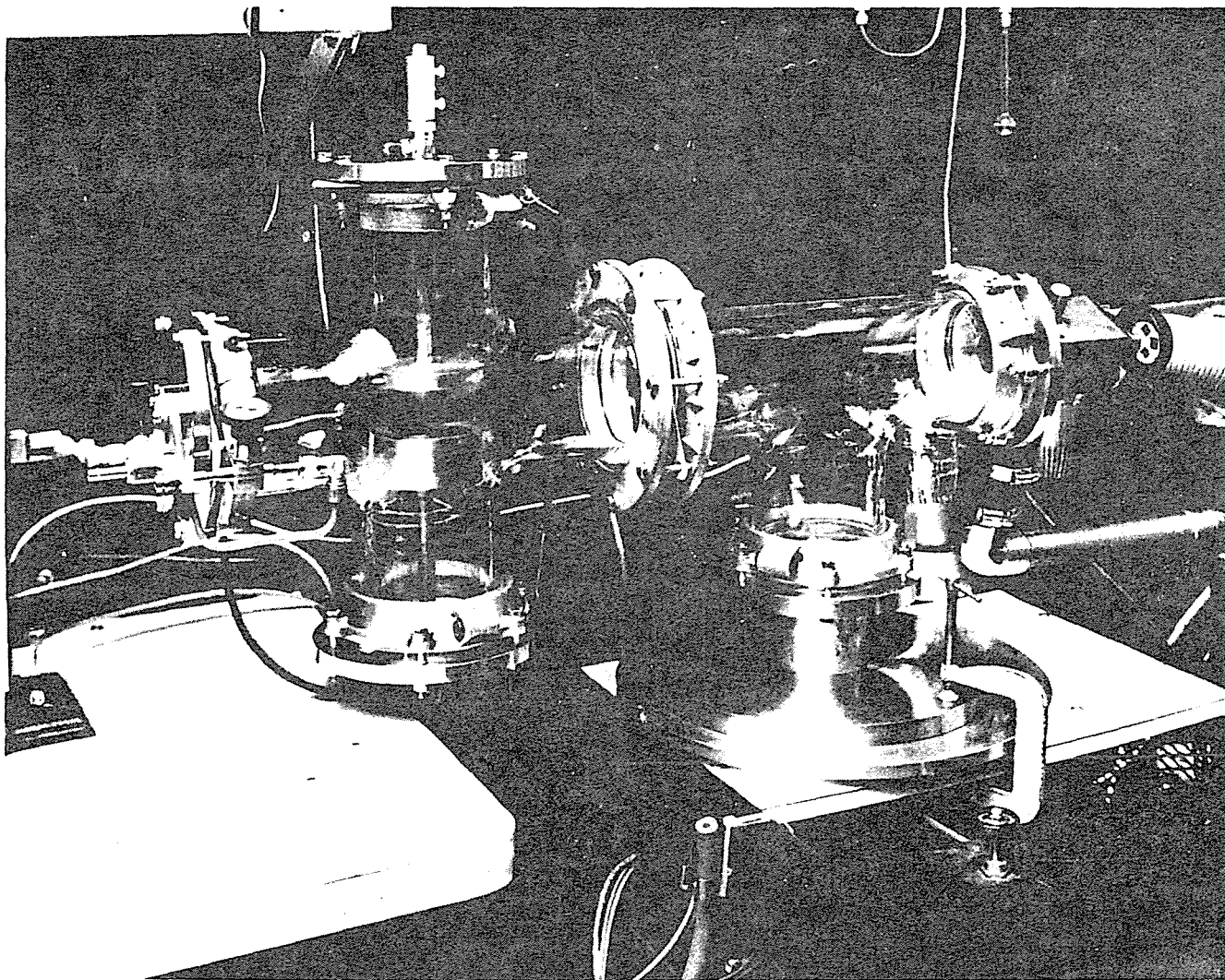
Figure 23.   Research deposition reactor.

It should be recognized that a BSF width of 2 μm with $N_A \sim 5 \times 10^{18}$ is not appropriate for a n^+-p-p^+ cell design but is desirable for the oxide-passivated cells (Figure 20). A few oxide-passivated cells with Ga BSF were also processed; however, due to loss in carrier lifetime we did not see high efficiencies.

3.10 Plasma-Deposited Thin Films for Multilayer Antireflective Coating

Our model calculations (Figure 3) indicate that reflection losses can be reduced significantly by a properly tailored multilayer AR coating instead of the conventionally used single- or double-layer coatings. Plasma techniques can provide a way of depositing AR-coated layers with controlled thickness and refractive index; therefore, we are developing and investigating this approach. Generally, hard and chemically stable thin films of refractory materials such as SiO_2, Si_3N_4, SiC, and TiO_2 can be deposited with high optical perfection by plasma deposition techniques. The deposition reaction is carried out in a glow discharge at pressures of about 1 torr. The "hot" electrons of plasma-producing radicals combine on the substrate under ion bombardment to form the films. An illustration of our research deposition reactor is shown in Figure 23.

The films can be deposited with substrate temperatures of 200-300°C. Typically, the reaction consists of silane with an oxidant. At present we are using NH_3 gas to deposit nitride base coating and in the future we could go to TiO_2 base coatings, if necessary. The following reaction is used to produce Si_3N_4 films:

$$3SiH_4 + 4 NH_3 \rightarrow Si_3N_4 + 12 H_2$$
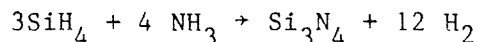
Because of the nonequilibrium nature of the deposition process, wide departures from stoichiometry are possible; the N/Si ratio can be varied from 0 to about 1.5, with corresponding changes in refractive index from about 3.5 to 1.8. Also, the films include bonded hydrogen in varying amounts. These films are useful for AR coating because the refractive index can be selected.

The optimum single-layer index has been calculated at 2. We have obtained this index value by adjusting the SiN_x stoichiometry to be slightly Si rich. We have actually deposited single-layer plasma AR coating on solar cells and are getting ready to deposit multilayer coatings. In these single-layer films, no visible absorption is observed but is expected if the N/Si ratio becomes smaller than that required for the high index coatings needed for multilayer AR coatings.[30] Mixtures such as SiO_2/TiO_2 will be needed for these.

Solar cell data with a single-layer plasma AR coating are shown in Table 16. This first experiment was performed on unpassivated cells, and the thickness of the AR coating (890 Å) turned out to be higher than the desired value of 750 Å. The measured refractive index was 1.95. The AR coating was deposited after cell fabrication (without AR coating) to determine the relative improvement without the interference of any process effects. Table 16 shows that despite the higher thickness the relative improvement was nearly 45% in J_{sc}. The n^+-p-p^+ cell efficiency with the spin-on TiO_2/SiO_2 AR coating is generally about 15%, but the best cell efficiency with this plasma coating was 15.9%. Efficiency improvement is even greater than 50% because we also see an appreciable enhancement in V_{oc}. With the conventional spin-on coating, V_{oc} is about 580 mV, but with plasma coating V_{oc} was ~590 mV, suggesting that this coating may be helping in passivation of the emitter surface. This could happen because atomic hydrogen in the discharge can tie up some dangling silicon bonds. In a second experiment with single layer coating, we deposited 750 Å thick coating which resulted in 45-47% improvement in J_{sc}. Thus, initial results on single-layer plasma Si_3N_x coating look quite promising, and experiments are in progress to apply this on oxide-passivated cells. This will be followed by the multilayer AR coating structure.

Table 16. Results of Single-Layer Plasma-Deposited Silicon Nitride Coating on Baseline n^+-p-p^+ Cells (AR Coating Thickness = 890 Å and Refractive Index = 1.95)

Cell ID	J_{sc} mA/cm^2	V_{oc} Volts	FF %	η %
(a)	Before AR Coating Deposition			
4	23.3	.566	.765	10.1
6	22.7	.557	.760	9.6
7	23.6	.567	.761	10.2
8	23.5	.567	.765	10.2
9	23.4	.566	.771	10.2
10	22.8	.553	.765	9.7
(b)	After AR Coating Deposition			
4	33.5	.588	.773	15.2
6	33.9	.592	.792	15.9
7	33.6	.588	.779	15.4
8	33.3	.589	.760	14.9
9	33.6	.590	.773	15.4
10	33.4	.586	.785	15.4

3.11 High-Low Emitter, MIS Contacts, and Reflective Back Contact

One attempt has been made to fabricate a high-low n^+-n emitter by epitaxially depositing a 2 μm thick n-layer with a doping of 10^{17} cm^{-3}. We were able to get the proper thickness and doping but our diffusion length appeared to be short; therefore, J_{sc} and the cell efficiencies were lower than the baseline cells. Another run with special precautions for high-lifetime epitaxial growth is in progress.

We have also made one run to study reflective back contact using Al, Au, and Ag metals in addition to standard Ti-Pd-Ag contact. These metals were deposited over the gridded back oxide. Au and Ag metals

showed poor adhesion to the back oxide and consequently peeled off. The Al metal looked somewhat promising with current densities in some cases about 0.5 mA/cm^2 better than Ti-Pd-Ag contact. This area needs to be investigated further.

We are in the process of making solar cells with front and back MIS contacts by growing thin (< 50 Å) oxides, oxynitrides, and low-pressure CVD nitride. The front metal grid and the back metal will be deposited directly on these thin dielectrics to completely avoid direct metal/silicon contact.

4. CONCLUSIONS

Consistent with our model calculations we have successfully fabricated greater than 17% efficient solar cells by passivating the cell surfaces. Compared to the unpassivated cells, oxide passivation gave ~ 3 mA/cm^2 improvement in J_{sc}, ~ 20 mV increase in V_{oc}, and greater than 2% increase in the absolute cell efficiency. Cell efficiencies of 17.2% on 4 Ω-cm float-zone silicon have been achieved by 110 Å thick front oxide and ~ 50 Å thick back oxide grown at 800°C. In these cells the majority of increase in V_{oc} comes from the front-surface passivation, although back-surface passivation also provides additional ~ 5 mV increase in V_{oc}. Even in 4 Ω-cm base cells, emitter surface recombination seems to limit J_o or V_{oc}, prior to any passivation.

In these 4 Ω-cm base cells, both front- and back-surface passivation contribute to the increase in J_{sc} by reducing the loss of photogenerated carriers to the surfaces. Spectral response measurements showed a very significant improvement in the quantum efficiency at shorter wavelengths, associated with appreciable increase in the quantum efficiency at longer wavelengths. This is consistent with the observed increase in J_{sc} and supports the fact that both front- and back-surface passivation are effective and working. No significant increase in the spectral response was observed in the wavelength range of 0.75 to 0.95 µm when the light is absorbed well within the bulk away from the surfaces. This indicates that oxide passivation does not appreciably change the intrinsic diffusion length of the bulk silicon in the finished cell. The effective diffusion length, at longer wavelengths, is much lower for the unpassivated cells but is hardly affected by the surface in the case of passivated cells.

Analysis of the I-V data shows that oxide passivation in 17.2% efficient cells lowers J_{ol} by about a factor of 2. This decrease coupled with ~ 3 mA/cm^2 increase in J_{sc} accounts for the observed 20 mV increase in the V_{oc} in our 4 Ω-cm float-zone silicon cells.

Solar cells fabricated on 0.75 Ω-cm silicon show an increase in J_{sc} of ~ 1.5 mA/cm^2, V_{oc} improvement of 17 mV, and absolute cell efficiency increase of about 1%. The best cell efficiency was 16.7%. The bulk diffusion length (~ 400 µm), calculated from the spectral response measurements, was less than the cell width; therefore, we saw some increase in the quantum efficiency at longer wavelengths but not as much as in the case of 17.2% efficient 4 Ω-cm cells. Due to the effectiveness of oxide passivation, J_o was reduced by a factor of two and quantum efficiency at shorter wavelengths was significantly improved.

Contrary to 4 Ω-cm and 0.75 Ω-cm cells, the oxide-passivated 0.1-0.2 Ω-cm cells did not show an improvement in the spectral response at longer wavelengths. This could be partly because the bulk diffusion length (300 µm, calculated from spectral response measurements) was less than the cell thickness (375 µm). The best cell efficiency on this material was 16.9%, in spite of the poor antireflective coating.

The bulk diffusion length in the 0.75 Ω-cm finished cell (~ 400 µm) and in the 0.1-0.2 Ω-cm cell (~ 300 µm) is actually greater than the bulk diffusion length in the 17.2% efficient 4 Ω-cm cell (263 µm). These low-resistivity crystals are indeed of very high quality. Their efficiency at present is slightly lower than the 17.2% cells made on 4 Ω-cm material, partly because they are ~ 375 µm thick and the back-surface passivation is therefore not as effective, and partly because we had poor antireflective coating on low-resistivity cells due to a problem in the photoresist step. More cells from low-resistivity material are being fabricated.

Solar cells (n^+-p-p^+) have also been fabricated on 0.3 to 0.7 Ω-cm gallium-doped Czochralski crystal which gave ~ 15% efficient

cells. After oxide passivation, the best cell efficiencies were
~ 16.5%.

A gallium back-surface field formed by open-tube gallium
diffusion at 1230^OC for 3 min resulted in a surface concentration of
~ 5 x 10^{18} cm^{-3} and a depth of ~ 2 μm. Despite the desired surface
concentration, we saw a 2% drop in cell efficiency due to a decrease in
carrier lifetime during the high-temperature diffusion.

Initial results on plasma-deposited antireflective coatings look
very promising. The single-layer coating alone gives $\geqslant$ 45% enhancement
in J_{sc} and >50% enhancement in efficiency. An appreciable increase in
V_{oc} suggests that the plasma Si_3N_x coating may be passivating the
silicon surface due to the presence of atomic hydrogen in the discharge.

An initial attempt has been made to fabricate high-low emitter,
MIS contacts and reflective back contact. Further experiments are in
progress to overcome some of the problems observed in the initial
experiments.

We have ordered 0.3 Ω-cm float-zone, high-lifetime silicon from
Wacker for future work. We believe this material can give much higher
efficiencies than the 17% already achieved on 4 Ω-cm substrates.

5. PROGRAM STATUS

5.1 Present Status

During this phase of the program we attempted all the tasks and successfully fabricated greater than 17% efficient cells. Specifically we:

- Fabricated 17.2% efficient cells on 4 Ω-cm float-zone silicon which were tested and verified at SERI.

- Analyzed the 17.2% efficient cells by spectral response measurements, I-V measurements, ellipsometric measurements, and spreading resistance measurements.

- Fabricated and analyzed 16.7% efficient oxide-passivated cells on 0.75 Ω-cm float-zone silicon.

- Fabricated and analyzed 16.9% efficient oxide-passivated cells on 0.1-0.2 Ω-cm float-zone silicon.

- Set up and calibrated the equipment for plasma-deposited antireflective coating, and fabricated and analyzed n^+-p-p^+ cells with single-layer Si_3N_x coatings.

- Initiated experiments for high-low emitter and reflective and MIS back contacts.

- Ordered 0.3 Ω-cm high lifetime float-zone wafers from Wacker for future work.

5.2 Future Activity

We expect to get low-resistivity, high-lifetime wafers from Wacker in January 1984. We plan to fabricate oxide-passivated, high-efficiency cells on this new material. We plan to design and make new masks for 2 cm x 2 cm cells with two or more different grid patterns. We will continue to investigate the MIS contacts and multilayer AR coating. We will also initiate experiments on dendritic web silicon, especially the use of H^+ implantation for improving web solar cell performance.

6. REFERENCES

1. F. A. Lindholm and J. G. Fossum, 14th IEEE Photovoltaic Specialists Conference Proceedings, p. 680 (1980).

2. A. Neugroschel, F. A. Lindholm, and S. C. Pao, Appl. Phys. Lett., 33:168 (1978).

3. R. B. Godfrey and M. A. Green, Appl. Phys. Lett., 34:790 (1979).

4. J. R. Davis and A. Rohatgi, 15th IEEE Photovoltaic-Specialists Conference Proceedings, p. 680 (1980).

5. A. W. Blakers and M. A. Green, Appl. Phys. Lett. 39:483 (981).

6. J. R. Davis et al., IEEE Trans. Electron Devices, ED-27, p. 67 (1980).

7. R. H. Hopkins et al., Final Report JPL/DOE-954331-81/14 (1982).

8. R. N. Ghoshtagore, Solid-State Electronics, 22(10):877 (1980).

9. M. Wolf, "Designing Practical Silicon Solar Cells Approaching the 'Limit Conversion Efficiency'," Proc. 14th IEEE Photovoltaic Specialists Conf., p. 563 (1980).

10. H. J. Hovel, Semiconductor and Semimetals, Vol. II, Solar Cells, Academic Press, p. 20 (1975).

11. M. P. Godlewski, C. R. Barona, and H. W. Brandhorst, Jr., "Low-High Junction Theory Applied to Solar Cells," Proc. 10th Photovoltaic Specialists Conf., p. 40 (1973).

12. J. G. Fossum, "Physical Operation of Back Surface Field Solar Cells," IEEE Trans. Electron. Devices, Vol. ED-24, p. 322 (1977).

13. A. Sinha and S. K. Chattopadhyaya, "Effect of Back Surface Field on Photocurrent in a Semiconductor Junction," J. Solid State Elect., Vol. 21, p. 943 (1978).

14. J. G. Fossum and E. L. Burgess, "High-Efficiency p^+-n-n^+ Back-Surface-Field Silicon Solar Cells," Appl. Phys. Lett., Vol. 33, p. 238 (1978).

15. J. B. Gunn, "On Carrier Accumulation and the Properties of Certain Semiconductor Junctions," J. Electron. Control, Vol. 4, p. 17 (1958).

16. M. P. D. Lanyon and R. A. Tuft, "Bandgap Narrowing in Heavily Doped Silicon," Proc. IEDM, Washington, D.C. p. 316 (1978).

17. F. A. Lindholm, private communication.

18. A. S. Grove, Physics and Technology of Semiconductor Devices, John Wiley, New York, 1967.

19. D. Kendall, presented at the Conf. Physics and Application of Lithium Diffused Silicon, NASA, Goddard Space Flight Center, Dec. 1969.

20. J. D. Beck and Conradt, Solid State Communications, Vol. 13, p. 93 (1973).

21. J. A. Amick and A. K. Ghosh, "Practical Limiting Efficiencies for Crystalline Silicon Solar Cells," J. Electrochem. Soc., Vol. 130 (1), p. 160 (1983).

22. J. G. Fossum, F. A. Lindholm, and M. S. Shibib, "The Importance of Surface Recombination and Energy-Bandgap Narrowing in p-n-Junction Silicon Solar Cells," IEEE Trans. Electron Devices, Vol. ED-26, p. 1294 (1979).

23. D. V. Lang, J. Appl. Phys., 45: 3023 (1974).

24. G. L. Miller, D. V. Lang, and L. C. Kimerling, Ann. Rev. Material Science, 377 (1977).

25. D. K. Schroder, and J. Guldberg, Solid State Electron., 14, 1285 (1971).

26. A. Rohatgi et al., "Effect of Titanium, Copper and Iron on Silicon Solar Cells," J. Solid State Electronics, 23, 415 (1980).

27. A. Rohatgi and P. Rai-Choudhury, Second Quarterly Report on "Research on the Basic Understanding of High Efficiency in Silicon Solar Cells," SERI Contract No. XB-3-02090-4, June 1983.

28. N. D. Arora, S. G. Chamberlain and D. J. Roulston, "Diffusion Length Determination in p-n Junction Diodes and Solar Cells," Appl. Phys. Lett. 37, 3, p. 325 (1980).

29. Mark Spitzer, Spire Corporation, private communication.

30. C. C. Johnson and T. Wydeven, "Plasma-Enhanced CVD Silicon Nitride Antireflection Coatings for Solar Cells," J. Solar Energy 31(4), 355 (1983).

7. ACKNOWLEDGMENTS

78

APPENDIX 1

IMPORTANCE AND CONSIDERATIONS OF HIGH-EFFICIENCY SOLAR CELLS

A. Rohatgi and E. F. Federmann
Westinghouse R&D Center
Pittsburgh, PA 15235

SUMMARY

This paper discusses the importance of high efficiency solar cells in reducing the cost of photovoltaic modules and systems. In order for photovoltaics to compete with other forms of energy on a large-scale basis, the cost of cell modules should come down to about 70¢/watt (1980 dollars) and, more importantly, module efficiencies should be about 16% because of high area-related costs. Based on recent trend in cell efficiency improvement, it is projected that 16% efficient modules could be realized within the next five years. The silicon material, processing, and design considerations for achieving 18-20% efficient cells are also discussed. It is shown that early price reduction in photovoltaic systems will occur because of the increase in cumulative production and steep learning curve, but when modules reach a price that assures substantial implementation then higher efficiency becomes the key element in reducing the cost and increasing the market.

IMPORTANCE AND CONSIDERATIONS OF HIGH-EFFICIENCY SOLAR CELLS

A. Rohatgi and E. F. Federmann
Westinghouse R&D Center
Pittsburgh, PA   15235

The importance of energy has increased tremendously in the past decade. Among the various alternatives available, solar energy is particularly attractive because it is essentially unlimited and has minimal pollution or physical danger associated with it. The photovoltaic cell is a very desirable solar energy conversion device because it converts sunlight directly into electricity rather than some intermediate form of energy. The solar cell was invented in the 1950s, but at that time its cost was too high and efficiency too low to compete with other forms of energy. Fortunately, with the advent of the space program in the 1960s and the thrust for terrestrial applications in the mid-1970s, the cost of solar cells has come down by about an order of magnitude to $\sim$\$10/watt, and in large quantities, prices as low as \$4.95/Watt have been quoted.

In order for photovoltaics to compete with other forms of energy on a large-scale basis, the cost of solar cell modules should come down to about 70¢/watt (1980 dollars) and, more importantly, module efficiencies should be about 16% because area-related costs become extremely important for large systems. It is now recognized increasingly in the photovoltaic community that high efficiency is a major attribute

that will determine the large-scale applicability of solar photovoltaic

systems. Present-day solar cell efficiencies fall considerably short of

the module efficiency requirements for very large-scale applications.

Assuming 5% reflection absorption losses, 1% mismatch losses, and 94% packing

factor for rectangular cells, 18% efficient cells will be required

for 16% efficient modules. Current module efficiencies are about 12%

in production.

In the last two to three years, solar cell efficiencies have

been in the range of 14-17% even at the research level, and there has

been some concern that single-crystal silicon cell efficiency has

reached its practical limit,[1] although the theoretical limit[2]

is ∿25% (AM1). However, recent breakthroughs have occurred in silicon

cell efficiency at the research level. Cell efficiencies in the range

of 17-18.5% have been reported (Table 1), which is existing proof that

photovoltaic know-how and technology today can provide 18% efficient cells,

although it could take another five years before such cells are

made reproducibly in mass production. The high efficiencies in Table 1 are the

result of high-quality silicon, innovative cell design, very careful cell

processing, reduced reflection losses, and improved understanding of

efficiency-limiting mechanisms such as bandgap narrowing, interband

Auger recombination, and surface recombination.

Based on recent progress toward high-efficiency cells (Table 1),

it is not unreasonable to expect 20% efficient cells at the research

level by 1986-1988 and at the production level by 1995. However, it

will take a considerable amount of basic research involving high-quality

silicon material, process development, cell design, and basic

understanding of efficiency-limiting factors. Some of the considerations

needed for 18-20% efficient cells are discussed below.

Material and Carrier Lifetime Considerations

There is a need to understand the crystal defects and

imperfections even in the very best silicon crystals grown today because

the measured lifetimes are well below the ultimate value. Based on the

best measured lifetime values of the order of 1 msec, Fossum et al.[7]

have hypothesized a vacancy-related fundamental defect in silicon

crystals which limits the lifetime in nondegenerate silicon. However,

in good-quality crystals, it is difficult to detect any deep level defect

even with the help of the most sensitive techniques, such as deep-level

transient spectroscopy that are available today. There is a need to

identify and minimize such crystal defects by improved methods of

crystal growth, which may include high-purity melt, improved crucible materials

and instrumentation, optimized growth conditions, and multiple

pass float zone refining.

There is some discrepancy in the lifetime data in the low-

resistivity range,[8] suggesting that interband Auger coefficients need

to be reevaluated. Any change in these coefficients would have

significant impact on the design of heavily doped regions. A low-

resistivity (0.1-0.3 Ω-cm) and high lifetime ($\sim$500 μsecs) ribbon silicon

would be a very desirable substrate for high-efficiency, low-cost solar cell

modules.

Process Considerations

Substantial research is also required in the area of device processing for high-efficiency cells. It is extremely important to select process conditions that will not introduce new defects or unwanted impurities; otherwise, the high lifetime of the starting material will become academic. High-temperature oxidations should be avoided to minimize stacking faults and dislocation-type defects. Special care must be taken during substrate cleaning, and favorable gettering ambients consisting of $POCl_3$ and HCl gas should be utilized whenever possible. Slow cooling and gradual wafer withdrawal from the furnace could also be important in preserving or even increasing the carrier lifetime of the starting material.

Design Considerations

If a high carrier lifetime cannot be obtained or retained in the cell, then clever cell design can still give high-efficiency cells. As suggested by the recent model calculations of Sah,[9] 20% efficient p^+-n-n^+ cells can be realized with a base lifetime of only 20 μsecs provided the cell thickness is reduced to 50 μm and the back-surface field penetration is 20 μm with an $N_D \sim 5 \times 10^{18}$ cm^{-3}. Use of a p^+ emitter reduces the interband Auger recombination in the emitter because of smaller Auger recombination rates. Similarly, our model calculations[10] suggest that for a n^+-p-p^+ cell with metal over p^+ region, the BSF region should be deep (> 10 μm), with a surface concentration of 3×10^{18} cm^{-3}. However, if the p^+ surface is passivated by growing a

thin layer of oxide, then the BSF region should be very thin in order to take advantage of the low surface recombination velocity.

In addition to the bulk material and BSF region, the emitter plays a very important role in determining cell efficiency. Most current cells employ a surface dopant concentration of $\sim 10^{20}$ cm^{-3}. In this range Auger recombination limits the minority-carrier lifetime values to nano-second range, while bandgap narrowing increases the saturation current and consequently reduces the open-circuit voltage. Another very important factor which lowers the current as well as the voltage is the emitter surface recombination velocity. We have found that just by passivating the emitter surface, the quantum efficiency of the cells at short wavelengths (0.4-0.5 µm) can be raised from 40% to greater than 75% (Figure 1). Therefore, the emitter region should not be regarded as a "dead layer" because by proper passivation coupled with reduced emitter doping, it may be possible to raise the quantum efficiency at shorter wavelengths to greater than 80-90%. However, special care must be taken in designing the contact for reduced emitter doping; otherwise, series resistance can degrade the fill factor. The back surface of the cells in Figure 1 was also passivated resulting in an increase in the quantum efficiency at longer wavelengths. Passivation of these cells also resulted in about 20 mV increase in V_{oc}.

Another factor that will help achieve 18-20% efficient cells is the design and fabrication of multilayer antireflective coatings with varying refractive index to minimize reflection losses. Most good

84

single-layer and double-layer AR coatings are able to increase J_{sc} by about 45%, but a multilayer coating could give an additional $\sim$5% improvement. For use in modules, the AR coating should be designed for the proper interface.

There is further potential for efficiency improvement by using tandem cells with silicon as the base.

Impact of Cell Efficiency on Photovoltaic System Costs and Markets

Just why do we need high efficiency cells? There are some who might say that the important factor is the cost per watt; and in instances where the system area related placement costs are small, this indeed seems to be true at this time. However, as photovoltaic module prices come down and market penetration becomes greater, efficiency of the cell becomes the vital factor in further module cost reduction.

Figure 2 shows our projection of module efficiency and price to the year 2000. The bands indicate a 90% probability the value will be within the range shown in the band. For the module price, the dashed curve shows the likely price.

Early price reduction will occur primarily because of increasing cumulative production and a rather steep learning curve. However, as the cell cost becomes a less dominant part of the module cost and conventional components that have been in high volume production for years become more important, the module learning curve becomes less steep and efficiency improvement is the key element in further cost reduction. Our evaluations indicate that this will occur at a module price of about $1.50/watt, and that below $1/watt, further price reduction will depend almost entirely on efficiency.

Perhaps a hypothetical example would be appropriate here. Assume a module priced at $1/watt using a 16% cell that results in a 12% efficiency module due to high mismatch losses and low packing factor. The module price per square meter is $120 in this case. If an 18% improved cell at the same module cost/meter^2 can be developed with a narrow statistical efficiency variation between cells and a form suited to a high packing factor, module efficiency would be 16%. This would result in a module price of $1/watt x .12 ÷ .16 or $0.75/watt. If the system placement cost for a particular application is $50/m^2, the cost of installing the array for the 16% cell will be .05 ÷ .12 = $0.42/watt, making the installed array cost $1.42/watt of array output under standard conditions and neglecting array wiring losses. For the 18% cell, the placement cost will be .05 ÷ .16 = $0.31/watt, and the total installed array cost, $1.06/watt. In this case, the reduction is $0.36/watt — $0.25/watt for the module and $0.11/watt for area related system costs.

How important are modest module price reduction to the photovoltaic potential? Figure 3 shows — with the usual 90% band — the dependence of annual Megawatt peak sales on module price. For the likely case, a reduction of module price from $1/watt to $.70/watt is projected to result in a more than threefold increase in market size from 2500 MWp to 8000 MWp.

These speculations on the impact of cell efficiency improvement have assumed that all other attributes of the cell and module remain the same. Attributes of importance are: for the cell — life, yield, narrow statistical variation in efficiency, adaptability to minimum steps and

automated techniques for cell and module manufacture, and adaptability to high packing factor; for the module – life maintenance and reliability, degradation, and automated processes of connection and assembly.

Trade-off of the above attributes with efficiency can have an important impact on system costs. In particular, life can have a profound effect. System life is usually taken to be 20 or 30 years. If the module life is less, not only does the system cost increase due to purcahse of new modules – the cost of physical replacement must also be added.

To summarize, when photovoltaic modules reach a price that assures substantial implementation, the major factor in reducing module cost will be increased efficiency. The increase in utilization of photovoltaic systems is dramatically affected in this implementation range by modest reductions in module price. As a bonus, reduction of placement costs for higher efficiency modules will further enhance system implementation. Thus, just at the time when photovoltaic systems become viable for many applications, further increase in efficiency is the key element in future market buildup.

TABLE 1

SOME RECENT HIGH EFFICIENCY SILICON SOLAR CELLS
TESTED UNDER ONE SUN AM1 ILLUMINATION

| J_{sc} mA/cm^2	V_{oc} mV	FF	η %	Substrate Resistivity Ω-cm	Source
36.0	625	.805	18.1	0.15	Applied Solar Energy
36.5	610	.775	17.2	10	Corporation[3]
36.2	600	.793	17.2	4	Westinghouse[4]
35.9	627	.800	18.0	0.3	Spire Corp.[5]
34.9	643	.813	18.1	0.2	University of New South Wales Australia[6]
33.0	653	.810	17.5	0.3 Concentrator Cell	Sandia National Laboratories[11]
34.0	624	.820	17.6	0.3 Concentrator Cell	Applied Solar Energy Corporation[11]
35.1	623	.780	17.1	0.3	Catholic University of Leuven, Belgium[12]
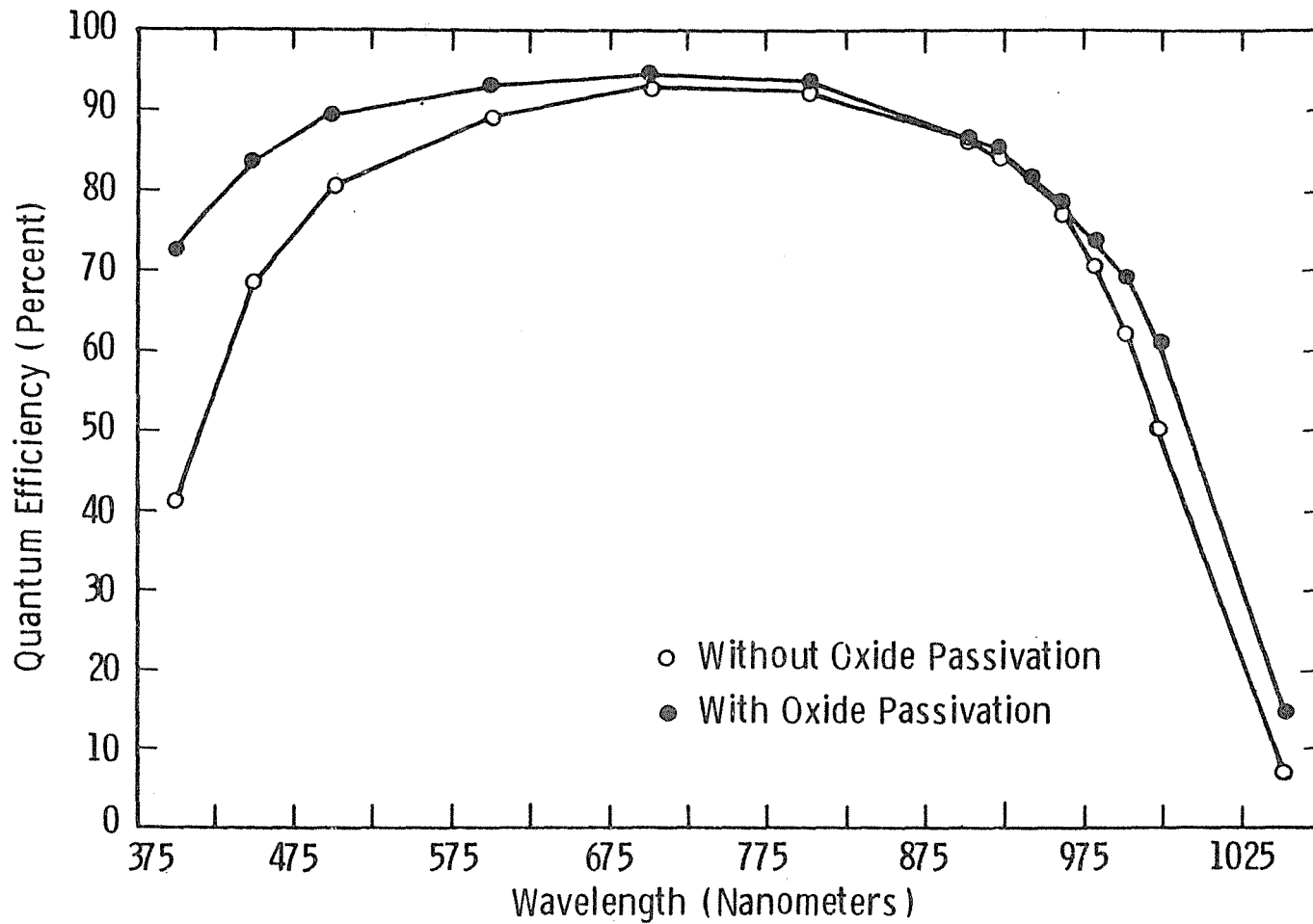
Fig. 1 – Quantum efficiency vs. wavelength plot for an unpassivated cell and 17. 2% efficient oxide passivated cell on 4 Ω-cm float zone silicon
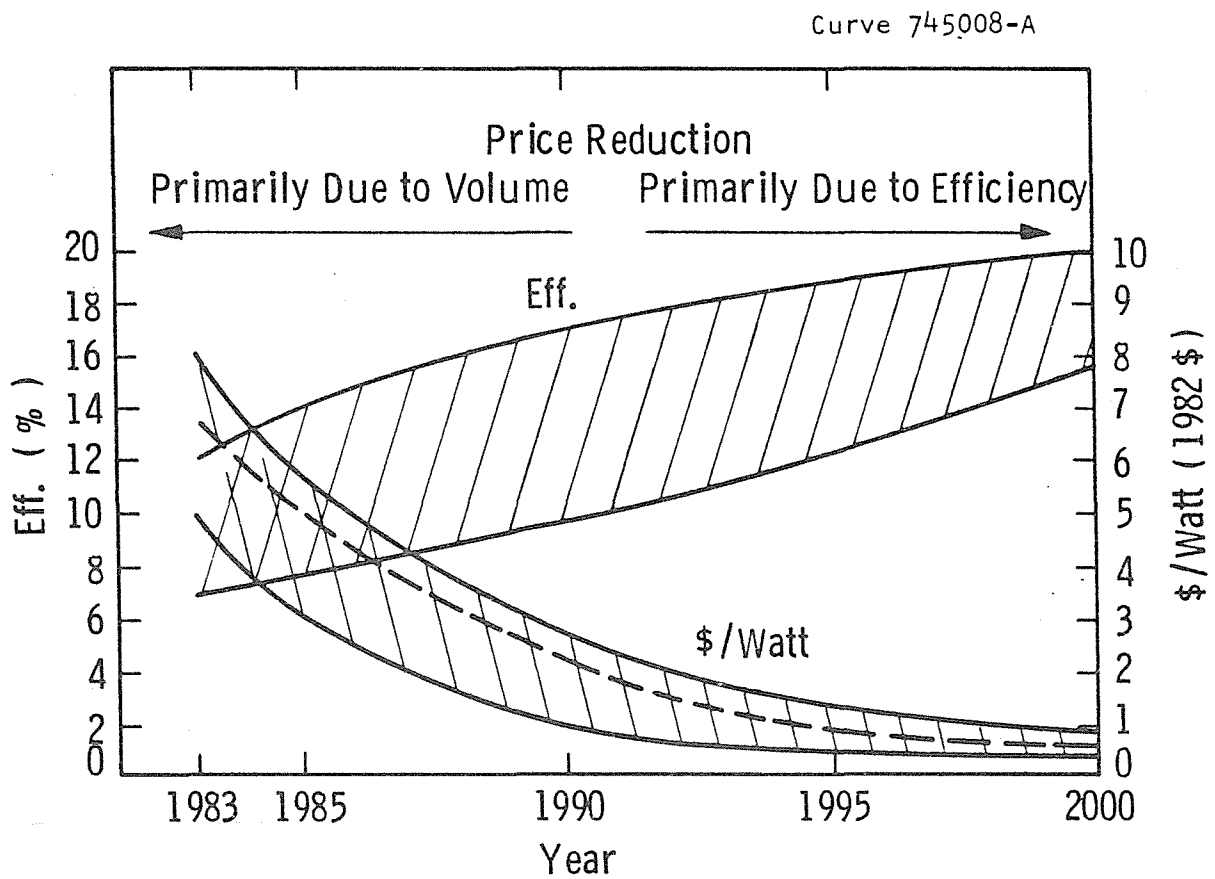
Fig. 2 —Projected module prices and efficiencies
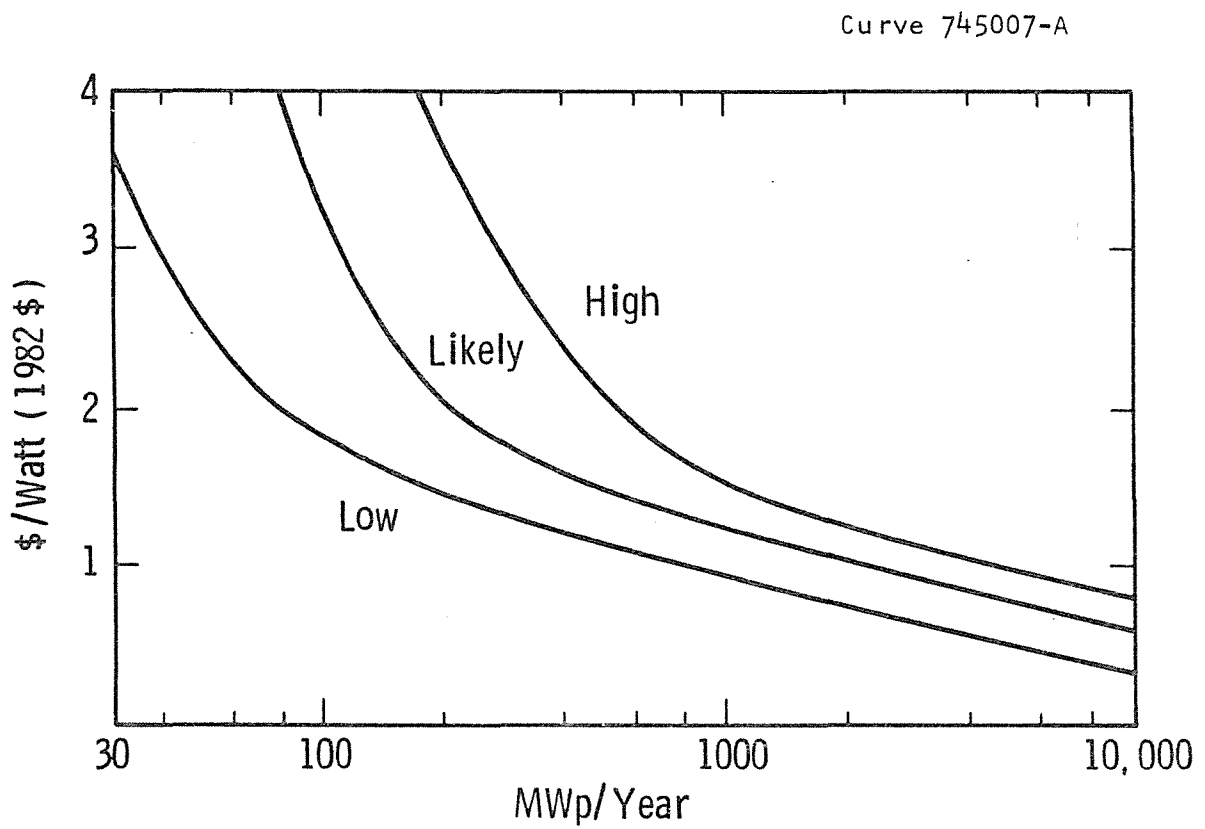
Fig. 3 —Module MWp/year as function of price

REFERENCES

1. J. A. Amick and A. K. Ghosh, J. Electrochem. Society $\underline{130}$ (1), 160 (1983).

2. M. Wolf, Proc. of 14th IEEE Photovoltaic Specialists Conf., p. 674 (1980).

3. P. A. Iles, Applied Solar Energy Corporation, private communication.

4. A. Rohatgi and P. Rai-Choudhury, 3rd Quarterly Report on "Research on Basic Understanding of High Efficiency in Silicon Solar Cells," SERI Contract No. XB-3-02090-4, July 1983, also submitted for 17th Photovoltaic Specialists Conf. (1984).

5. M. Spitzer, Spire Corporation, private communication; 3rd Quarterly Report on Research on Basic Understanding of High Efficiency in Silicon Solar Cells," SERI Contract No. ZB3-02090-3 also submitted for 17th Photovoltaic Specialists Conf. (1984).

6. A. W. Blakers, M. A. Green, and Shi Jigun, ISES Perth Meeting, Australia, 1983.

7. J. G. Fossum and D. S. Lee, Solid State Electronics $\underline{25}$ (8), 741 (1982).

8. M. Wolf, Analysis and Evaluation in the Production Process and Equipment Area of the Low Cost Solar Array Project, DOE/JPL Final Report of Contract No. 956034, April 1982.

9. C. T. Sah, "Study of Relationships of Material Properties and High Efficiency Solar Cell Performance on Material Composition, First Technical Report, DOE/JPL Contract No. 956289-83/1, July 1983.

10. J. R. Davis and A. Rohatgi, Proc. of 14th IEEE Photovoltaic Specialists Conf., p. 569 (1980).

11. H. T. Weaver and R. D. Nasby, Proc. of 16th IEEE Photovoltaic Specialists Conf., p. 361 (1982).

12. J. Nijs et al., Solar Cell, 7(3), p. 331 (1982).

APPENDIX 2

DESIGN, FABRICATION, AND ANALYSIS OF 17-18% EFFICIENT
SURFACE-PASSIVATED SILICON SOLAR CELLS

A. Rohatgi and P. Rai-Choudhury

ABSTRACT

A simple analytical model has been developed which provides useful guidelines for fabricating high-efficiency silicon solar cells. Consistent with the model calculations, both surfaces of n^+-p-p^+ solar cells were passivated by a thin layer of thermally grown SiO_2. Oxide passivation resulted in 17.2% efficient solar cells on 4 Ω-cm base material. Passivated cells show about 3 mA/cm^2 increase in J_{sc}, ~20 mV improvement in V_{oc}, and ~2% increase in absolute cell efficiency compared to the counterpart 15.2% efficient unpassivated cells. The majority of improvement in V_{oc} came from the emitter surface passivation, while both front- and back-surface passivation contributed to the increase in J_{sc}. The emitter region should not be regarded as a "dead layer" because emitter surface passivation can increase the quantum efficiency at short wavelengths from 40% to greater than 75%.

1. INTRODUCTION

The theoretical maximum efficiency of a silicon solar cell is about 25%, although present-day cells fall considerably short of this limiting value. This is largely a consequence of heavy doping effects, bandgap narrowing, and high recombination at and near the cell surfaces. Recent efforts to increase the efficiency of silicon solar cells have been focused appropriately on the problem of raising the open-circuit voltage since current collection efficiencies are approaching theoretical limits.[1-3] This emphasis has led directly to the problem of maximizing the effective diffusion length in all parts of the device, while using substrate material with the highest possible donor or acceptor concentrations. These provisions act in opposition and are modified by the specific details of the device structure. It is thus evident that an optimization is possible. The problem is complicated by imperfectly understood mechanisms or imprecise knowledge of the controlling parameters, and by experimental difficulties in separating the effects of these mechanisms. The major problems of efficiency improvement fall into the above categories; however, there are additional design requirements for efficient contacts and antireflective coatings. Although these areas are better understood, they are not trivial and must be satisfied in a manner compatible with the requirements of the rest of the device. In this paper we describe our effort of achieving high-efficiency silicon solar cells by a combination of modelling, innovative cell design, compatible cell processing, and a detailed analysis of high-efficiency cells.

2. MODEL CALCULATIONS

We have developed a simplified analytical model which provides useful insight and guidelines for fabricating high-efficiency solar cells. The model includes the effect of bandgap narrowing, Auger recombination, and recombination at the device surfaces, but it neglects

the electric field effects resulting from the gradient of doping concentrations.[4,5]

The model is based on the use of an internal recombination velocity as a measure of the minority-carrier losses in the various regions of the device. This directly provides the junction saturation current and thus the dark voltage-current characteristic which exerts primary control over cell performance. It is apparent that the major benefit of reducing recombination is the increase in open-circuit voltage, V_{oc}, which follows from reductions of the saturation current, J_o.

Solar cell efficiency is directly proportional to the open-circuit voltage and the short-circuit current. Both, of course, are subject to recombination losses, but here we will only concentrate on the variation of V_{oc}. Open-circuit voltage is inversely related to the saturation current (J_o).

$$V_{oc} = V_T \ln \left[1 + \frac{J_{sc}}{J_o} \right] \tag{1}$$

$$J_o = J_{ob} + J_{oe} = \frac{q n_i^2}{N_A} \cdot \frac{D_n}{L_n} \left\{ \frac{S_n \cosh \left(\frac{W_B}{L_n}\right) + \frac{D_n}{L_n} \sinh \left(\frac{W_B}{L_n}\right)}{\frac{D_n}{L_n} \cosh \left(\frac{W_B}{L_n}\right) + S_n \sinh \left(\frac{W_B}{L_n}\right)} \right\}$$

$$+ \frac{q n_i^2}{N_D} \cdot \frac{D_p}{L_p} \left[\frac{S_p \cosh \left(\frac{W_E}{L_p}\right) + \frac{D_p}{L_p} \sinh \left(\frac{W_E}{L_p}\right)}{\frac{D_p}{L_p} \cosh \left(\frac{W_E}{L_p}\right) + S_p \sinh \left(\frac{W_E}{L_p}\right)} \right] \tag{2}$$

(D_n, L_n) and (D_p, L_p) are the diffusivity and diffusion length of the minority carriers in the p-base and n^+ emitter region, W_B and W_E are the base and emitter widths beyond the junction edges, S_n and S_p are the surface recombination velocities at the front of the n^+ emitter region and back of the p-base region, respectively, and J_{ob} and J_{oe} are the base and emitter contribution to the reverse saturation current.[5]

The recombination at the back surface can be reduced by introducing a back-surface field or low-high junction,[6-9] while the recombination at the front surface can be reduced by growing an oxide layer. A detailed analysis of low-high structures by Gunn[10] provides a beginning place for our model. The starting expression for the present discussion is an equation, derived from the carrier transport equations which transform the surface recombination velocity of the device (S_o) to an effective recombination velocity seen by minority carriers at the low side of the low-high interface as a function of the properties of the low and high regions. This equation for a p-p^+ structure is:

$$S_e = \frac{n_p^+}{n_p} \frac{D_n^+}{L_n^+} \left[\frac{\dfrac{S_o L_n^+}{D_n^+} + \tanh\left(\dfrac{W_p^+}{L_n^+}\right)}{1 + \dfrac{S_o L_n^+}{D_n^+} \tanh\left(\dfrac{W_p^+}{L_n^+}\right)} \right]$$ (3)

where n_p^+, L_n^+, D_n^+ = concentration, diffusion length, and diffusivity of the minority carrier in the heavily doped p^+ region.

W_p^+ = width of the heavily doped region.

S_o = surface recombination velocity at the back of the high region.

S_e = effective recombination velocity at the low side of the low-high junction.

n_p = minority-carrier concentration in the low region.

We introduce the necessary modifications in the above expression to include the effects of degeneracy and bandgap narrowing. We have devised an empirical expression for the effective bandgap narrowing, (ΔV_G) based on the data of Lanyon[11] and Lindholm[12] corrected for degeneracy effects. The values thus adjusted for Fermi statistics can be used in the usual Boltzman expression for the np product, i.e.,

$$np = n_{ie}^2 = \exp \frac{(\Delta V_G^+ - \Delta V_G^-)}{V_T} \, n_i^2$$

where ΔV_G^+ and ΔV_G^- are the effective bandgap narrowing in the high and low regions, respectively.

$$\Delta V_G = 0.231 \left[\left(\frac{10^{20}}{N}\right)^{3/4} + 1 \right]^{-2/3} \tag{4}$$

and

$$n_i^2 = N_c \, N_v \, \exp\left(-\frac{E_G}{V_T}\right)$$

Equation 3 can now be written as:

$$S_e = \frac{N_A}{N_A^+} \frac{D_n^+}{L_n^+} \exp\left(\frac{\Delta V_G^+ - \Delta V_G^-}{V_T}\right) \left[\frac{\dfrac{S_o L_n^+}{D_n^+} + \tanh\left(\dfrac{W_p^+}{L_n^+}\right)}{1 + \dfrac{S_o L_n^+}{D_n^+} \tanh\left(\dfrac{W_p^+}{L_n^+}\right)} \right] \tag{5}$$

Empirical expressions were derived to relate the diffusion length and diffusivity to the impurity concentrations (N).

The expression for D was obtained from the data of Conwell as given in Grove.[13]

$$D = \frac{D_o}{1 + \left(\dfrac{N}{10^{17}}\right)^{0.6}} + A_o \tag{6}$$

where for p-type

$$D_o = D_{no} = 35$$

$$A_o = 1.8$$

and for n-type

$$D_o = D_{po} = 12.5$$

$$A_o = 1$$

The diffusion length is obtained using a Kendall's lifetime function[14] for bulk silicon (τ_K) combined with Beck and Conradt's[15] data for Auger recombination τ_A.

$$\tau_n = \left(\frac{1}{\tau_A} + \frac{1}{\tau_K}\right)^{-1} \tag{7}$$

where

$$\tau_K = \frac{\tau_o}{1 + \dfrac{N}{7 \times 10^{15}}} \tag{8}$$

Note the value chosen for τ_o is related to the quality of silicon. We have found that a value of 200 to 400 µs for τ_o is more appropriate for modeling high-performance devices.

The Auger lifetime is given by:

$$\tau_A = \frac{1}{(K_A \cdot 10^{-31})N^2} \tag{9}$$

where $K_A = 1.2$ for p-type
$K_A = 2.8$ for n-type

Then the diffusion length is obtained from:

$$L = \sqrt{D\tau} \tag{10}$$

It should be noted that the derivation of Equation 5 is completely general in that it may be applied to the calculation of an effective recombination velocity across an arbitrarily chosen region anywhere in the device as, for example, within the base region where the doping is constant. In this case we set $N_A = N_A^+ = N_A(\text{base})$. This velocity then characterizes the total recombination beyond this plane.

Assuming appropriate recombination velocity on the cell surface as the boundary conditions and from known doping profiles, we can now iteratively apply this calculation using Equation 5 from the back

surface, across the base to the edge of the depletion region, and thus account for all the recombination processes in the base and back by calculating S_{ejb}. A similar calculation for the n region above the junction can give S_{ejb}. Relating Equation 2 in terms of S_e as given in Equation 5 permits expressing the base and emitter component of the saturation current density as:

$$J_o = J_{ob} + J_{oe} = (qn_i^2 /N_A)S_{ejb} + (qn_i^2 /N_D)S_{eje} \qquad (11)$$

where S_{ejb}, N_A and S_{eje}, N_D are the recombination velocities and doping densities at the edges of the depletion region. Then, neglecting current contributions from the depletion region,

$$V_{oc} = V_T \, \ell n \, (\frac{J_{sc}}{J_{on} + J_{on}}) \qquad (12)$$

Figure 1 shows the results of model calculations for a back-surface field solar cell using three different back-surface field (BSF) structures with two different base diffusion lengths. In Figure 1 recombination velocity is plotted as a function of distance into the n^+-p-p^+ solar cell. Referring to the BSF region in the figure, the upper curve is for a high recombination ohmic back ($S_o = 10^6$ cm/sec), while the lower two curves are for the oxide-passivated backs with reduced S_o. The lowest curve was obtained by lowering the BSF surface-doping concentration to 10^{19} cm^{-3}, thus reducing the heavy doping effects. In the 4 Ω-cm base region, the solid curves are for a lower base diffusion length of 209 μm while the dotted curves are for longer base diffusion length of 467 μm. In this example we have assumed a diffused emitter with high-surface concentration with the emitter surface passivated ($S_o \sim 500$ cm/sec).

If the emitter surface is not passivated in this 4 Ω-cm cell, the $S_{eje} \gg S_{ejb}$, $J_{oe} \gg J_{ob}$, and V_{oc} is limited by J_{oe}. Model calculations in Figure 1 show that with the emitter surface passivated,

$S_{eje} \gtrsim S_{ejb}$, but due to much higher doping density in the emitter ($\sim 10^{17}$ cm^{-3}) at the edge of the depletion region[7] compared to the base doping (3.5×10^{15} cm^{-3}), $J_{ob} \gg J_{oe}$. Therefore, with emitter surface passivation, J_{ob} limits J_o. Now both S_{ejb} and the reverse saturation current can be reduced further by back-surface passivation or lower BSF doping (Figure 1) to gain additional increase in V_{oc}. Figure 1 shows that a long diffusion length (L > 3W) in the finished device is necessary to realize this benefit of back-surface passivation and lower BSF doping, otherwise S_{ejb} is limited by the diffusion velocity (D/L) of the carriers in the base. Calculations also indicate that for a diffusion length of 467 µm, with both surfaces passivated, a V_{oc} of 599 mV, J_{sc}[22] of 37 mA/cm^2, and a cell efficiency of 17.4% can be obtained. If the surface concentration of the BSF region is reduced to 10^{19} cm^{-3}, then a V_{oc} of 605 mV and a cell efficiency of 17.8% can be achieved on this 4 Ω-cm substrate.

Use of a lower resistivity substrate with similar diffusion length can further reduce the base component of the reverse saturation current and thus give greater improvements in V_{oc}. The design of the emitter could be more important for the low-resistivity substrate because J_{oe} may dominate J_o, even after front-surface passivation. Reduced doping in the emitter can lower J_{oe} further and provide additional gain in V_{oc}. A similar effect of doping concentration is shown in Figure 1 for the heavily doped p$^+$ region when J_{ob} dominates J_o.

3. EXPERIMENTAL WORK

Consistent with our model calculations, we passivated the solar cell surfaces to obtain higher open-circuit voltage. Solar cells with an n$^+$-p-p$^+$ structure were fabricated on 4 Ω-cm, p-type, boron-doped, 10 mils thick, <111> float-zone silicon. The n$^+$ emitter was formed by a 850°C POCl$_3$ diffusion which resulted in a junction depth of 0.3 µm and a sheet resistance of 60-80 Ω/square. The p$^+$ back-surface field (BSF) was fabricated by a 950°C boron diffusion. Thin thermal oxide was grown at

$800^{\circ}C$, which resulted in an oxide thickness of ~100 Å on top of the n^{+} region and ~50 Å on the p^{+} surface. All the high-temperature steps were followed by a slow cool at ~$1^{\circ}C$/min in order to preserve the high lifetime of the starting material. About 600 Å thick TiO_2/SiO_2 antireflective coating was applied by a spin-on process on top of the front oxide. Ti-Pd-Ag contacts were made on front and back. The cell area was 1 cm^2 and the front contact grid design had an area coverage of 2%. A similar grid pattern was opened through the back oxide to establish communication between the p^{+} region and the back metal contact.

Solar cells were tested under 100 mW/cm^2 AM1 spectrum with the help of a quartz-iodine simulator. Current-voltage measurements were also taken in the dark to separate cell resistances, bulk recombination, and junction recombination components numerically and/or graphically.[16,17] The bulk component of the transformed I-V data[16] had a slope equal to one and the reverse saturation current (J_o) was obtained from the intercept at $V = 0$.

Both reflectivity and spectral response measurements were performed over a wavelength range of 0.4 μm to 1.1 μm. In the spectral response measurements, photocurrent under short-circuit conditions from the cell is compared automatically to that from a standard silicon detector of calibrated spectral response. Absolute spectral response (amps/watt) was obtained by:

$$\frac{\text{Relative Spectral Response } (\lambda) \times \text{Standard Detector (A/W)}}{1-R\ (\lambda)}$$

From these data, internal quantum efficiency, $Q_E(\lambda)$, as a function of wavelength was determined according to:

$$Q_E(\lambda) = \frac{\text{Absolute Spectral Response } (\lambda) \times \text{Energy of Photons}}{q}$$

Internal quantum efficiency is defined as the number of electron-hole pairs collected relative to the number of photons entering the material.[5]

The effective diffusion length in the base was obtained from the plot of photon attenuation length ($1/\alpha$, where α is the photon absorption coefficient) and a variable X-1, where X is the ratio of photons absorbed per unit time in the base to the number of electrons per unit of time in the external circuit.[18] $X = e^{-\alpha(d+w)}/Q_E$, where d is the junction depth and w is the width of the depletion region at zero bias. The effective diffusion length would be equal to the time base diffusion length if the base width is much greater than the diffusion length; otherwise, it is a combination of bulk diffusion length and surface recombination velocity.

Ellipsometric measurements were performed to determine the thickness of the oxide layer and the antireflective coating separately and in combination.

4. RESULTS

All solar cells were fabricated on high-lifetime 4Ω-cm float-zone silicon. Consistent with the high lifetime of the starting material, deep-level transient spectroscopy (DLTS) performed on Schottky barrier diodes[19] showed no deep levels. Table 1 shows the cell data for the baseline n^+-p-p^+ solar cells, without any oxide passivation. Short-circuit current density (J_{sc}) in these cells is about 33 mA/cm^2, open-circuit voltage (V_{oc}) is ~580 mV, and the average cell efficiency is about 14.75% with the maximum exceeding 15%.

Table 2 shows the data for the solar cells with both surfaces passivated. In oxide-passivated cells, J_{sc} ~36 mA/cm^2, V_{oc} ~600 mV, and cell efficiencies are greater than 17%. A lighted I-V curve is shown in Figure 2. Table 3 shows a comparison of cell parameters of a 17.2% efficient oxide-passivated cell and a 15.2% efficient unpassivated cell. Oxide passivation results in an increase in J_{sc}, V_{oc}, and fill factor associated with a decrease in the reverse saturation current (J_o).

Table 1

Baseline Unpassivated Solar Cells (n^+-p-p^+) Fabricated
on 4 ohm-cm Float-Zone Silicon

Cell ID	Short-Circuit Current J_{sc} mA/cm^2	Open-Circuit Voltage V_{oc} Volts	Fill Factor	Cell Efficiency %
1	33.3	0.582	0.767	14.8
2	33.1	0.584	0.756	14.6
3	33.0	0.579	0.777	14.9
4	32.9	0.581	0.772	14.7
5	32.9	0.581	0.752	14.4
6	33.4	0.583	0.780	15.2

Table 2

Oxide-Passivated Solar Cells on Boron-Doped 4 Ω-cm
Float-Zone Silicon

Cell ID	Area (cm^2)	J_{sc} (mA/cm^2)	V_{oc} (mV)	FF (%)	η (%)
HIEFY 4-4	1.0	36.1	599	79.4	17.1
-5	1.0	36.2	600	79.3	17.2
-6	1.0	36.4	598	78.5	17.1
-7	1.0	36.2	599	79.1	17.2
-8	1.0	36.3	597	79.5	17.2
HIEFY 3-1	1.0	34.6	599	79.2	16.5
-2	1.0	34.6	598	78.9	16.4

Figure 3 compares the internal quantum efficiency of the oxide-passivated 17.2% efficient cell and the counterpart 15.2% efficient unpassivated cell. The data show a significant increase in the quantum efficiency at shorter wavelengths (0.4-0.55 µm) along with an appreciable increase in the quantum efficiency at longer wavelengths (0.9-1.1 µm) as a result of passivating both cell surfaces.

Table 3

A Comparison of Cell Parameters of a 15.2% Efficient Cell
and 17.2% Oxide-Passivated Cell

Parameter	Unpassivated n^+-p-p^+ Cell	Oxide-Passivated O-n^+-p-p^+-O Cell
J_{sc}	33.4 mA/cm^2	36.1 mA/cm^2
V_{oc}	583	600
FF	.78	.794
η	15.2%	17.2%
R_s	0.5 Ω	0.21 Ω
R_{sh}	104 kΩ	190 kΩ
J_{o1}	3.7 x 10^{-12} A/cm^2	2 x 10^{-12} A/cm^2

Figure 4 shows the 1/α versus X-1 plot for the oxide-passivated as well as the unpassivated cell. The two curves overlap in 1/α range of 15-60 μm and the slope of the two curves in this range gives a bulk diffusion length of 263 μm, but as we go to longer wavelengths the slope of the unpassivated cell curve becomes less steep, indicating a relative decrease in the effective diffusion length.

In order to gain more insight into the effect of surface passivation, the back metal and the back oxide were removed from a few 16.5% efficient oxide-passivated cells, protecting the front surface, and then the p^+ back surface was remetallized. These cells now only have front-surface passivation. Table 4 shows the cell data with a) both surfaces passivated, b) the same cells with only the front surfaces passivated, and c) unpassivated cells. The data (Table 4b-4c) show that front-surface passivation in these 4 Ω-cm cells provides a significant increase in V_{oc} (~13 mV) and an appreciable increase in J_{sc} (0.5-1 mA/cm^2). Back-surface passivation (Table 4a-4b) gives an additional increase in V_{oc} of ~5 mV and J_{sc} of 0.5 mA/cm^2.

Ellipsometric measurements on 17.2% efficient oxide-passivated cells showed that the antireflective coating consists of passivating oxide of thickness 112 Å with a refractive index of 1.458 and a spin-on

106

Table 4

Solar Cell Data With a) Both Surfaces Passivated,
b) Only Front-Surface Passivated, and
c) With No Surface Passivation

Cell ID	V_{oc} Volts	J_{sc} mA/cm^2	FF	η %
(a) Both Surfaces Passivated: $o-n^+-p-p^+-o$				
1	.599	34.6	.792	16.5
2	.598	34.6	.789	16.4
(b) Above Cells with Only Front-Surface Passivated: $o-n^+-p-p^+$				
1	.595	33.9	.795	16.0
2	.594	34.0	.793	16.0
(c) Cells Without Surface Passivation: n^+-p-p^+				
1	.582	33.5	.767	14.9
2	.582	33.3	.767	14.8

layer of 555 Å on top of the passivating oxide with a refractive index
of 2.03.

5. DISCUSSION

Table 2 shows that oxide passivation coupled with careful cell
processing can give solar cell efficiencies greater than 17% (AM1) on
good quality 4 Ω-cm float-zone silicon, with $V_{oc} > 600$ mV, J_{sc}
~36 mA/cm^2, and fill factor ~0.795. These parameters are in good
agreement with the model calculations in Section 2. These cells are
among the best cells reported to date, especially on 4 Ω-cm material.
The data in Table 3 show ~20 mV improvement in V_{oc}, ~3 mA/cm^2 increase
in J_{sc}, and about 2% (absolute) increase in cell efficiency in the
oxide-passivated cell compared to the counterpart unpassivated cell.

Dark I-V measurements (Table 3) indicate a decrease in reverse
saturation current, J_o, from 3.7×10^{-12} cm^{-2} to 2.0×10^{-12} cm^{-2}.

Using the expression $V_{oc} \simeq KT/q \; \ell n(J_{sc}/J_o)$, this decrease in J_o coupled with the measured increase in J_{sc} essentially accounts for the observed 18 mV increase in V_{oc} due to passivation in this pair of cells. Since $J_o = J_{oe}$ (emitter) $+ J_{ob}$ (base), to find out which component of J_o has been reduced, back-oxide passivation from some lower efficiency cells (16.5%) was removed and then they were retested (Table 4b) after remetallizing the p^+ back surface. The data in Table 4 indicate that, out of the ~18 mV increase in V_{oc} due to oxide passivation, a 13 mV improvement comes from the front-surface passivation and the remaining comes from the back-surface passivation. This also implies that without any surface passivation in these cells, $J_o \sim J_{oe}$ and, therefore, front-surface passivation alone is able to increase V_{oc}. If J_{ob} was limiting J_o, then the front-surface passivation would not have much influence on J_o or V_{oc}. It appears that after front-surface passivation in these 4 Ω-cm cells, J_o becomes base limited ($J_o \sim J_{ob}$) and, therefore, back-surface passivation gives an additional 5 mV improvement in V_{oc} (Tables 4a-4b). These observations are entirely consistent with our model predictions in Section 2, Figure 1.

Greater improvements in V_{oc} can be achieved from front-surface passivation in lower resistivity base material[20,21] with similar diffusion velocity (D/L). In these cells J_{ob} will no longer limit J_o; instead, the value of S achievable from front-surface passivation will define the lower limit of J_{oe} or J_o. However, if J_{oe} remains much greater than J_{ob}, even after front-surface passivation, then the back-surface passivation will not increase V_{oc} much further. Some attempts are being made to verify this by fabricating cells on 0.2-0.3 Ω-cm material specially grown for high lifetime.

Figure 3 explains the reason for the observed increase in J_{sc} due to oxide passivation. Shorter wavelengths (<0.55 μm) are primarily absorbed in the emitter, while longer wavelengths (>0.95 μm) are mostly absorbed near the back surface. The figure shows that front-surface passivation results in a significant improvement in the quantum efficiency at shorter wavelengths, while the back-surface passivation increases the

quantum efficiency at longer wavelengths. This is consistent with the data in Table 4, which show that both front- and back-surface passivation contribute to the observed increase in J_{sc}, since passivation reduces the number of photogenerated carriers that are lost to the surfaces. The quantum efficiency at ~0.4 µm wavelength could be raised from 40 to 75% by emitter surface passivation, which implies that in the unpassivated cell, a majority of the photogenerated carriers near the emitter surface are not collected because of high surface recombination, and not because of high bulk recombination in the emitter as a result of Auger and bandgap narrowing effects. Thus, the emitter region should not be regarded as a "dead layer" because simply by proper oxide passivation, emitter quantum efficiency can be made greater than 75%, and further improvements may be possible by reducing Auger recombination and bandgap narrowing effects in the emitter. Surface recombination can be minimized further by growing a thin tunnel oxide underneath the front and back metal to completely avoid direct metal/silicon contact.

Figure 3 indicates that quantum efficiency in the wavelength range of 0.85-0.95 µm is nearly the same for both unpassivated and passivated cells. Most of the light in this wavelength range is absorbed within the bulk silicon, away from the surfaces, since the absorption length is in the range of 20-60 µm. This suggests that oxide passivation has apparently not changed the actual diffusion length of the base material, which is calculated to be 263 µm in this wavelength range (Figure 4). At longer wavelengths (higher values of 1/α), the slope of the unpassivated cell becomes less steep relative to a passivated cell, indicating that its effective diffusion length decreases near the back surface due to high surface recombination velocity. The slope of the curve for the oxide-passivated cell in Figure 4 is only slightly affected at longer wavelengths, supporting the notion that a good back-surface passivation has been achieved.

6. CONCLUSIONS

Consistent with our model calculations, we fabricated greater than 17% efficient solar cells by passivating the cell surfaces. In the 4 Ω-cm base material used in this study, both front- and back-surface passivation by a thin layer of SiO_2 resulted in about 3 mA/cm^2 increase in J_{sc}, ~20 mV improvement in V_{oc}, and ~2% increase in the absolute cell efficiency. In these cells, the majority of increase in V_{oc} comes from front-surface passivation, although back-surface passivation also provides ~5 mV increase in V_{oc}. Both front- and back-surface passivation contribute to the increase in J_{sc} by reducing the loss of photogenerated carriers to the surfaces. Even in a 4 Ω-cm base cell, the emitter surface recombination velocity seems to limit J_o or V_{oc} when cell surfaces are not passivated.

Greater improvements in V_{oc} can be achieved by front-surface passivation in lower resistivity base cells provided the same diffusion velocity (D/L) and diffusion length to base width (L/W) ratio can be maintained. In such cells, J_{ob} will not limit J_o; instead, the lower limit of J_o will be defined by the value of S achievable from the front-surface passivation. The emitter region should not be treated as a "dead layer" because proper surface passivation can result in greater than 75% quantum efficiencies at short wavelengths (<0.55 μm), and further improvements are possible by reducing heavy doping effects or by growing tunnel oxide underneath the metal grid.

7. ACKNOWLEDGMENTS

8. REFERENCES

1. F. A. Lindholm and J. G. Fossum, "Review of Physics Underlying Recent Improvements in Silicon Solar Cell Performance," Proc. 14th IEEE Photovoltaic Specialists Conf., p. 680 (1980).

2. A. Neugroschel, F. A. Lindholm, S. C. Pao, and J. G. Fossum, "Emitter Current Suppression in a High-Low-Junction Emitter Solar Cell Using an Oxide-Charge-Induced Electron Accumulation Layer," Appl. Phys. Lett. 33, 168 (1978).

3. R. B. Godfrey and M. A. Green, "655 mV Open Circuit Voltage 17.6% Efficient Silicon MIS Solar Cells," Appl. Phys. Lett., 34, 790 (1979).

4. M. Wolf, "Designing Practical Silicon Solar Cells Approaching the 'Limit Conversion Efficiency'," Proc. 14th IEEE Photovoltaic Specialists Conf., p. 563 (1980).

5. H. J. Hovel, Semiconductor and Semimetals, Vol. II, Solar Cells, Academic Press, p. 20 (1975).

6. M. P. Godlewski, C. R. Barona, and H. W. Brandhorst, Jr., "Low-High Junction Theory Applied to Solar Cells," Proc. 10th Photovoltaic Specialists Conf., p. 40 (1973).

7. J. G. Fossum, "Physical Operation of Back Surface Field Solar Cells," IEEE Trans. Electron. Devices, Vol. ED-24, p. 322 (1977).

8. A. Sinha and S. K. Chattopadhyaya, "Effect of Back Surface Field on Photocurrent in a Semiconductor Junction," J. Solid State Elect., Vol. 21, p. 943 (1978).

9. J. G. Fossum and E. L. Burgess, "High-Efficiency p^+-n-n^+ Back-Surface-Field Silicon Solar Cells," Appl. Phys. Lett., Vol. 33, p. 238 (1978).

10. J. B. Gunn, "On Carrier Accumulation and the Properties of Certain Semiconductor Junctions," J. Electron. Control, Vol. 4, p. 17 (1958).

11. M. P. D. Lanyon and R. A. Tuft, "Bandgap Narrowing in Heavily Doped Silicon," Proc. IEDM, Washington, D.C. p. 316 (1978).

12. F. A. Lindholm, private communication.

13. A. S. Grove, Physics and Technology of Semiconductor Devices, John Wiley, New York, 1967.

14. D. Kendall, presented at the Conf. Physics and Application of Lithium Diffused Silicon, NASA, Goddard Space Flight Center, Dec. 1969.

15. J. D. Beck and Conradt, Solid State Communications, Vol. 13, p. 93 (1973).

16. A. Rohatgi, J. R. Davis, R. H. Hopkins, P. Rai-Choudhury, P. G. McMullin, and J. R. McCormick, "Effect of Titanium, Copper, and Iron on Silicon Solar Cells," J. Solid State Elect., Vol. 22, p. 415 (1980).

17. A. Neugroschel, F. Lindholm, and C. T. Sah, "A Method for Determining the Emitter and Base Lifetimes in p-n Junction Diodes," IEEE Trans. Electron. Devices, Vol. ED-24, p. 662 (1974).

18. N. D. Arora, S. G. Chamberlain, and D. J. Roulston, "Diffusion Length Determination in p-n Junction Diodes Solar Cells," Appl. Phys. Lett., Vol. 37, p. 325 (1980).

19. A. Rohatgi, "Application of DLTS Technique to Study Junctions and Interfaces," Vacuum-Surfaces-Thin Films, K. L. Chopra and T. C. Goel, Ed., Vanity Books, Delhi, p. 115 (1979).

20. J. G. Fossum, F. A. Lindholm, and M. S. Shibib, "The Importance of Surface Recombination and Energy-Bandgap Narrowing in p-n-Junction Silicon Solar Cells," IEEE Trans. Electron Devices, Vol. ED-26, p. 1294 (1979).

21. Mark Spitzer, Spire Corporation, private communication.

22. J. A. Amick and A. K. Ghosh, "Practical Limiting Efficiencies for Crystalline Silicon Solar Cells," J. Electrochem. Soc., Vol. 130 (1), p. 160 (1983).
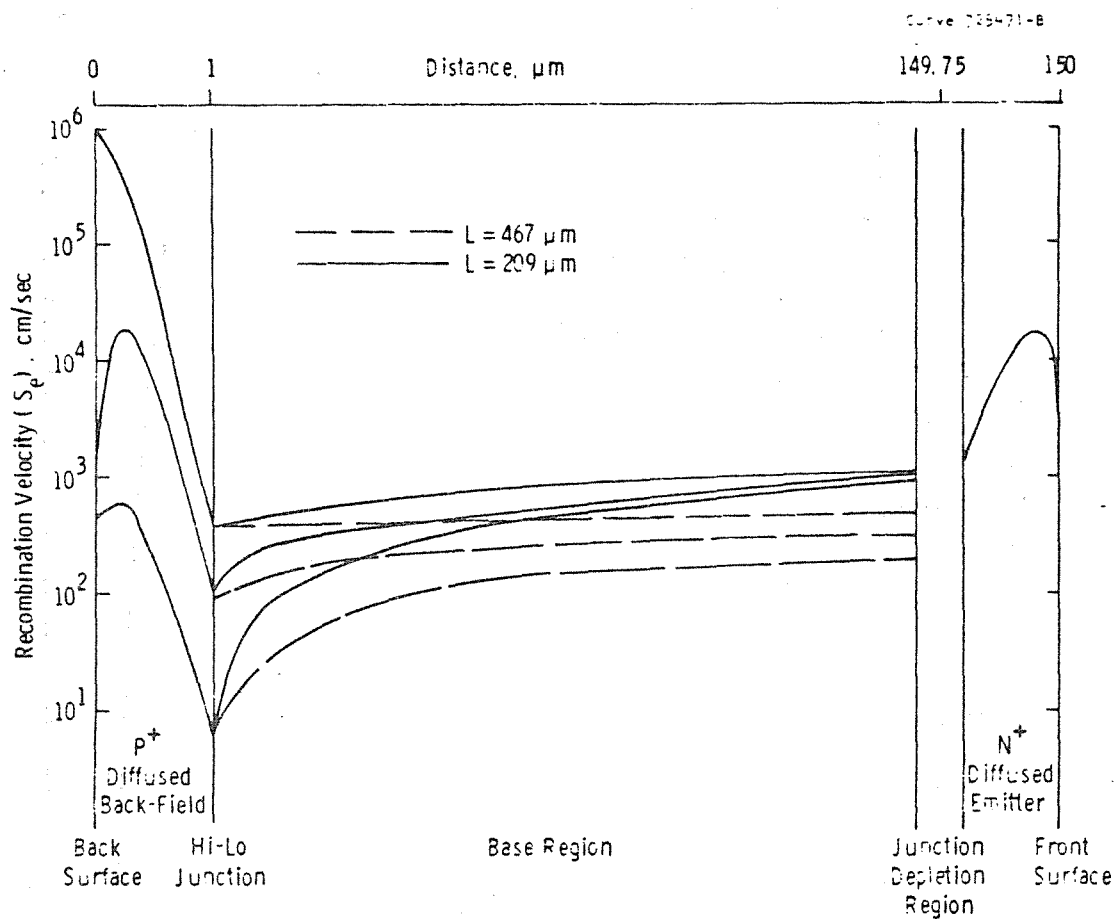
LIST OF FIGURES

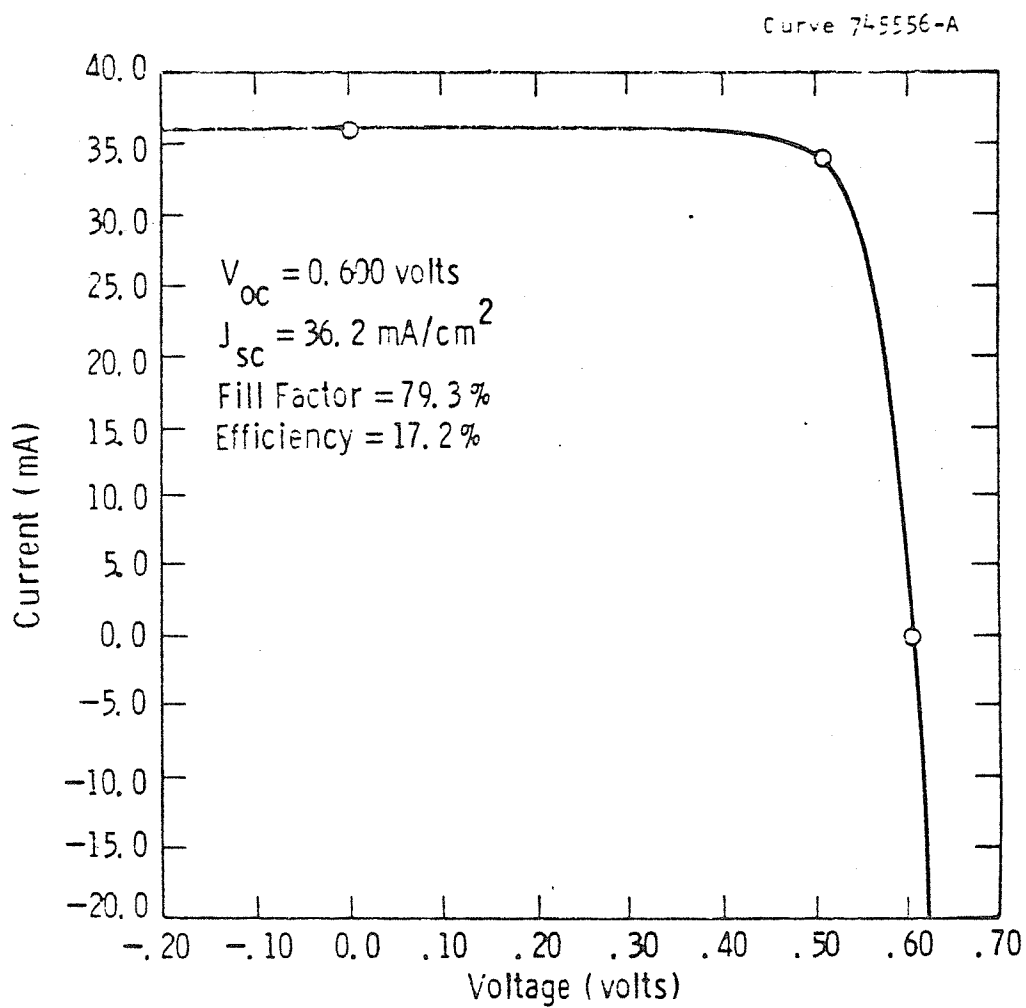Figure 1. Internal recombination velocity plots for back-surface
field solar cells.

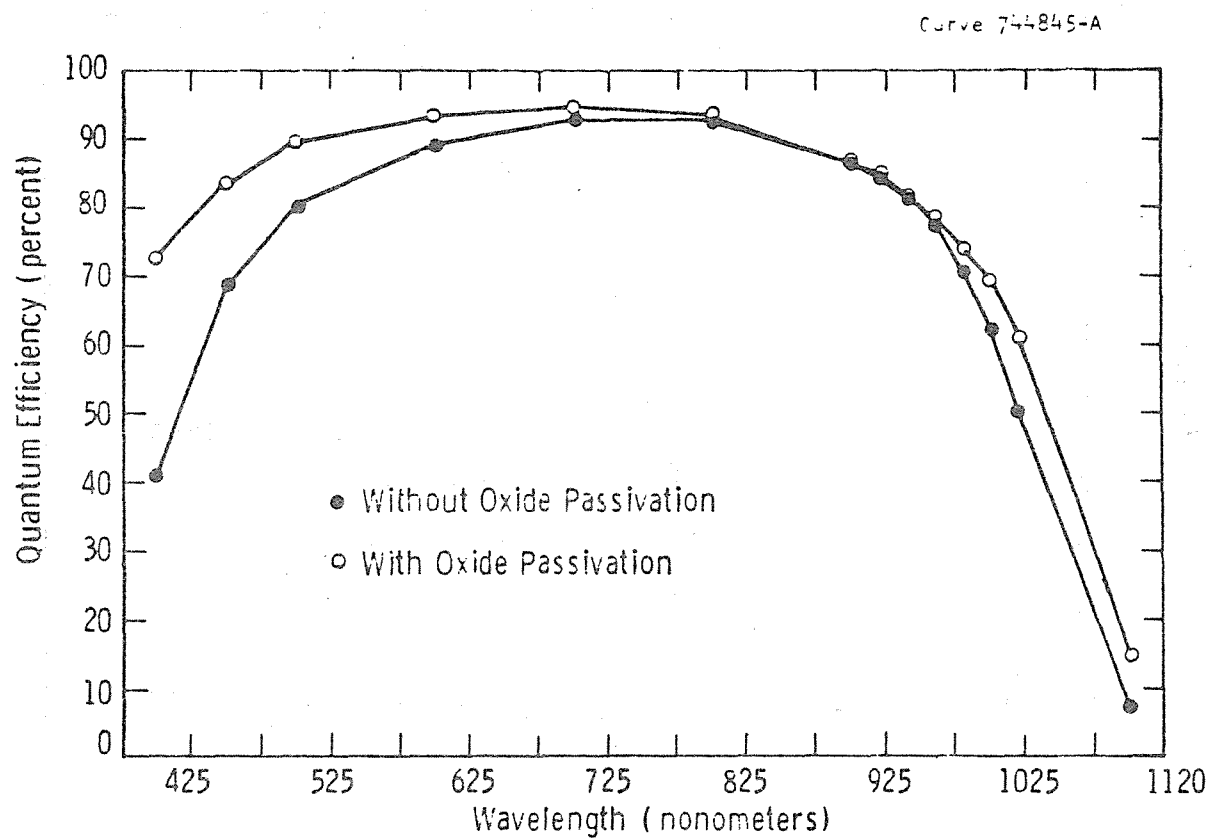Figure 2. Lighted I-V data for a 17.2% oxide-passivated cell fabricated on 4 Ω-cm float-zone silicon.

Figure 3. Internal quantum efficiency versus wavelength plot for an
unpassivated 15.2% efficient cell and 17.2% efficient oxide-
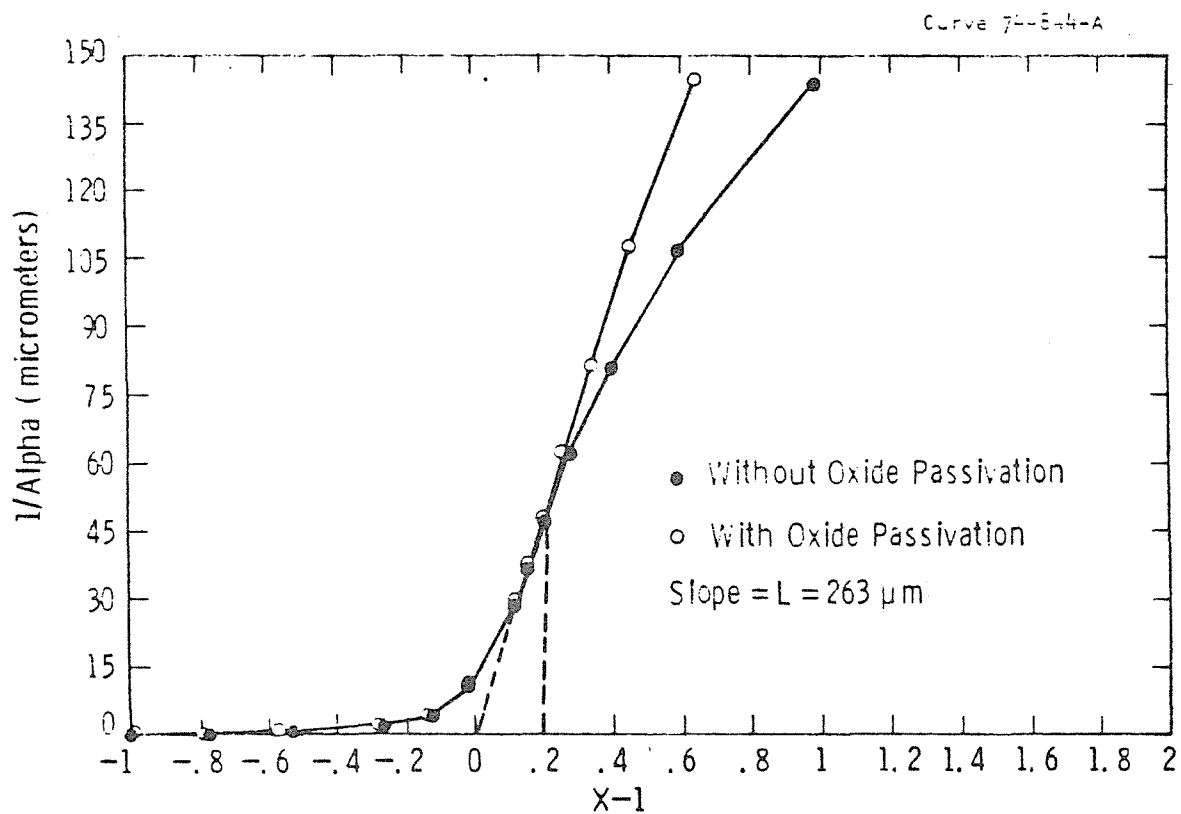passivated cell on 4 Ω-cm float-zone silicon.

117

Figure 4. Diffusion length plot for an unpassivated 15.2% efficient
cell and 17.2% efficient oxide-passivated cell on 4 Ω-cm
float-zone silicon.

Document Control Page	1. SERI Report No. SERI/STR-211-2451	2. NTIS Accession No.	3. Recipient's Accession No.

4. Title and Subtitle

Research on the Basic Understanding of High Efficiency in Silicon Solar Cells

5. Publication Date

September 1984

6.

7. Author(s)

A. Rohatgi and P. Rai-Choudhury

8. Performing Organization Rept. No.

9. Performing Organization Name and Address

Westinghouse R&D Center
1310 Beulah Road
Pittsburgh, Pennsylvania 15235

10. Project/Task/Work Unit No.

3434.10

11. Contract (C) or Grant (G) No.

(C) XB-3-02090-4

(G)

12. Sponsoring Organization Name and Address

Solar Energy Research Institute
1617 Cole Boulevard
Golden, Colorado 80401

13. Type of Report & Period Covered

Technical Report

14.

15. Supplementary Notes

Technical Monitor: Joseph Milstein

16. Abstract (Limit: 200 words)

This report presents results of research designed to develop a basic under-
standing of high-efficiency silicon solar cells and achieve cell efficiencies
greater than 17% by employing innovative concepts of material preparation, cell
design, and fabrication technology. The research program consisted of a theo-
retical effort to develop models for very high-efficiency cell designs, exper-
imental verification of the designs, and improved understanding of efficiency-
limiting mechanisms such as heavy doping effects and bulk and surface recombi-
nation. Research was performed on high-lifetime float-zone silicon, the baseline
material, low-resistivity gallium-doped czochralski silicon, and boron-doped
float-zone silicon.

17. Document Analysis

a. Descriptors Silicon; Solar Cells; Theoretical Data; Experimental Data

b. Identifiers/Open-Ended Terms High Efficiency Silicon Solar Cells

c. UC Categories

63

18. Availability Statement

National Technical Information Service
U.S. Department of Commerce
5285 Port Royal Road
Springfield, Virginia 22161

19. No. of Pages

129

20. Price

A07

Form No. 0069 (3-25-82)